

ปฏิกิริยาของเหล็กกล้าไร้สนิมเฟอร์ริติก (AISI441 และ CROFER22APU) ที่ใช้เป็นตัวเชื่อมต่อทาง
ไฟฟ้าในเซลล์เชื้อเพลิงแบบของแข็งออกไซด์ที่ใช้ก๊าซชีวภาพ



นายปิโยรส พรหมดิเรก

ศูนย์วิทยพัทยากร
จุฬาลงกรณ์มหาวิทยาลัย

วิทยานิพนธ์นี้เป็นส่วนหนึ่งของการศึกษาตามหลักสูตรปริญญาวิศวกรรมศาสตรดุษฎีบัณฑิต

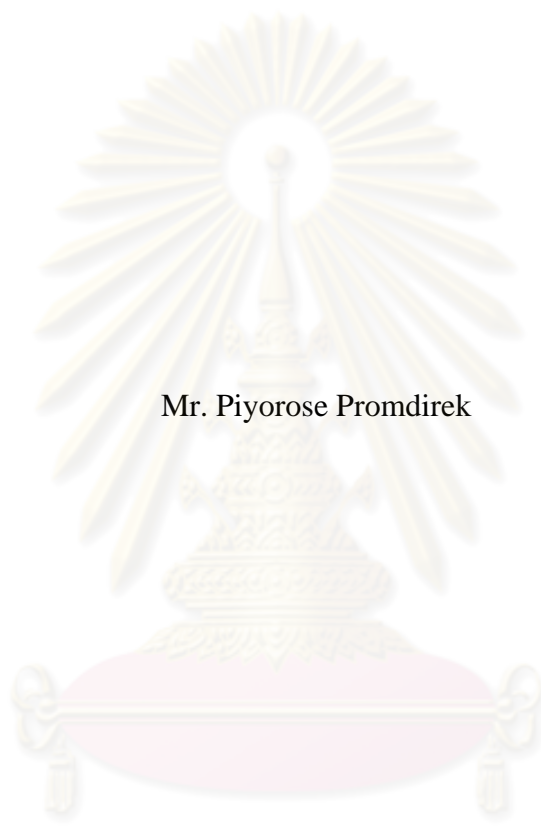
สาขาวิชาวิศวกรรมโลหการ ภาควิชาวิศวกรรมโลหการ

คณะวิศวกรรมศาสตร์ จุฬาลงกรณ์มหาวิทยาลัย

ปีการศึกษา 2553

ลิขสิทธิ์ของจุฬาลงกรณ์มหาวิทยาลัย

REACTIVITY OF FERRITIC STAINLESS STEELS (AISI441 AND
CROFER22APU) USED AS ELECTRICAL INTERCONNECTORS IN BIOGAS-
FUELLED SOLID OXIDE FUEL CELLS



Mr. Piyorose Promdirek

ศูนย์วิทยทรัพยากร
จุฬาลงกรณ์มหาวิทยาลัย

A Thesis Submitted in Partial Fulfillment of the Requirements
for the Degree of Doctor of Engineering Program in Metallurgical Engineering
Department of Metallurgical Engineering
Faculty of Engineering
Chulalongkorn University
Academic Year 2010
Copyright of Chulalongkorn University

Thesis Title REACTIVITY OF FERRITIC STAINLESS STEELS (AISI441 AND CROFER22APU) USED AS ELECTRIC INTERCONNECTORS IN BIOGAS-FUELLED SOLID OXIDE FUEL CELLS


By Mr. Piyorose Promdirek

Field of Study Metallurgical Engineering

Thesis Advisor Associate Professor Gobboon Lothongkum, Dr. Ing.

Thesis Co-advisor Professor Alain Galerie, Ph.D.

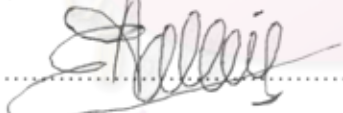
Accepted by the Faculty of Engineering, Chulalongkorn University in Partial Fulfillment of the Requirements for the Doctoral Degree


..... Dean of the Faculty of Engineering
(Associate Professor Boonsom Lerdhirunwong, Dr. Ing)

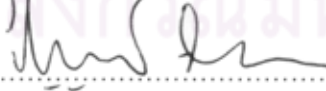
THESIS COMMITTEE



..... Chairman
(Assistant Professor Sawai Danchaiwijit, Ph.D.)


..... Thesis Advisor
(Associate Professor Gobboon Lothongkum, Dr. Ing)


..... Thesis Co-advisor
(Professor Alain Galerie, Ph.D.)


..... Examiner
(Assistant Professor Patama Visuttiwitkul, Ph.D.)


..... Examiner
(Panyawat Wangyao, Ph.D.)


..... External Examiner
(Assistant Professor Somrerak Chandra-ambhorn, Ph.D.)

ปิโยรส พรหมดิเรก : ปฏิกริยาของเหล็กกล้าไร้สนิมเฟอริติก (AISI441 และ CROFER22APU) ที่ใช้เป็นตัวเชื่อมต่อทางไฟฟ้าในเซลล์เชื้อเพลิงแบบของแข็งออกไซด์ที่ใช้ก๊าซชีวภาพ (REACTIVITY OF FERRITIC STAINLESS STEELS (AISI441 AND CROFER22APU) USED AS ELECTRIC INTERCONNECTORS IN BIOGAS-FUELLED SOLID OXIDE FUEL CELLS)
 อ. ที่ปรึกษาวิทยานิพนธ์หลัก : รศ. ดร. กอบบุญ หล่อทองคำ, 162 หน้า

วัตถุประสงค์ของการวิจัยนี้เพื่อศึกษาและเข้าใจพฤติกรรมการกัดกร่อนของเหล็กกล้าไร้สนิมเฟอริติกชนิด AISI 441 (18CrTiNb) และ CROFER22APU ที่อุณหภูมิสูงเพื่อเป็นตัวเลือกสำหรับตัวเชื่อมต่อทางไฟฟ้าของเซลล์เชื้อเพลิงแบบของแข็งออกไซด์ (SOFCs) ภายใต้ก๊าซชีวภาพสังเคราะห์ ($\text{CH}_4 + \text{CO}_2$) ที่แห้งและใช้ทางด้านขั้วบวกของเซลล์เชื้อเพลิง การวิเคราะห์เทอร์โมไดนามิกส์พบว่าในก๊าซดังกล่าวมีความดันย่อยของออกซิเจนอยู่ในช่วงของ 10^{-23} ถึง 10^{-20} บาร์ ที่อุณหภูมิระหว่าง 700 ถึง 900°C และคาร์บอนที่เป็นของแข็งเกิดขึ้นในสภาวะดังกล่าว จากการทดลองจลนพลศาสตร์พบว่าการเปลี่ยนแปลงมวลเป็นแบบเชิงเส้นที่อุณหภูมิระหว่าง 700 ถึง 900°C แบบจำลองของการเกิดออกไซด์ในการศึกษาค้นคว้านี้ได้ถูกเสนอ และวิพากษ์ เมื่อเปรียบเทียบกับค่าคงที่ทางจลนพลศาสตร์ของ AISI 441 ที่อยู่ในคาร์บอนไดออกไซด์บริสุทธิ์พบว่า จลนพลศาสตร์ของการกัดกร่อนในก๊าซชีวภาพเร็วกว่าและเพิ่มขึ้นตามการเพิ่มปริมาณการผลิตก๊าซมีเทนในก๊าซชีวภาพแห้ง ผลการทดสอบด้วยเครื่อง X-ray diffraction ยืนยันการเกิดของโครงสร้างสปีเนล Mn - Cr และ Cr_2O_3 ที่มีส่วนผสมของคาร์ไบด์อยู่ ลักษณะพื้นผิวของชิ้นงานที่ถูกกัดกร่อนมีขนาดออกไซด์หนาแน่นที่อุณหภูมิต่ำกว่า 800°C ซึ่งมีลักษณะเป็นเกราะป้องกันที่มีประสิทธิภาพการแพร่ของคาร์บอน อย่างไรก็ตามเมื่ออุณหภูมิถึง 900°C ออกไซด์สเกลมีรอยแตกและรูพรุนเกิดขึ้น ทำให้คาร์บอนสามารถตกตะกอนและกระจายตัวง่ายกว่าที่ 900°C และอาจนำไปสู่การสร้างคาร์ไบด์ภายใน ทำให้อุณหภูมิในการทำงานสูงสุดของตัวเชื่อมต่อทางไฟฟ้านี้ที่ทำด้วยเหล็กกล้าไร้สนิมเฟอริติก AISI 441 ภายใต้ก๊าซชีวภาพอยู่ที่ 800°C

ภาควิชา..วิศวกรรมโลหการ....

สาขาวิชา..วิศวกรรมโลหการ..

ปีการศึกษา 2553

ลายมือชื่อนิสิต.....

ลายมือชื่อ อ.ที่ปรึกษาวิทยานิพนธ์หลัก.....



กอบบุญ หล่อทองคำ

5071871321 : MAJOR METALLURGICAL ENGINEERING

KEYWORDS : Solid oxide fuel cells/ SOFCs/ interconnects/ ferritic stainless steels/ biogas/ carbon dioxide/ corrosion kinetics/ carburization/ surface morphology


PIYOROSE PROMDIREK : REACTIVITY OF FERRITIC STAINLESS STEELS (AISI441 AND CROFER22APU) USED AS ELECTRIC INTERCONNECTORS IN BIOGAS-FUELLED SOLID OXIDE FUEL CELLS. THESIS ADVISOR : ASSOC. PROF. GOBBOON LOTHONGKUM, Dr.-Ing., 162 pp.

The objective of this study is to understand the high temperature corrosion behaviour of the ferritic stainless steel type AISI 441 (18CrTiNb) and CROFER22APU, a candidate for SOFC interconnectors, under dry synthetic fermentation biogas ($\text{CH}_4 + \text{CO}_2$ mixtures) possibly used at the anode side of the cell. Thermodynamic analysis showed that, in such mixtures, the partial pressure of oxygen lies in the range of 10^{-23} to 10^{-20} bar for temperature between 700 and 900°C and that the formation of solid carbon may take place in several conditions. Kinetic experiments showed linear mass change at temperatures between 700 and 900°C. The modeled kinetics was discussed in this study. In this temperature range, kinetic experiments showed linear mass change. Comparing with the linear rate constants of 441 oxidised in pure CO_2 , corrosion in biogas is larger and increases with increasing the methane content in the dry biogas. XRD results confirmed the formation of Cr_2O_3 and Mn-Cr spinel, with a mixture of internal carbides. The surface morphology of the corroded specimens showed a dense oxide scale at temperatures less than 800°C, serving as an efficient barrier to carbon penetration. However, when the temperature reaches 900°C, cracks and pores appear in the oxide scale, carbon can precipitate and diffuse easier than at 800°C and may lead to internal carbide formation. In such biogas atmospheres, 800°C seems the maximum operating temperature of devices containing this ferritic stainless steel.

Department : Metallurgical Engineering

Field of Study : Metallurgical Engineering

Academic Year : 2010

Student's Signature 

Advisor's Signature 

ACKNOWLEDGEMENTS

This work was conducted in the frame of the 2007-2008 “Hubert Curien” Franco-Thai program on “Biogas-fuelled SOFC interconnect: Reactivity and Surface modification” coordinated by the Thai-French Innovation Centre (TFIC) of King Mongkut’s University of Technology North Bangkok. The author would like to gratefully thank Professor Alain Galerie of the Institut National Polytechnique de Grenoble (INPG) as the head of this project in the French side and Assistant Professor Somrerk Chandra-ambhorn as the head in Thai side. The appreciatory thanks are also Associate Professor Gobboon Lothongkum of Chulalongkorn University (CU) as the project partner. The author’s study has also been under international PhD thesis co-supervision between Grenoble INP and Chulalongkorn University. The author also thanks the French Region Rhone-Alpes who provided additional financial support. Their support made the author’s PhD study at INPG and CU possible.

The author would like to thank Professor Michel Ponds, Professor Alain Galerie and Professor Yves Wouters for welcoming him to pursue the PhD study at the Laboratory of Science et Ingénierie des Matériaux et Procédés (SIMaP), France. The author had spent the memorable times under the supervision of Professor Alain Galerie as the thesis director at INPG, France and Associate Professor Gobboon Lothongkum as the thesis director at CU, Thai, and with the kindly help of Professor Yves Wouters. He wishes to express his deep gratitude to them.

The acknowledgement is also given to UGINE&ALZ Research Centre, Arcelor Group and ThyssenKrupp VDM for the samples of AISI441 and Crofer22APU Sheets respectively. The author gratefully thanks Assistant Professor Sawai Danchaiwijit of the CU as the President of Jury and also Dr. Panyawat Wangyao, and Assistant Professor Patama Visuttipitukul of CU, as well as Associate Professor Chatchai Somsiri of the Thainox company and Professor Sébastien Chevalier of the University of Burgundy for their valuable comments as the reviewers of the thesis manuscript.

Contents

Abstract (Thai)	IV
Abstract (English)	V
Acknowledgements	VI
Chapter I: Introduction	1
1.1 Industrial Context.....	1
1.1.1 Solid oxide fuel cells (SOFCs).....	1
1.1.2 Biogas-fuelled SOFCs.....	3
1.1.3 Metallic interconnects.....	5
1.2 Objective of Research.....	7
1.3 Research Scope.....	8
1.4 Advantage of Research.....	8
1.5 Research Planning.....	9
Chapter II: Literature review	10
2.1 Thermodynamics Considerations.....	10
2.1.1 Thermodynamics of gaseous atmospheres.....	14
2.1.2 Thermodynamics of metal oxide formation.....	16
a) Ellingham-Richardson diagram.....	18
b) Phase diagrams of some Fe-based alloys.....	20
c) Stability diagram in carburization.....	23
2.2 High Temperature Corrosion.....	25
2.2.1 Oxidation mechanisms.....	25
2.2.1.1 Defect and diffusion in corundum structure.....	25
2.2.1.1.1 Corundum structure.....	26
2.2.1.1.2 Defects structure of pure Cr ₂ O ₃	27
2.2.1.2 Kinetic approach of scale formation (Sarrazin, 2000).....	29
2.2.2 High temperature corrosion in carbon-containing gases.....	33
2.2.2.1 Physico-chemical characterization in CO ₂ or CO atmospheres.....	33
a) Oxidation kinetics.....	33
b) Scale characterization.....	36
2.2.2.1 Physico-chemical characterization in carburization atmospheres.....	37

Chapter III: Experimental methods	40
3.1 Materials	40
3.1.1 Stainless steels	40
3.1.2 Experimental gas supply.....	41
3.2 Thermodynamic Calculations	41
3.3 Kinetic Experiments.....	42
3.3.1 Oxidation kinetics of ferritic stainless steels in CO ₂ atmosphere.....	43
3.3.1.1 Materials preparation.....	43
3.3.1.2 Thermogravimetric monitoring	43
a) Isothermal kinetics of oxidation	47
b) Isobaric kinetics.....	47
3.3.2 Kinetics of corrosion of ferritic stainless steels exposed to synthetic biogas 48	
3.3.2.1 Materials preparation.....	48
3.3.2.2 Isothermal corrosion in horizontal furnace.....	48
3.3.2.3 Thermogravimetric experiments.....	50
3.4 Corrosion Scale Characterizations	52
3.4.1 Scanning electron microscope and energy dispersion spectrometry	52
3.4.2 X-Ray Diffraction.....	53
3.4.3 Photoelectrochemistry	54
3.4.4 Marker experiments.....	55
3.4.5 Microhardness	56
Chapter IV: Oxidation kinetics of ferritic stainless steels in CO₂ atmosphere at high temperatures	57
4.1 Introduction.....	57
4.2 Thermodynamic Calculation.....	57
4.2.1 Partial pressure of oxygen	57
4.2.2 Oxide stability diagram.....	59
4.3 Oxidation Kinetics	60
4.3.1 Isothermal oxidation kinetics.....	60
a) Oxidation kinetics of 441	60
b) Oxidation kinetics of Crofer	61
c) Arrhenius plot of temperature dependence	62
4.3.2 Isobaric oxidation kinetics of 441	64

4.4 Scale Characterization	67
4.4.1 AISI 441	67
4.4.1.1 X-ray diffraction analysis.....	67
4.4.1.2 Photoelectrochemistry experiments	68
4.4.1.3 Scale morphology.....	70
4.4.1.4 Markers experiment.....	74
4.4.2 Crofer22APU	74
4.4.2.1 X-ray diffraction analysis.....	74
4.4.2.2 Scale morphology.....	75
4.5 Mechanism of Oxidation Modeling.....	78

Chapter V: Corrosion behaviour of ferritic stainless steels exposed to synthetic biogas at high temperature.....82

5.1 Introduction.....	82
5.2 Thermodynamic Calculations	82
5.2.1 Thermodynamics of biogas	82
a) 30% CH ₄ + 70% CO ₂	83
b) 50% CH ₄ + 50% CO ₂	84
c) 70% CH ₄ + 30%CO ₂	85
5.2.2 Oxide stability diagram of AISI441	93
5.2.3 Carbide stability of AISI441 in biogas	95
5.3 Kinetics Behaviour of Ferritic Stainless Steels.....	97
5.3.1 Isothermal kinetics of corrosion	97
5.3.2 Temperature dependence of corrosion kinetics	101
5.4 Scale Characterization	108
5.4.1 XRD analysis.....	108
5.4.2 Scale morphology	111
5.4.3 Thickness	122
5.4.4 Microhardness	123

Chapter VI: General conclusion and perspectives.....126

6.1 General Conclusion.....	126
6.1.1 Conclusions for steels under CO ₂ atmosphere	126
6.1.2 Conclusions for steels under synthetic biogas.....	127

6.2 Perspectives	129
References	131
Appendices	137
Appendix A: Thermodynamic calculation	137
Appendix B: Oxide thickness calculation	147
Appendix C: Naphthalene formation	149
Biography	152



ศูนย์วิทยทรัพยากร
จุฬาลงกรณ์มหาวิทยาลัย

Chapter I

Introduction

1.1 Industrial Context

1.1.1 Solid oxide fuel cells (SOFCs)

Among various types of effective technologies for energy conversion, solid oxide fuel cells (SOFCs) system is one of future energy supplies with regard to high potential, and environmental friendly technologies. SOFCs can make use of various fuels (Hydrogen –as do other fuel cell types-, as well as methane (natural gas, biogas, etc.) and reformed liquid fuels (diesel, kerosene, etc.)). The multi-fuel capability with little or no fuel gas treatment is a unique characteristic of SOFC. Moreover, the produced heat can be easily used in cogeneration systems with or without turbines. The combination of SOFC with a gas turbine offers high electrical efficiencies compared to other power conversion systems (approx. 60-65% vs today's 40% maximum). SOFC technology today is being introduced in field tests (planar technology, 1 to 5 kW_{el} and demonstrators (Tubular technology, 100 to 300 kW_{el}) (Antoni, 2004).

SOFCs, named due to the application of a solid oxide as electrolyte, are electrochemical reactors for direct conversion of chemical energy of gaseous fuel and oxygen into electrical energy at high temperatures (conventionally 800 – 1000°C). Figure 1 shows the SOFCs components and schematic working principle (Antoni, 2004).

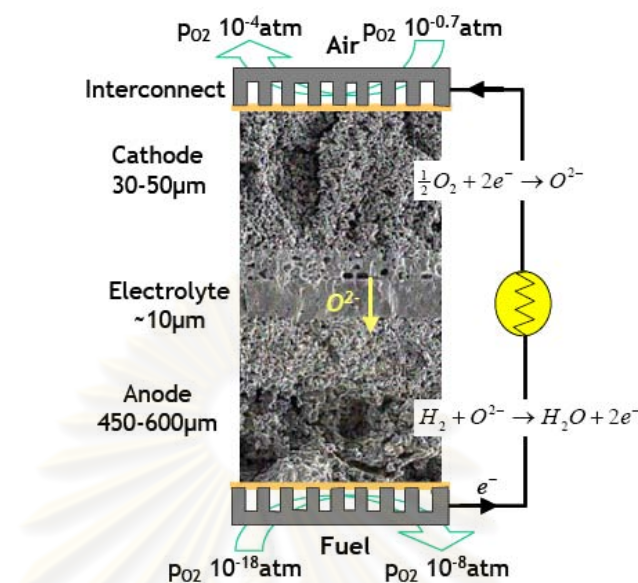
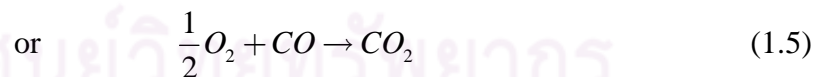
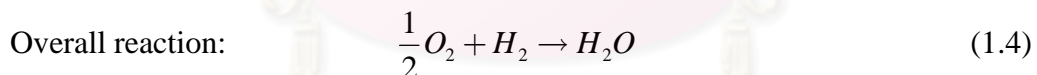
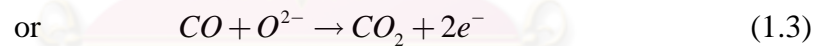
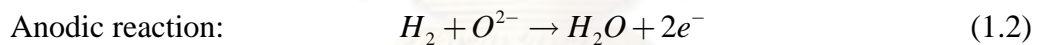
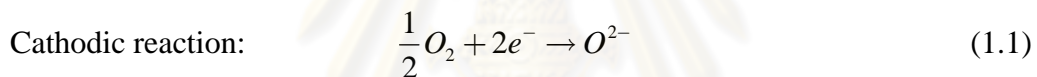


Figure 1: SOFC components and schematics working principle of SOFCs (Antoni, 2004).

A single unit of SOFC consists of a gas-tight electrolyte separating the porous cathode and anode, and an electrical interconnect which links individual cells together. Yttria doped zirconia is the popular electrolyte material because it reveals predominately ionic conductivity over a wide range of oxygen partial pressure. The most common material used for the anode side is a cermet made of nickel with the electrolyte material. At the cathode side, the cathode material should be electronically conductive. Perovskite structured ceramic has then been the best choice, in particular the strontium doped lanthanum manganite (LSM), because this material exhibits an excellent thermal expansion match with the zirconia electrolyte and good performance at high temperatures. Finally, the electrical connection, called electric connector or briefly interconnect, can be a ceramic or metallic material but, at intermediate temperatures ($600^\circ - 800^\circ\text{C}$), a metallic material may offer more advantage over a ceramic material including lower cost, easier processing, better workability, improved mechanical strength, higher electronic conductivity, higher thermal conductivity, etc., (Antoni 2004). The effort in several researches (Antoni, 2004; Chandra-ambhorn, 2006; Fergus, 2005; Geng, 2006; Kofstad, 1992; Piccardo, 2006) were, as well as this

study, dedicated to study metallic interconnects which will be mentioned subsequently.

For the working principle of SOFCs, when oxygen in air is flowed in the cathode cavity, oxygen will be reduced at the cathode/electrolyte interface to form oxide ion. In the other hand, several types of fuel, for example hydrogen or methane or biogas, may be fed at the anode side. Hydrogen in the fuel gas is oxidised at the triple phase boundaries (TPB) (electrolyte/anode/fuel) and react with the oxygen ions which migrate from the cathode side through the electrolyte to the electrolyte/anode interface. Electrons are then liberated to flow from the anode to the interconnect and to external circuit then to the cathode for the complete electrical circuit. This mechanism is efficiently described to understand by the following chemical reactions (Antoni, 2004):



The equations (1.3) and (1.5) are frequently used for the case of the presence of CO at the anode side.

1.1.2 Biogas-fuelled SOFCs

Due to their operation, hydrogen is usually fuelled in anode side and air is generally used for the cathode side. However, not only pure hydrogen can be used as fuel, but ordinary fossil-based as well as other alternative fuels can also be supplied (Herle, 2004).

In research of fuel gas, the biogas, one of attractive type of fuel gas, has been considered as a superior choice for anode side due to its primitive and renewable nature (Herle, 2003, 2004-I, 2004-II; Norheim, 2004). The biogas typically refers to a gas produced by the biological breakdown of organic matter in the absence of oxygen. In addition, biogas fabrication is a friendly and sensible way to process waste streams of variable nature (sewage sludge, liquid organic industrial effluents, farm residues, landfill, municipal and industrial solid organic residues).

At the laboratory scale, it has been recently reported by Girona et al. (Girona, 2006) that the electrical performance of a single stack under simulated biogas is very close to its characteristic performance under hydrogen (207 mW.cm^{-2} and 245 mW.cm^{-2} respectively). Nevertheless using biogas as a fuel is a good agreement, but the corrosive environment between carbon-containing atmosphere and SOFC components should be also considered.

The biogas is produced from different sources, for example, landfills, sewage, sludge, and biowaste digesters during anaerobic degradation of organic materials. Biogas generally contains approximately 50%-70% of methane, 30%-40% of carbon dioxide and others. Depending on the resource, Rasi et al. (Rasi, 2007) have determined the major and trace organic compounds in biogas and the variation in biogas composition in three different types of biogas producing plants: a municipal landfill, a sewage digester, and farm biogas plant. Compositions of the biogas from different sources are shown in Table 1.1.

Table 1.1: Contents of methane, carbon dioxide and other species in biogas from different biogas producing plants (Rasi, 2007).

Biogas	CH₄ (%)	CO₂ (%)	O₂ (%)	N₂ (%)	H₂S (ppm)	Benzene (mg m⁻³)	Toluene (mg m⁻³)
Landfill	47-57	37-41	<1	<1-17	36-115	0.6-2.3	1.7-5.1
Sewage digester	61-65	36-38	<1	<2	b.d*	0.1-0.3	2.8-11.8
Farm biogas plant	55-58	37-38	<1	<1-2	32-169	0.7-1.3	0.2-0.7

*b.d- Below detection limit 0.1 ppm

According to Table 1.1, the highest methane content, 65%, was detected in the gas from sewage digester and the lowest, 47%, from landfill. Whereas, maximum content of CO₂ detected in landfill was 41%. Many volatile organic compounds (VOCs), for example, benzene and toluene, harmful to the environment and human, possibly occurred in biogas because waste which entered the plant was probably from industries and mostly consisted of natural component of crude oil widely used in industries. Table 1.1 also reveals that the level of oxygen in biogas was less than 1% because the occurrence of high amount of air in biogas can increase of risk of explosion.

1.1.3 Metallic interconnects

For the last decade, metals have played an important role to be used for interconnects in SOFCs at intermediate temperatures (600-800°C) but the most influential problems were their reactivity, especially the formation of oxide scales on the surface in contact with anode and cathode side service environments. In theory, the use of alloys with high temperature oxidation resistant property and high electronic conductivity property might be considered but unfortunately these properties are inversed.

There are many conventional high temperature metal alloys available for consideration. Such alloys generally contain chromium and/or aluminium and/or silicon as alloying additions relying on the formation of protective scales of chromia (Cr₂O₃), alumina (Al₂O₃) or silica (SiO₂). However, alumina and silica act as insulating materials, leading to very high area specific resistance (ASR) value. Therefore, most studies on metallic material at high temperature for SOFC interconnect deals with chromia forming alloys. Its electronic conductivity (10^{-3} – 10^{-2} S.cm⁻¹ at 800°C) is orders of magnitude larger than that of alumina and silica (Antoni, 2004).

Moreover, the oxide scale should be adherent to the substrate. This is to provide the durability of interconnect stainless steels for long-term service. Indeed,

oxide spallation can lead to the physical separation between metal and oxide scale, acting as infinite electrical insulator.

However, it is not only the growth oxide scale of chromia that is a main problem for SOFCs interconnects but also volatilisation of high valence Cr(VI)-species at the cathode side in the form of CrO_3 , and/or $\text{CrO}_2(\text{OH})_2$ at working temperatures (the second one enhanced by the presence of humidity) so such poisoning is most likely to occur within the cathode (Fergus, 2005).

Some minor addition elements are required to satisfy the desired properties. For SOFC interconnects, key properties are reactivity with service environment and electrical conductivity. Small additions (0.1%) of oxygen-active elements such as yttrium, cerium and other rare earth metals may improve growth scale behaviour (Kofstad, 1988). There are several advantages of these elements on the oxidation behaviour: (I) the growth rate of chromia is reduced. (II) the adherence of chromia to the alloy substrate is improved and (III) the scale is more dense (Kofstad, 1992).

As well as manganese (Mn) or titanium (Ti) additions, the formation of Mn–Cr spinel phase (MnCr_2O_4) can reduce chromium evaporation by lowering the activity of Cr_2O_3 (Gordon, 2006) whereas rutile (TiO_2), which can form in the outer portion of the scale may also reduce chromia volatilization. Geng et al. (Geng, 2006) showed that the effect of Mn and Ti content on the oxidation kinetics of ferritic stainless steels was important. The higher content of Mn and Ti were in the alloy, the larger the weight gain. In addition, molybdenum and tungsten were added to better match the coefficient of thermal expansion (CTE) of the alloy to those of the other fuel cell components (Fergus, 2005).

Presently, numerous commercial alloys based on the systems NiCr, NiFeCr or FeCr are available for consideration. Nickel–based alloys present high mechanical strength and high surface stability but they reveal higher CTE than those of the other fuel components. Thus, this is the significant advantage of ferritic stainless steels over nickel–based alloys for application as SOFCs interconnects. Moreover, because of low–cost methods of production, ferritic stainless steels are the most attractive materials for metallic interconnects (Fergus, 2005).

In addition, when using methane or biogas as an anodic fuel, an additional requirement is that the high temperature alloy should also exhibit carburisation resistance in the zone of gas inlet. Oxide scales of chromia are generally used under these conditions, but chromia scales are not completely dense and impervious to carbon or carbon-containing molecules. Chromia-formers have shown to provide a long term protection when their scales are formed by pre-oxidizing the alloys prior to the exposure to carburising conditions. Example of alloys such as G4857(HP), G48485 HK-40), 36XM(HP-mod), i.e. iron-nickel-chromium alloys, are available for this case (Kofstad, 1992).

Nevertheless, ferritic stainless steels have been considered as attractive materials to be used as interconnect subjected to simulation biogas by Jian et al. (Jian, 2003). Unclad and Ni-clad ferritic stainless steels were exposed to carburisation atmosphere for 1000h. Their results showed that there was no benefit from Ni cladding the surface of the steel because Ni cladding was deleterious, raising carbon diffusion into bulk and forming some metal carbide in ferrite grains and at the grain boundaries.

In the recent years, 18 Cr-ferritic stainless steels have been evaluated for the application of SOFCs interconnects in synthetic air and humidified hydrogen by Chandra-ambhorn (Chandra-ambhorn, 2006). AISI441 was selected for using as interconnect but it appeared necessary to improve electrical conductivity of the formed scales. Their report concluded that TiN-coated AISI 441 exhibited the best optimised properties to be applied as SOFC interconnect.

1.2 Objective of Research

According to Chandra-ambhorn's thesis (Chandra-ambhorn 2006), AISI441 grade was proposed as the best optimized grade to be applied as SOFCs interconnect, relying on the evaluations in term of oxidation kinetics, adhesion and electrical conductivity tested in simplified atmospheres: synthetic air and humidified hydrogen as fuel. According to high cost of Crofer, AISI441 instead of Crofer tends to be used as SOFC interconnect with the surface modification.

Currently, performance of the single cell operated under biogas has been tested at several laboratories. Study of the performance of stainless steel interconnects subjected to biogas atmospheres is now required to complete the understanding of the behaviour of all SOFC components subjected to biogas before the surface modification.

Therefore, the present work is associated with the application of conventional ferritic stainless steels (primary AISI 441) as SOFCs interconnect. Specific interconnect stainless steel Crofer22APU is also studied as a reference materials.

The aim of this research is to study the reactivity of ferritic stainless steels subjected to simulated biogas atmospheres in order to understand the corrosion mechanism and relates to their corrosion behaviour as interconnectors in SOFCs at high temperature in synthetic biogas.

1.3 Research Scope

This research will be studied and investigated in term of thermodynamic calculations, and physico-chemical characterisation. The first physico-chemical characterisation is to study the oxidation kinetics of ferritic stainless steels in pure CO₂ atmosphere at temperature range of 800–1000°C. The study of the corrosion behaviour in synthetic biogas atmosphere (CH₄+CO₂) will be accomplished subsequently.

1.4 Advantage of Research

The study of the reactivity of ferritic stainless steels exposed to synthetic biogas at high temperatures will provide the knowledge to understand the mechanism and behaviour of corrosion in order to develop and/or modify the surface of stainless steels for SOFC applications.

1.5 Research planning

Task/Quarter	1	2	3	4	5	6	7	8	9	10	11	12
1. Literature reviews	■	■	■	■	■	■	■	■	■	■		
2. Thermodynamic calculation	■	■										
2. Kinetics of steels in CO ₂		■	■	■								
3. Kinetics of steels in biogas			■	■	■	■						
4. Surface characterization					■	■	■	■				
5. Discussion & Conclusion									■	■	■	■
6 Redaction									■	■	■	■

ศูนย์วิทยทรัพยากร
จุฬาลงกรณ์มหาวิทยาลัย

Chapter II

Literature review

The basic ideas of thermodynamics and kinetics of high temperature corrosion will be summarized in the following. The detail of these subjects can be found in many standard textbooks (Birks, 1983; Dehoff, 2006; Kofstad, 1988; Lupis, 1993; Sarrazin, 2000).

2.1 Thermodynamics Considerations

General chemical reaction may be given as

$$\sum_{i=1}^r \nu_i A_i = 0 \quad (2.1)$$

Where A_i s represent reactants or products and ν_i s are stoichiometric coefficients which are the numbers to balance stoichiometrically the reaction. They are considered as algebraic: positive for the products and negative for the reactants. The increments in the mol number, dn_i , of the substance A_i produced by reaction are related to each other by following relations

$$\frac{dn_1}{\nu_1} = \frac{dn_2}{\nu_2} = \dots = \frac{dn_r}{\nu_r} = d\lambda \quad (2.2)$$

where λ is a parameter designating the progress variable of the reaction.

The Gibbs free energy of a system with the variables of temperature, pressure and the mol number of its components may be given by the equation

$$dG = -SdT + VdP + \sum_{i=1}^r \mu_i dn_i \quad (2.3)$$

Corresponding equation (2.2), equation (2.3) become

$$dG = -SdT + VdP + \left(\sum_{i=1}^r \nu_i \mu_i \right) d\lambda \quad (2.4)$$

where μ_i is the chemical potential or partial molar Gibbs free energy of component i

At constant pressure and temperature, the criterion of spontaneous reaction is

$$(dG)_{P,T} \leq 0 \quad (2.5)$$

By definition
$$\Delta G = \sum_{i=1}^r \nu_i \mu_i \quad (2.6)$$

By equation (2.4) and (2.5), therefore the criterion of spontaneous reaction become

$$\Delta G d\lambda \leq 0 \quad (2.7)$$

The meaning of this inequality is that at constant temperature and pressure the possible process can occur if the variations must be such that

$$(dG)_{P,T} = \Delta G d\lambda \leq 0 \quad (2.8)$$

If ΔG is negative, $d\lambda$ must be positive and the reaction will be proceeded forward. Contrarily, if ΔG is positive, $d\lambda$ must be negative and the reaction will be proceeded backward.

The chemical potential or partial molar Gibbs free energy of specie i is more practical to analyze it in term of activity as follow

$$\mu_i = \mu_i^0(T) + RT \ln a_i \quad (2.9)$$

where a_i is the activity of component i at temperature T and μ_i^0 is chemical potential at standard state.

From equation (2.6), the equation (2.9) yields

$$\begin{aligned} \Delta_r G - \Delta_r G^0 &= \sum_{i=1}^r \nu_i (\mu_i - \mu_i^0) \\ &= RT \sum_{i=1}^r \ln a_i \end{aligned} \quad (2.10)$$

The equation (2.10) can be rewritten between products ($\nu_i > 0$, $i = 1, 2, 3, \dots$, k) and the reactants ($\nu_i < 0$, $i = k+1, k+2, k+3, \dots$, r) as follows

$$\Delta_r G - \Delta_r G^0 = RT \ln Q \quad (2.11a)$$

$$Q = \frac{(a_1)^{\nu_1} (a_2)^{\nu_2} (a_3)^{\nu_3} \dots (a_k)^{\nu_k}}{(a_{k+1})^{|\nu_{k+1}|} \dots (a_r)^{|\nu_r|}} \quad (2.11b)$$

Since at equilibrium $\Delta_r G = 0$, Q takes the equilibrium value designated by K

$$(Q)_{eq} = K \quad (2.12)$$

Hence the equation (2.11) can be written

$$\Delta_r G^0 = -RT \ln K \quad (2.13)$$

K is called the equilibrium constant and depends on the Gibbs free energy at standard state and temperature. If $Q > K$ the reaction proceeds backward, conversely, if $Q < K$ the reaction proceeds forward.

Considering multicomponent system, Gibbs free energy of mixing, designated G^M , was rewritten as equation following

$$G^M = \sum_{i=1}^n n_i \mu_i \quad (2.14)$$

Applying this equation with equation (2.9), equation (2.14) becomes

$$G^M = RT \sum_{i=1}^n n_i \ln a_i \quad (2.15)$$

or in the term of molar Gibbs free energy, G_m^M , equation (2.15) may be rewritten

$$G_m^M = RT \sum_{i=1}^n X_i \ln a_i \quad (2.16)$$

where X_i is mole fraction ($X_i = \frac{n_i}{\sum_{i=1}^n n_i}$)

However, for general solution, Gibbs free energy of mixing consists of three contributions: the reference term, the ideal term, and the excess term. In a simple substitutional solution (only one lattice site with random occupation), the well-known Redlich-Kister-Muggianu polynomial is then used for the excess term. The equation (2.16) therefore becomes:

$$G_m^M = \sum_{i=1}^n X_i \mu_i^0 + RT \sum_{i=1}^n X_i \ln a_i + \sum_i \sum_{\prec j} X_i X_j \sum_{v=0}^{n_{ij}} L_{ij}^v(T) (X_i - X_j)^v + \sum_i \sum_{\prec j} \sum_{\prec k} \left[X_i X_j X_k \frac{(X_i L_i^{ijk}(T) + X_j L_j^{ijk}(T) + X_k L_k^{ijk}(T))}{(X_i + X_j + X_k)} \right] \quad (2.17)$$

where $L_i^v(T)$ is Redlich – Kister coefficient in function of temperature

It is necessary to minimize the total Gibbs energy of all the phases for the calculation of phase equilibria in a multicomponent system. Hence

$$G = \text{minimum or } dG = 0$$

However, the total Gibbs free energy has nowadays been determined by the various softwares such as FactSage, Thermocalc or other.

In its most complete form these software incorporate a database with enthalpies and entropies of formation of a large number of molecular components. The database is input to the program in the system and a range of temperatures that are of interest in the problem. The most software will be proceed as follows (Dehoff, 2006)

a) Development of a list of the molecular components in its database that may form from the elements that are input.

b) Construction of a list of independent balanced chemical reactions among these components by relation of $r = c - e$ (where r is a number of independent conservation reaction, c is components in system, and e is elements in systems).

c) Retrieval of enthalpies and entropies for these reactions in its database.

d) Computation of ΔG_i^0 values for each reaction at a temperature of interest.

e) Calculation of the corresponding equilibrium constant K_i .

f) Analysis of this set of equations for the compositions of each of the components at equilibrium.

Mathematical method was used to derive some data base of Gibbs free energy in FACTSAGE to thermodynamic consideration. Figure 2.1 shows the schematic diagram of FactSage algorithm which uses the method of minimization of Gibbs free energy.

ศูนย์วิทยทรัพยากร
จุฬาลงกรณ์มหาวิทยาลัย

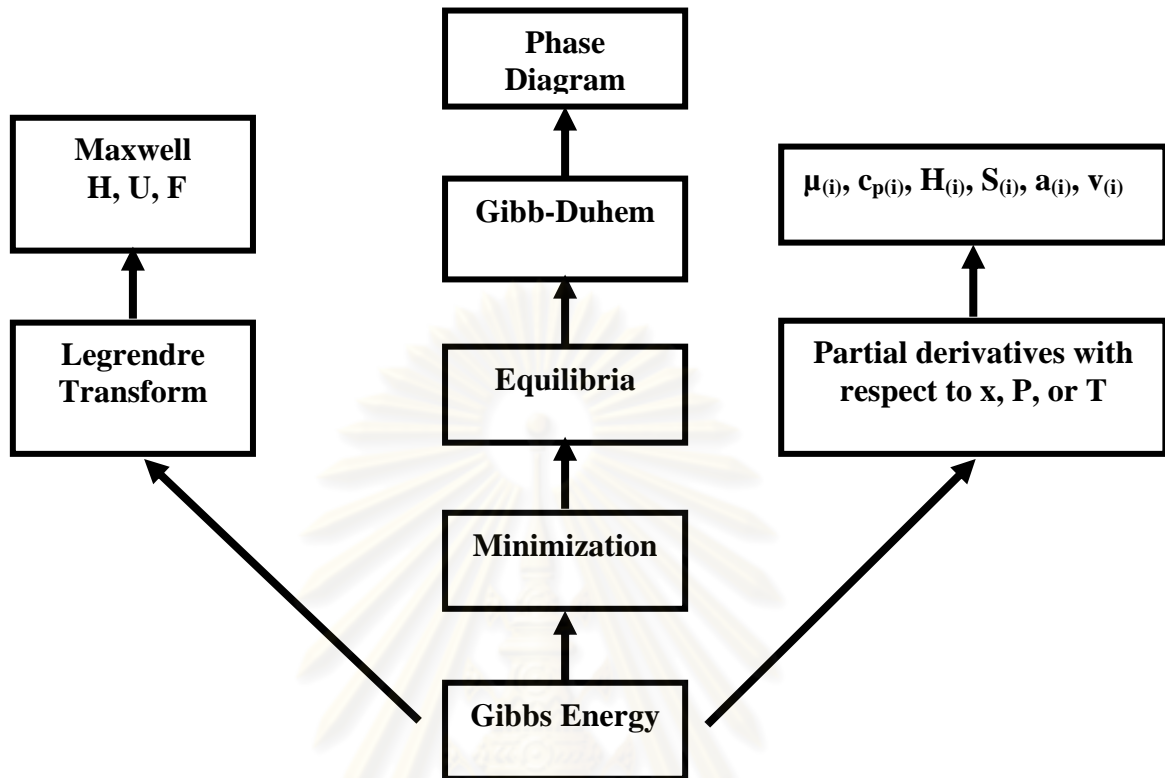


Figure 2.1: Schematic diagram of theoretical background of FACTSAGE (Factsage).

2.1.1 Thermodynamics of gaseous atmospheres

Recalling equation (2.9), activity of gas is substituted by the variable called “fugacity, f ”. The equation (2.9) then become

$$\mu_i = \mu_i^0(T) + RT \ln \frac{f_i}{f^0} \quad (2.14)$$

It is convenient to consider the value of the fugacity in the standard state of gas (f^0) to be equal to 1. At the state of gas less than 1 atm, the gas will behave as perfect gas. The fugacity of gas will be then written in term of partial pressure of gas ($f = p_i$) (if P_t is the total pressure in the system: $p_i = X_i P_t$, X_i is mole fraction of the specie of gas). The equation (2.14) can be rewritten as

$$\begin{aligned} \mu_i &= \mu_i^0(T) + RT \ln p_i \\ &= \mu_i^0(T) + RT \ln X_i P_t \end{aligned} \quad (2.15)$$

At equilibrium state, by substituting equation (2.15) in the equation (2.11) for general reaction of gas mixture, it comes

$$\Delta_r G^0 = -RT \ln \frac{\prod_{i=1}^k p_i^{\nu_k}}{\prod_{i=k+1}^r p_i^{|\nu_{k+1}|}} \quad (2.16)$$

However, in the case of complex gas in atmospheres, it is necessary to use the method of Gibbs energy minimization with thermodynamic calculation program. Special program such as CHEMSAGE/FACTSAGE and GEMINI have been developed to calculate the equilibrium composition of the gaseous phase.

In case of biogas atmospheres, the principal components are methane and carbon dioxide. Three possible reactions involved in the production of hydrogen for SOFC are shown as follows



The equation (2.17) is called reaction of dry reforming of methane. When the SOFC is operated using an oxygen ion-conducting electrolyte, water is also generated by the electrochemical reaction of hydrogen and oxygen ion and therefore, the steam reforming of methane (equation (2.18)) and the water gas shift reaction (equation (2.19)) also take place. However feeding biogas rather than hydrogen, important problems remain to be solved. One of them is the problem of carbon deposition on the anode and interconnects. The following reactions are the most possible carbon formation reactions in the system:



All reactions are used to examine the thermodynamic possibility of carbon formation by calculating the value of their carbon activity (a_c). When $a_c > 1$, carbon formation is observed. Whereas $a_c < 1$, carbon formation is thermodynamically impossible.

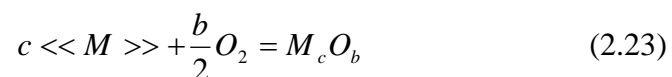
A number of efforts have been carried out to diminish the possibility of carbon deposition in industrial systems. Some additives such as molybdenum or cerium metal oxides, to the Ni-based anode or stream, were added to reduce carbon deposition (Assabumrungrat, 2006; Finnerty, 2000; Piroonlerkgul, 2008).

Assabumrungrat et al. (Assabumrungrat, 2006) have reported with their calculations that carbon activity decreased dramatically with increasing CO_2/CH_4 ratio and in addition, steam showed a more pronounced influence on inhibiting the carbon formation than carbon dioxide particularly at low operating temperatures.

As well as the report of Piroonlerkgul et al. (Piroonlerkgul, 2008), a reforming agent (steam or air) is required to inhibit the carbon formation when temperature increases. Their calculations showed that the mol number of reforming agent required per mole number of biogas required decreased almost hyperbolically with temperature, attaining nearly constant value beyond about 1173 K. However, when the amount of reforming agent increases, the electrical efficiency always decreases. In addition, steam is considered to be the most suitable reforming agent as the steam-fed SOFC offer much higher power density than the air-fed SOFC.

2.1.2 Thermodynamics of metal oxide formation

Considering the equilibrium between metal, its oxide, and gaseous phase of oxygen, the reaction can be written



where $\ll M \gg$ = metal in alloy

The Gibbs free energy of formation of a metal oxide is given by

$$\Delta_r G_f = \Delta_r G_f^0 + RT \ln \left(\frac{a_{M_c \text{O}_b}}{a_{\ll M \gg}^c a_{\text{O}_2}^{b/2}} \right) \quad (2.24)$$

At equilibrium, $\Delta_r G_f = 0$, the equation(2.24) is then

$$\Delta_r G_f^0 = -RT \ln \left(\frac{a_{M_c O_b}}{a_{\langle\langle M \rangle\rangle}^c a_{O_2}^{b/2}} \right) \quad (2.25)$$

The unit activity of metal oxide and ideal gas are assumed.

Then,

$$\Delta_r G_f^0 = -RT \ln \left(\frac{1}{a_{\langle\langle M \rangle\rangle}^c P_{O_2}^{b/2}} \right) \quad (2.26)$$

$\Delta_r G_f^0$ is the standard Gibbs free energy of formation of metal oxide,

To assess derivations from ideality, it is convenient to introduce a correction factor to strict proportionally between the activity of metal in alloy ($a_{\langle\langle M \rangle\rangle}$) and mol fraction of metal in alloy ($X_{\langle\langle M \rangle\rangle}$). The correction factor is called the activity coefficient and is designated by $\gamma_{\langle\langle M \rangle\rangle}$. It can be defined by

$$a_{\langle\langle M \rangle\rangle} = \gamma_{\langle\langle M \rangle\rangle} X_{\langle\langle M \rangle\rangle} \quad (2.27)$$

In the case of an ideal solution, $\gamma_{\langle\langle M \rangle\rangle} = 1$ at all concentrations. In real solutions, it is a function of composition, temperature, and pressure and its deviation from the value of 1 will measure the deviation of the solution's behaviour from the ideal model.

In multicomponent system, Gibbs-Duhem equation may be devised for the activity coefficient by the equation (2.28),

$$\sum_{i=1}^r X_i d\mu_i = 0 \quad (2.28)$$

For binary system, the Gibbs-Duhem equation become

$$X_1 d \ln \gamma_1 + X_2 d \ln \gamma_2 = 0 \quad (2.29)$$

Integrating equation (2.29) from $X_2 = 1$ to X_2 , it comes

$$\ln \gamma_2 = - \int_{X_2=1}^{X_2} \frac{X_1}{X_2} d \ln \gamma_1 \quad (2.30)$$

In the Knudsen cell-mass spectroscopy method for studying the thermodynamic properties of a binary solution, the experimentally measured quantity is proportional to the ratio of the activities of the two components. Knowing their concentrations, we deduce a quantity proportional to the ratio of the activity

coefficients of the two components. The integration of Gibbs-Duhem equation may then be rewritten

$$\ln a_2 = -\int_{X_2=1}^{X_2} X_1 d \ln \left(\frac{a_1}{a_2} \right) \quad (2.31)$$

As the activity of a component is directly proportional to its partial pressure (assuming ideal gas behaviour), it is directly proportional to the measured ion current. Hence,

$$\ln a_2 = -\int_{X_2=1}^{X_2} X_1 d \ln \left(\frac{I_1^+}{I_2^+} \right) \quad (2.32)$$

The partial pressure of a species within the Knudsen cell is given in such mass spectrometric studies by the expression

$$P_i = \frac{I_i^+ TK}{\sigma_i \beta_i} \quad (2.33)$$

where I_i^+ is the ion current, T is the temperature of the cell, σ_i is the relative ionization cross section, β_i is the relative detector sensitivity, and K is a constant.

A form which is more suitable for graphical integration is obtained by deducting from equation (2.32) the following expression which is obtained from the relationship between the mol fractions. This yield

$$\ln \gamma_2 = -\int_{X_2=1}^{X_2} X_1 d \left[\ln \left(\frac{I_1^+}{I_2^+} \right) - \ln \left(\frac{X_1}{X_2} \right) \right] \quad (2.34)$$

$\ln \gamma_2$ is obtained through a plot of X_1 vs $-\left[\ln (I_1^+/I_2^+) - \ln (X_1/X_2) \right]$. This integration technique is due to Belton and Fruehan (Belton, 1967)

a) Ellingham-Richardson diagram

According to equation 2.26, by assuming the unity of activity of the pure solid phases, the oxide will be formed only if the ambient oxygen pressure is larger than the dissociation pressure of the oxide in equilibrium with the metal. The equation 2.26 may be rewritten

$$P_{O_2,eq} = \exp\left(\frac{2\Delta_r G_f^0}{bRT}\right) \quad (2.35)$$

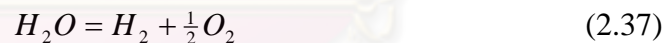
It means that a metal can be oxidized to the oxide if $P_{O_2} \geq P_{O_2,eq}$. The $P_{O_2,eq}$ is classically plotted in logarithm scale as a function of temperature to simply consider the stability of oxide formation. This diagram is well-known as Ellingham-Richardson diagram as shown in Figure 2.2. Along the ordinates are plotted values of $\Delta_r G_f^0$ for the oxides and of the partial molar free energy of oxygen, $\Delta_r G_f^0$ refer to the standard free energy of formation of the oxides per mole of oxygen. The most stable oxides have the largest negative value of $\Delta_r G_f^0$. For example, the stability of the oxide increases from Fe_2O_3 to Al_2O_3 .

In addition, this diagram is established in mixture of gases where oxygen is a component. The most important pairs of gases are in practice represented by $CO_2 + CO$ and $H_2O + H_2$.

The equilibriums for these gases mixture are



and



The corresponding partial pressure of oxygen can be expressed as

$$P_{O_2} = \left(K_1 \frac{P_{CO_2}}{P_{CO}}\right)^2 \quad (2.38)$$

and

$$P_{O_2} = \left(K_1 \frac{P_{H_2O}}{P_{H_2}}\right)^2 \quad (2.39)$$

where K_1 and K_2 are the equilibrium constants

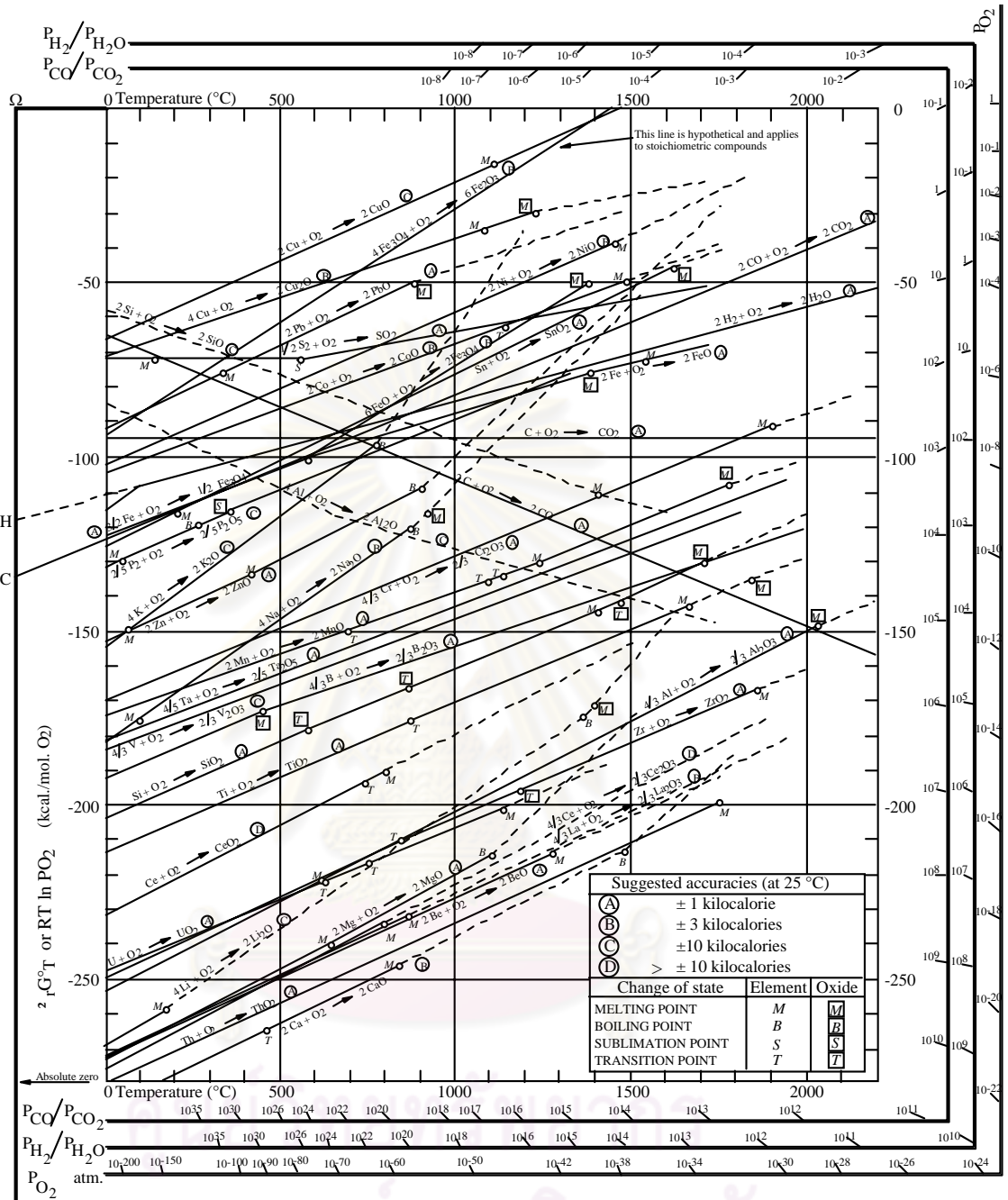


Figure 2.2: Ellingham-Richardson diagram for the oxidation of metals (Sarrazin, 2000).

b) Phase diagrams of some Fe-based alloys

The studied stainless steels investigated in the present work contains the chromium in the range of 18-20 %wt. Comparing to the diagram Cr-Fe as shown in Figure 2.3, both steels such 441 and Crofer, are therefore ferritic type.

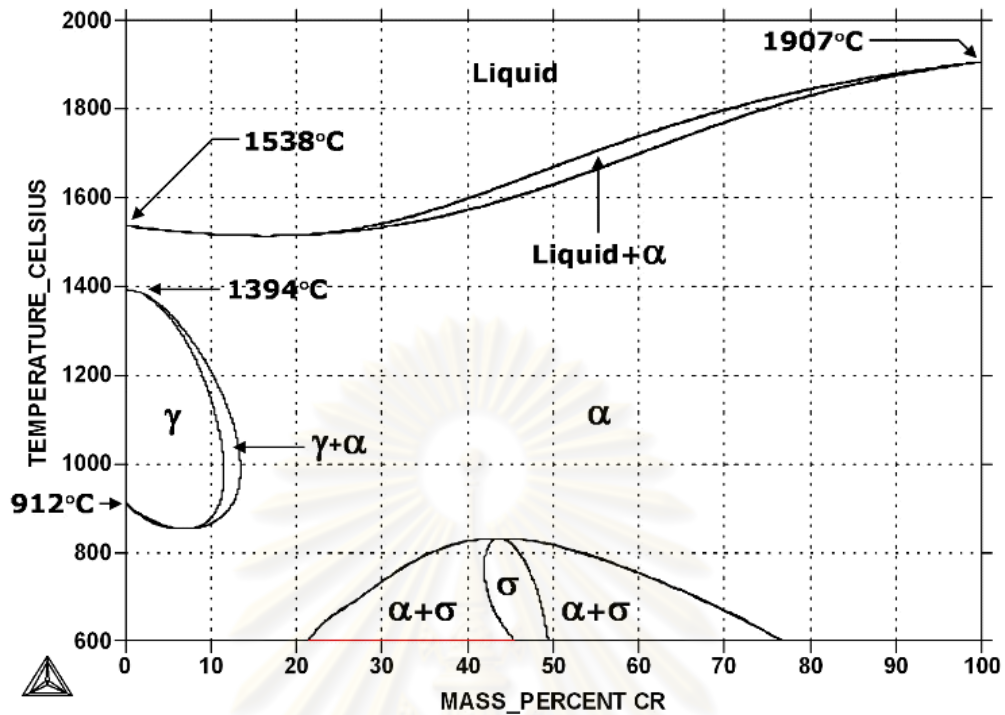


Figure 2.3: Phase equilibrium diagram of Fe-Cr (Calphad).

The minor alloying elements in the studied stainless steel are such as Mn, Nb, Ti, and La. Phase diagram of Fe-Nb and Fe-Ti are depicted in Figures 2.4 and 2.5 respectively for the studied stainless steel 441 which consist of 0.49% wt Nb and 0.16% wt Ti. From the diagram, it can be noted that some of intermetallic compounds possibly form in bulk materials, for example, Fe_2Nb (Laves phase) or Fe_2Ti .

The reactive element of Mn in alloy has been also important during oxidation. For the candidate alloys used as SOFCs component which contain Mn, the phase of spinel Mn-Cr-O was usually observed. In order to reduce the Cr evaporation, by example, such a spinel play a very important role. Jung (Jung, 2006) calculated the phase diagrams of the Mn-Cr-O system at various temperatures. The Gibbs free energy of formation of the spinel Mn-Cr-O, according to the reaction $\text{MnO} + \text{Cr}_2\text{O}_3 = \text{MnCr}_2\text{O}_4$, was optimized to be -51 kJ.mol^{-1} . These calculations confirmed the appearance of spinel phase on the Mn-Cr alloy subjected to SOFCs atmospheres with the partial pressure of oxygen in range of 10^{-33} bar at 900°C . The

phase diagram of Mn-Cr at 900°C is shown in Figure 2.6. The existence of this compound will be essentially discussed later.

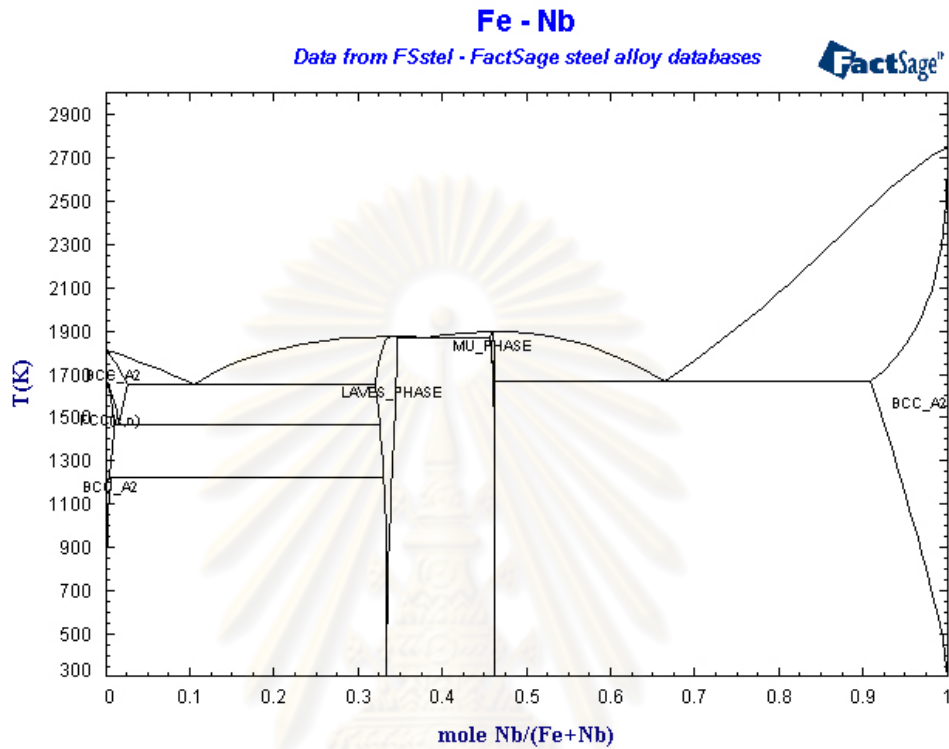


Figure 2.4: Phase equilibrium diagram of the Fe-Nb system (Factsage).

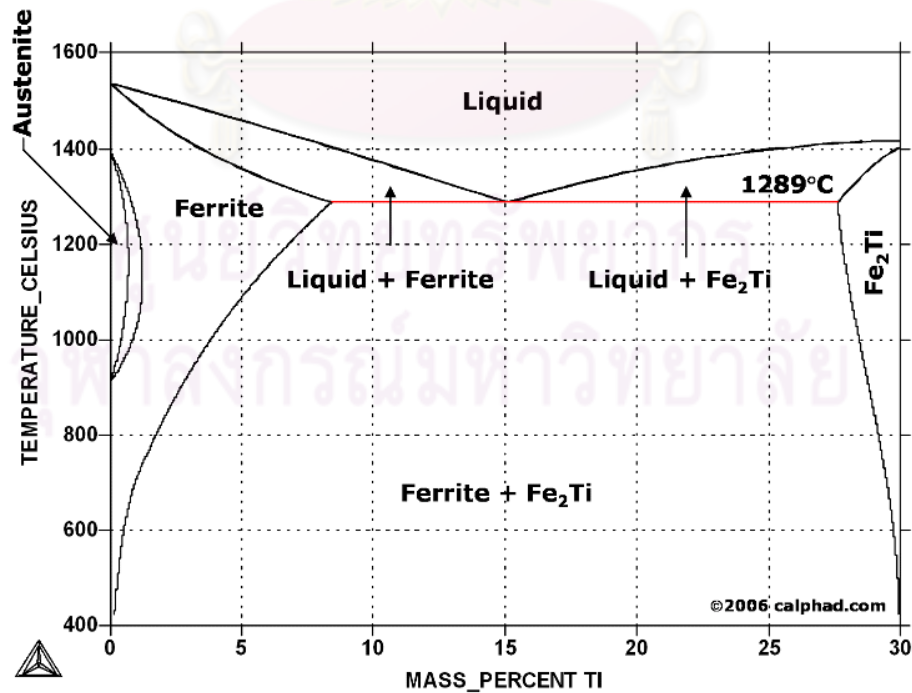


Figure 2.5: Phase equilibrium diagram of the Fe-Ti system (Calphad).

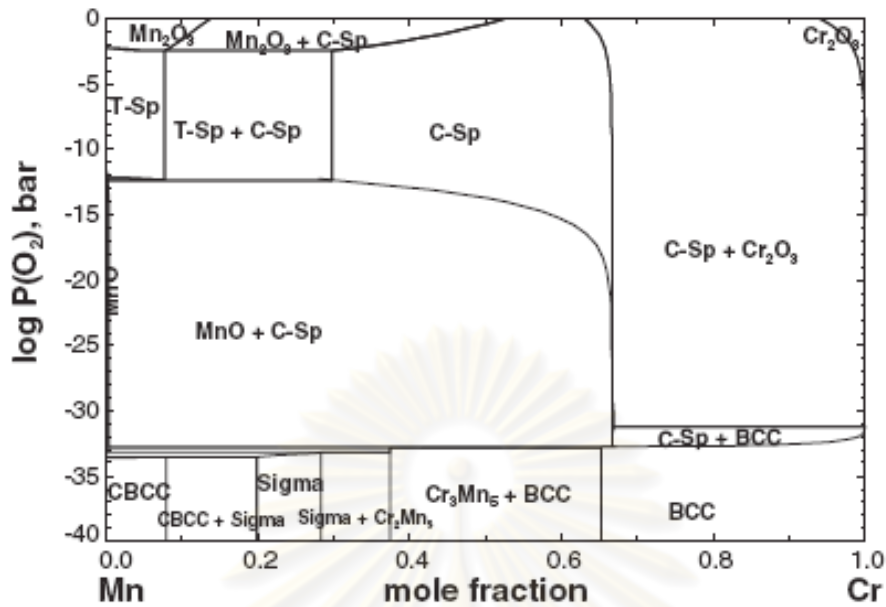


Figure 2.6: Phase equilibrium diagram of the Mn-Cr-O system at 900°C (Jung, 2006).

c) Stability diagram in carburization

Due to carbon containing in the biogas atmospheres, carburization process must be necessarily included. Biogas environments are characterized by low oxygen activities and relatively high carbon activities. The knowledge of stabilities of relevant carbides, of metal - carbon phase diagrams and of appropriate phase stability diagrams serve as important bases for interpretations of the possible reactions.

The Ellingham/Richardson diagram for some metal carbides of importance in carburization of metals was calculated by FactSage in Figure 2.7. The carbides show increase in stability (at carbon activity equal to one) from Fe_3C to TiC . The interpreted observation shows that Fe_3C is stable at temperature above 1080 K only.

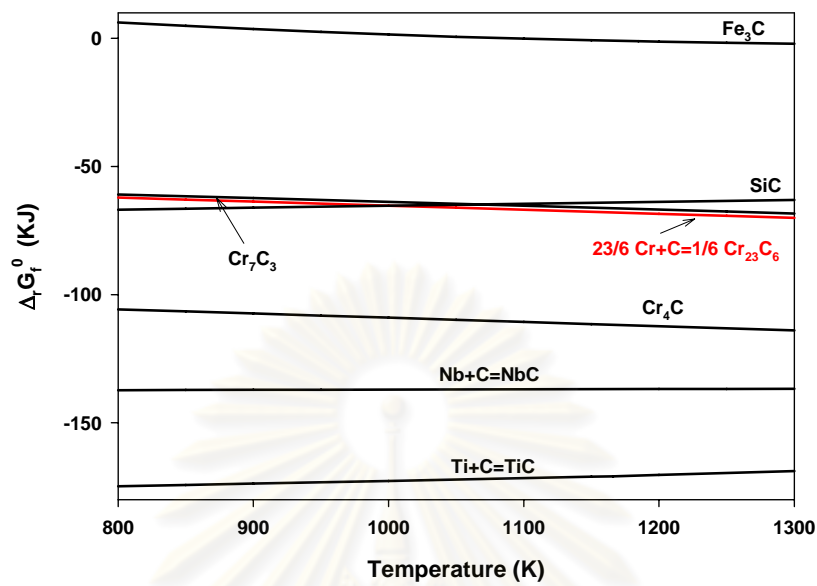


Figure 2.7: The standard free energy of formation of some carbides as a function of temperature (Factsage).

In atmospheres containing both carbon and oxygen, the reaction products may either be oxide or carbide. The Cr-O-C diagram at 800°C is revealed in Figure 2.8. It can be noted that, if the oxygen activity is sufficiently low, no oxide may be formed, however, chromium carbide will possibly appear.

ศูนย์วิทยทรัพยากร
จุฬาลงกรณ์มหาวิทยาลัย

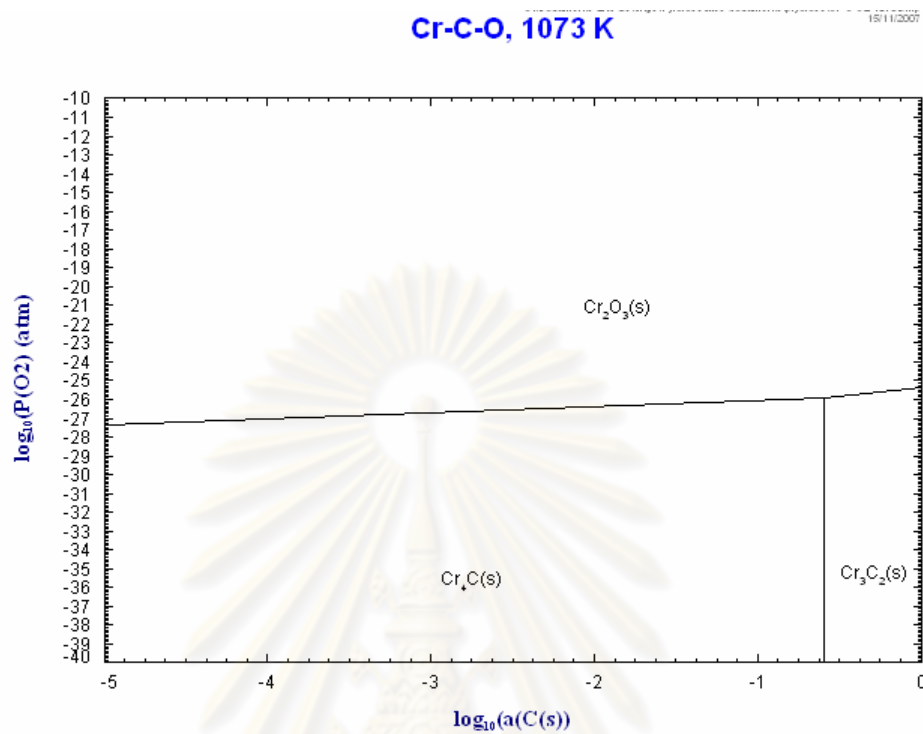


Figure 2.8: The Cr-C-O phase stability diagram at 1073 K (Factsage).

2.2 High Temperature Corrosion

2.2.1 Oxidation mechanisms

Understanding the mechanisms of corrosion reactions at high temperatures requires important knowledge such solid state diffusion and heterogeneous reaction kinetics. Several authors have extensively studied these points and provided this knowledge as detailed briefly in the following summary (Kofstad, 1988; Mrowec, 1980; Sarrazin, 2000; Wyckoff, 1964).

2.2.1.1 Defect and diffusion in corundum structure

A few studies (Antoni, 2004; Chandra-ambhorn, 2006; Fergus, 2005) have reported that the corundum structure of chromium oxide (Cr_2O_3) is the

major oxide phase occurring during oxidation of the conventional ferritic stainless steels. The following detail will be therefore emphasized in only Cr_2O_3 subject.

2.2.1.1.1 Corundum structure

In the corundum structure, the anions (O^{2-}) form a closely packed hexagonal lattice in which the cations (Cr^{3+}) occupy $2/3$ of all octahedral positions in the crystal structure. The coordination number of the cations is six, three O ions at distance of 1.97×10^{-10} m and three more separated with $\text{Cr-O} = 2.02 \times 10^{-10}$ m, and the coordination number of the anions is four. The symmetry is rhombohedral with the distance of unit of 5.35×10^{-10} m and a unit containing two molecules (Wyckoff, 1964). The corundum structure is shown in Figure 2.9.

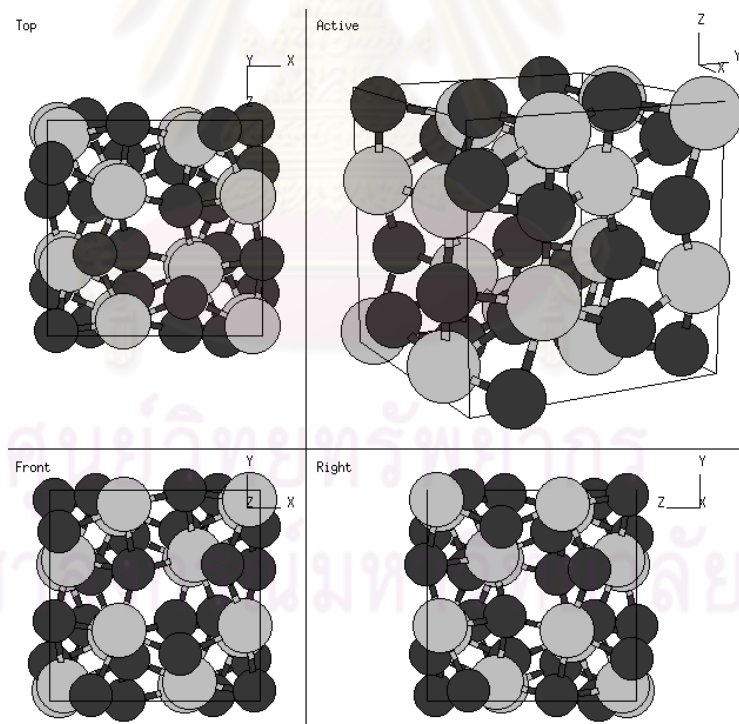


Figure 2.9: Corundum structure black: cation, gray: anion (available from http://cst-www.nrl.navy.mil/lattice/struk/d5_1.html)

2.2.1.1.2 Defects structure of pure Cr₂O₃

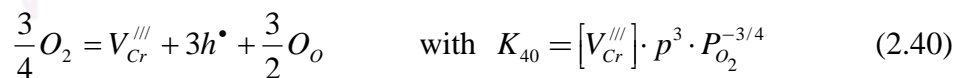
Brylewski et al. (Brylewski, 2001) have reported that Cr₂O₃ exhibits the mixed p-type and n-type properties independently on the oxidation temperature. It was discussed that the n-type behavior of the scale arises in its inner part (near the alloy/scale interface), where chromium interstitials $Cr_i^{\bullet\bullet\bullet}$ are the dominant point defects, whereas the chromium vacancies, $V_{Cr}^{\prime\prime\prime}$, as the major defects, lead to p-type behavior in the outer part of scale.

Other works reported the complex defect structures of Cr₂O₃ at temperatures higher than ca. 1000 °C and lower than ca. 1000 °C (Holt, 1994-I; Holt, 1994-II; Kofstad, 1980; Young, 1985;).

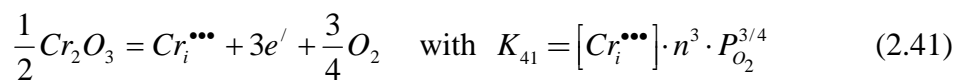
Cr interstitials $Cr_i^{\bullet\bullet\bullet}$ are the predominant Cr point defects, showing n-type behaviour, with scale oxidised in the effective partial pressure of oxygen which is close to the decomposition pressure of Cr₂O₃ in equilibrium with Cr metal. Contrarily, Cr₂O₃ is a p-type conductor at atmospheric and near-atmospheric oxygen pressure due to a higher mobility for electron hole than for electron (Kofstad, 1980; Young, 1985).

Considering formation and corresponding defect equilibria of the probable native point defects in chromia, the possible defect reactions of chromium vacancies $V_{Cr}^{\prime\prime\prime}$, chromium interstitials $Cr_i^{\bullet\bullet\bullet}$, oxygen vacancies $V_o^{\bullet\bullet}$, and oxygen interstitials $O_i^{\prime\prime}$ may be written as [Holt (1994)]

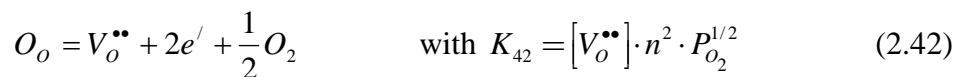
Chromium vacancies:



Chromium interstitials:



Oxygen vacancies



Oxygen interstitials:

$$\frac{1}{2}O_2 = O_i'' + 2h^\bullet \quad \text{with } K_{43} = [O_i''] \cdot p^2 \cdot P_{O_2}^{-1/2} \quad (2.43)$$

where K_{40} is the equilibrium constant of the Reaction (2.40), and similar for the others.

According to electroneutrality condition in the reactions (2.40) to (2.43), the concentrations of each ionic point defect become as follows:

$$[V_{Cr}'''] = 3^{-3/4} \cdot K_{40}^{1/4} \cdot P_{O_2}^{3/16} \quad (2.44)$$

$$[Cr_i'''] = 3^{-3/4} \cdot K_{41}^{1/4} \cdot P_{O_2}^{-3/16} \quad (2.45)$$

$$[V_O^{**}] = 2^{-2/3} \cdot K_{42}^{1/3} \cdot P_{O_2}^{-1/6} \quad (2.46)$$

$$[O_i''] = 2^{-2/3} \cdot K_{43}^{1/3} \cdot P_{O_2}^{1/6} \quad (2.47)$$

In the case that the intrinsic electronic defect is considered to be dominant, the concentrations of electrons and electron holes are given by $n = p = K_i^{1/2}$. By inserting these electronic concentrations into Equations (2.40) to (2.43), the concentrations of each ionic point defect in this case is then given as

$$[V_{Cr}'''] = K_{30} \cdot K_i^{-3/2} \cdot P_{O_2}^{3/4} \quad (2.48)$$

$$[Cr_i'''] = K_{31} \cdot K_i^{-3/2} \cdot P_{O_2}^{-3/4} \quad (2.49)$$

$$[V_O^{**}] = K_{32} \cdot K_i^{-1} \cdot P_{O_2}^{-1/2} \quad (2.50)$$

$$[O_i''] = K_{33} \cdot K_i^{-1} \cdot P_{O_2}^{1/2} \quad (2.51)$$

From Equations (1.23) and (2.44) to (2.51), the defect structure of Cr_2O_3 was proposed as in Figure 2.10 (Holt 1994). At the temperatures higher than ca. 1000 °C, it was discussed (Kofstad 1980; Holt 1994) that Cr_2O_3 behaves as an intrinsic electronic conductor in the outer part of scale. The oxygen activity of 1 bar

corresponds to the middle part of Figure 2.10. In the inner part where P_{O_2} is lower, $Cr_i^{\bullet\bullet}$ is the dominating cation with the n-type property.

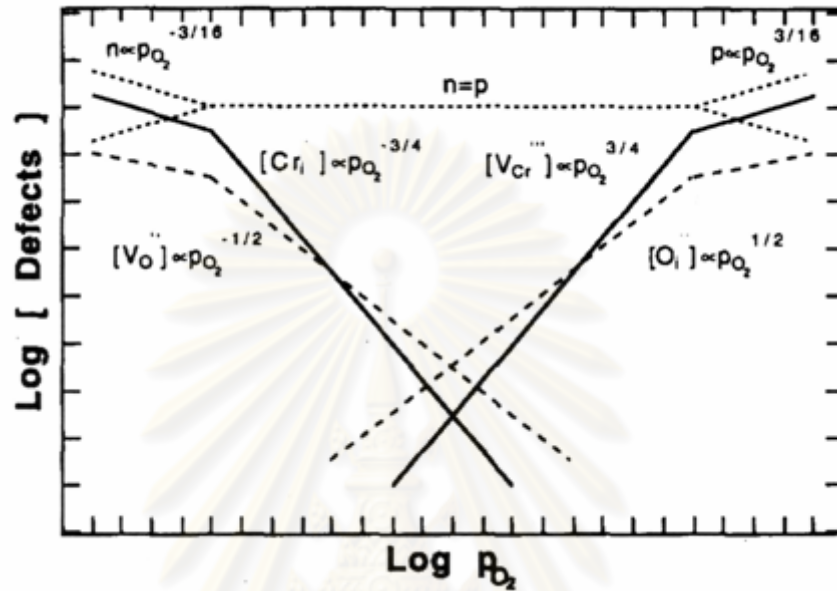


Figure 2.10: Kröger-Vink diagram for a defect structure situation in Cr_2O_3 where intrinsic electronic defects dominate at the near-stoichiometric composition (Holt, 1994-I).

It may be noted that the n-type behavior of Cr_2O_3 at the low P_{O_2} is also possible. Young et al. (Young, 1985) have concluded that the porous Cr_2O_3 equilibrated with a low oxygen partial pressure (H_2/H_2O) at 1920 K behaved as an n-type material in which Cr interstitials are the dominating point defect. However, it was also reported that stainless steels 304L oxidized in CO_2 behaved n-type property with oxygen vacancies in contrast to that observed in the oxidation of pure Cr in oxygen (Goutier, 2010).

2.2.1.2 Kinetic approach of scale formation (Sarrazin, 2000)

The kinetics of oxidation is basically followed by the change of mass in function of the oxidation time. Various types of oxidation kinetics can be experimentally observed: linear, parabolic, cubic, exponential or catastrophic type.

For the linear rate law, surface or phase boundary reaction may be the rate determining step. For the parabolic law, the thermal diffusion through the growing oxide scale is the rate determining step (Birks, 1983; Kofstad, 1988).

The oxidation mechanism in the case of a compact scale consists of an assumption of at least four basic processes as follows

- a) Oxygen adsorption on the oxide.
- b) Exchange of matter between the adsorbed phase and the oxide (external elementary step).
- c) Diffusion of matter through the oxide scale.
- d) Exchange of matter between the oxide and metal (internal elementary step).

The basic processes as mentioned above will be concisely describe as follows.

- a) Adsorption process

The most common theories and models of the adsorption process relate to monomolecular adsorption called Langmuir isotherm model (Lupis, 1993; Sarrazin, 2000). This model can be represented the variation of adsorbed volume as a function of gas pressure as shown by the following equation:

$$\theta_{eq} = \frac{s}{s_0} = \frac{K_a P}{1 + K_a P} \quad (2.52)$$

where θ_{eq} is the ratio of the number of occupied surface sites per surface area (s) and the number of initially available surface sites (s_0), K_a is the constant and P is gas pressure.

When G is the particle in the gas phase and k'_a and k''_a are constant, the sorption equilibrium may be represented by:



Basing on Eyring's theory, the rate of the sorption process is given by

$$\frac{dn_{G-s}}{dt} = k'_a (1 - \theta) P - k''_a \theta \quad (2.54)$$

b) Interfacial processes

These processes will describe in the external and internal elementary steps as the insertion of oxygen at the external interface and that of metal at the internal interface during the construction of the oxide lattice. The oxide will be considered as an ideal solution of point defects in a perfect crystal. The reactions of interfacial elementary steps depend on the predominance of native point defects. For the case of Cr_2O_3 , the predominant defect will be either the Cr vacancies V_{Cr}''' or oxygen interstitials O_i'' for a p-type semi-conductor and either Cr interstitials Cr_i''' , or oxygen vacancies V_o'' , for a n-type semi-conductor. The formulation of elementary interfacial steps is presented in Table 2.1.

Table 2.1: Formulation of elementary interfacial steps according to the nature of the predominant defects present in the Cr_2O_3 lattice.

Cr_2O_3 p-type semi-conductor		
Defect	External elementary step	Internal elementary step
V_{Cr}'''	$3O - s \xrightleftharpoons[k_e'']{k_e'} 3O_o + 2V_{\text{Cr}}''' + 6h^\bullet + 3s$	$2V_{\text{Cr}}''' + 6h^\bullet + 2\langle \text{Cr} \rangle \xrightleftharpoons[k_i'']{k_i'} 2\text{Cr}_{\text{Cr}}$
O_i''	$3O - s \xrightleftharpoons[k_e'']{k_e'} 3O_i'' + 6h^\bullet + 3s$	$2\langle \text{Cr} \rangle + 3O_i'' + 6h^\bullet \xrightleftharpoons[k_i'']{k_i'} 3O_o + 2\text{Cr}_{\text{Cr}}$
Cr_2O_3 n-type semi-conductor		
Defect	External elementary step	Internal elementary step
Cr_i'''	$3O - s + 2\text{Cr}_i''' + 6e' \xrightleftharpoons[k_e'']{k_e'} 3O_o + 2\text{Cr}_{\text{Cr}} + 3s$	$2\langle \text{Cr} \rangle \xrightleftharpoons[k_i'']{k_i'} 2\text{Cr}_i''' + 6e'$
V_o''	$3O - s + 3V_o'' + 6e' \xrightleftharpoons[k_e'']{k_e'} 3O_o + 3s$	$2\langle \text{Cr} \rangle \xrightleftharpoons[k_i'']{k_i'} 2\text{Cr}_{\text{Cr}} + 3V_o'' + 6e'$

The reactions as mentioned above will be applied with Eyring's theory, assuming the activities of atoms on their normal lattice equal to unity, the

activity of defects equal to their molar fraction, and electroneutrality condition, the kinetic calculation of reaction in table 2.1 will be obtained as shown in Table 2.2.

Table 2.2: Kinetic calculation of elementary interfacial steps according to the nature of the predominant defects presents in the Cr_2O_3 lattice.

Cr_2O_3 p-type semi-conductor		
Defect	External elementary step	Internal elementary step
V_{Cr}'''	$\frac{dn_e}{dt} = k'_e \theta^3 - 3^6 k''_e [V_{Cr}''']^8 (1-\theta)^3$	$\frac{dn_i}{dt} = 3^6 k'_i [V_{Cr}''']^8 - k''_i$
O_i''	$\frac{dn_e}{dt} = k'_e \theta^3 - 2^6 k''_e [O_i'']^9 (1-\theta)^3$	$\frac{dn_i}{dt} = 2^6 k'_i [O_i'']^9 - k''_i$
Cr_2O_3 n-type semi-conductor		
Defect	External elementary step	Internal elementary step
$Cr_i^{\bullet\bullet\bullet}$	$\frac{dn_e}{dt} = 3^6 k'_e \theta^3 [Cr_i^{\bullet\bullet\bullet}]^8 - k''_e (1-\theta)^3$	$\frac{dn_i}{dt} = k'_i - 3^6 k''_i [Cr_i^{\bullet\bullet\bullet}]^8$
$V_o^{\bullet\bullet}$	$\frac{dn_e}{dt} = 2^6 k'_e \theta^3 [V_o^{\bullet\bullet}]^9 - k''_e (1-\theta)^3$	$\frac{dn_i}{dt} = k'_i - 2^6 k''_i [V_o^{\bullet\bullet}]^9$

c) Diffusional processes

Due to the difference between ionic and electronic point defect mobilities, a volumetric distribution of charge can appear within the growing scale. The distribution of this charge can accelerate the positively charged ionic defects and impede the negatively charged electronic defects for the diffusion of defects from the internal interface toward the external one but the manner is contrary for the opposite direction. Hence, the electrical potential gradient through the scale will be taken into account in the general diffusion-migration equation as follows.

For ionic defects with degree of ionisation z in x direction

$$J_z = -D_\delta \left[\frac{\partial C_\delta}{\partial x} \pm \frac{zF}{RT} C_\delta \frac{\partial \phi}{\partial x} \right] \quad (2.55)$$

For electronic defects ε in x direction

$$J_\varepsilon = -D_\varepsilon \left[\frac{\partial C_\varepsilon}{\partial x} \pm \frac{F}{RT} C_\varepsilon \frac{\partial \phi}{\partial x} \right] \quad (2.56)$$

where C_δ and C_ε are, respectively, the volume concentration of ionic and electronic defects. D_δ and D_ε are, consequently, the diffusion coefficient of ionic and electronic defects. F is the Faraday constant and ϕ is the electric potential.

2.2.2 High temperature corrosion in carbon-containing gases

In the case of atmosphere containing both carbon and oxygen, for example biogas, the reaction products may either be oxide or carbide. In this study, high temperature corrosion can be associated with the mixture of two or three possible processes: oxidation, decarburization and carburization. However, for ferritic stainless steel, the decarburization is impossible due the lower content of carbon. The literature reviews can be divided into following categories:

2.2.2.1 Physico-chemical characterization in CO₂ or CO atmospheres

a) Oxidation kinetics

The literatures show a few papers only devoted to oxidation kinetics of steels exposed to CO₂ but the behaviour of ferritic stainless steels subjected to pure CO₂ atmosphere is not extensively well-known.

Lee et al. (Lee, 2005) studied the high temperature oxidation of three kinds of hot rolled steel viz. high strength steel (Fe-0.004C-0.6Mn-0.06Ti), bake hardened steel (Fe-0.003C-0.5Mn) and low carbon steel (Fe-0.04C-0.3Mn) under CO₂-O₂ atmosphere at 1100 – 1250°C. They then found that the oxidation process

followed an initial linear rate law which was gradually transformed to a nearly parabolic rate law with the thick porous and non adherent iron oxide scale.

Linear rate law was classically observed in the condition where a surface or phase boundary process or reaction may be the rate determining, for example, oxidation of C40E steel (Fe-0.4C) under CO₂ at 1183-1283 K by Vallette et al. (Vallette, 2005). Their results showed that kinetics followed a linear rate law where the reaction was governed by external (Fe_{1-x}O/CO₂) or internal (substrate/Fe_{1-x}O) interface reaction. The reaction rate was limited by the dissociation of carbon dioxide in to carbon monoxide with oxygen ion adsorption according to reaction (2.57):



Followed by incorporation of chemisorbed oxygen into wustite as



The oxidation of Fe-15Cr alloy in CO₂-CO mixtures at 700-900°C was investigated by Fujii et al. (Fujii, 1967). They proposed that the diffusion of iron through the oxide is sufficiently rapid to preclude the observation of parabolic oxidation rate and an adequate flux of iron to the gas-oxide interface is maintained in spite of the extensive voids separating the outer from the inner layer.

The oxidation of stainless steel 304L (18Cr-8Ni-1.3Mn-0.02C) in carbon dioxide at 1193-1293 K was studied by Goutier et al. (Goutier, 2010). They showed that the kinetics are irregular with three stages: 1) a short initial period of acceleration due to the formation of thin chromia at inner grain boundary and the formation of wustite 2) the slowing down of parabolic kinetics corresponding to a mechanism governed by diffusion of iron vacancies through chromite and finally 3) re-acceleration related to breakaway of protective layer.

In the case of high C metals or steels, decarburization was observed due to the oxidation of the dissolved carbon by CO₂, leading to CO evolution. This phenomenon resulted in weight loss in the first instants of reaction (Billings, 1970; Reeves, 1970).

As well as the study of oxidation kinetics of iron carbon by Billing et al. (Billings, 1970), when iron-carbon (Fe-1.07C) alloys were exposed in CO₂-CO at 950°C, not only the weight change curves were approximately linear

during the initial and final stage of exposure, but the decarburization-oxidation process also occurred. The slope of the curves initially exhibited negative value due to weight losses from decarburization process, which was controlled by the rate of carbon diffusion in both the metal and scale when the oxidizing potential was insufficient for wustite formation. However, the ultimate curves exhibited positive slope due to wustite formation based on surface controlled reaction steps.

In addition, Reeves et al. (Reeves, 1970) investigated the decarburization kinetics for Fe-0.81C in the presence of a wustite scale exposed to CO₂ atmosphere at 950°C. Their results showed that the initial slope was positive giving way to a region of constant slope and finally a region of decreasing slope as the reaction tended to become partially governed by diffusion processes. When shutting off CO₂ supply and allowing a scale specimen to react under vacuum, the loss of carbon became continuously slower with increasing exposure time. Moreover, the rate of carbon loss decreased as the oxide thickness increased. At sufficient thickness (~10 μm), the decarburization was not observed.

In the other hands, carburization was noticed during exposure of Fe-Cr alloys (15% max of Cr) to dry CO₂ at 700-900°C by Fujii et al. (Fujii, 1967). These authors showed that the rate of carbon accumulation in the alloy was closely identical to the oxidation rate since the generation of CO was directly related to the oxidation rate. The adsorbed CO on the surface led to CO disproportionation or reduction of CO which were suggested as carburizing processes. It was reasonable that the possibility of CO disproportionation reaction was enhanced by a sufficient local accumulation of CO so that, kinetically, the reaction can occur.

Moosa et al. (Moosa, 2007) showed that the kinetics of cyclic oxidation in CO₂ at 800-1000°C for uncoated Inconel 600 and coated with Yttrium doped Cr-modified aluminide (CrAlY) were parabolic with a duplex scale consisting of Cr₂O₃ and carbide M₇C₃. The breakdown of the protective scale in mixed oxidants (O/C) was clearly seen at high temperatures (900-1000°C), where chromium oxide was converted into unprotective carbides, with large voids or holes which were also obtained.

b) Scale characterization

It was not broadly reported the characteristics of the oxide scale grown on ferritic stainless steels in CO₂ atmosphere in contrast to that found in air or oxygen. However, The major oxide scale phase on conventional stainless steels in air or oxygen is generally chromia Cr₂O₃, with the spinel phase MnCr₂O₄ as external layer, depending on the alloying elements due to the increasing of diffusion coefficient in order of $D_{Mn} > D_{Fe} > D_{Cr}$ in chromia scale (Antoni, 2004; Brylewski, 2001; Chandra-ambhorn, 2006; Fergus, 2005; Kurokawa, 2004).

The existence of the same oxide phase on stainless steels subjected to CO₂ can be possible whenever the effective partial pressure of oxygen is identical to the decomposition of Cr₂O₃ or other at equilibrium.

In addition, a few authors (Chandra-ambhorn, 2006; Kurokawa, 2004;) have reported the morphology of oxide of stainless steels subjected to low partial pressure of oxygen, for example H₂/H₂O, tends to form the whisker oxide on the top of the chromia scale.

Nevertheless, although pure carbon or graphite can not be thermodynamically formed in CO₂ atmosphere but the precipitation of carbide or carbon can be appeared near the metal-scale interface. The elucidation of this phenomenon has not been reported. However, some assumptions of mechanism can be summarized as follows 1) the accumulation of C by the diffusion of CO₂ or local CO through the scale or microcracks towards the alloy/scale interface and then carbon dissolves in the alloy eventually forming discrete chromium carbides precipitates (Fujii, 1967; Moosa, 2007). Or/and 2) CO release at the oxide-gas interface, resulting from the oxidation reaction, may locally increase this activity making possible chromium carbide formation. It is also envisaged that CO may also diffuse in molecular form through specific channels in the oxide (Abellan, 2009; Abellan, 2010; Rouillard, 2007; Rouillard, 2009)

2.2.2.1 Physico-chemical characterization in carburization atmospheres

Although research work on corrosion of ferritic stainless steels in such biogas atmospheres has been quite rare, various atmospheres such as CO/CO₂ mixtures can be both oxidising and carburising for chromia-forming stainless steels. Such corrosion has been studied by several researchers.

Ferritic stainless steels nominally containing 16-18%wt.Cr were reacted at 750°C for up to 1000h in N₂/H₂/CO/CO₂/CH₄ by Jian et al (Jian, 2003). These authors showed that carbide was present in the corrosion scale as Cr-rich carbide which was indexed by TEM as M₂₃C₆ (M: Cr,Fe,V or M: Cr,Fe). However, the oxide layer formed on the surface of the steel appeared to act as a barrier to carbon diffusion to the steel. They proposed that chromium was consumed in carbide formation, reducing the amount available for corrosion or oxidation protection and the formation of large carbides along the ferrite grain boundaries can embrittle the steel.

Zhang et al. (Zhang, 2008) investigated thermal cycling oxidation of 304 stainless steels (19Cr9Ni) in CO/CO₂ at 700°C and in CO/H₂/H₂O at 680°C. Their results in CO/CO₂ showed that the weight changes represented both weight gain due to carbon and oxygen uptake and weight loss due to spallation or alloy surface disintegration. Surface analysis revealed the presence of chromia, Mn-spinel and small amounts of Cr₇C₃ and Fe₃C. Internal carburization formed fine intergranular carbide at subsurface. In other atmospheres, carbon was also formed to deposit on the surface. After 50 cycles of reaction, chromia, and Mn-spinel were detected in addition to graphite. After 141 cycles, oxide precipitates had formed a distinct layer at the subsurface. This layer appeared to be continuous, but subject to local damage. Fine intergranular and intragranular carbides were also revealed in the steel.

The corrosion of cast alloy (33Ni26CrNbSi) exposed to CO + 4.3%CO₂ gas mixture at temperatures of 982 and 1080°C was studied by Xu et al. (Xu, 2008). Their results showed that MnCr₂O₄ spinel and Cr₂O₃ were the external corrosion products on all samples. Scale thickness increased with time at 982°C

according to approximately parabolic kinetics, however, the scaling kinetics were subparabolic at 1080°C. Growth of the chromium-rich external scale was accompanied by depletion of Cr and disappearance of secondary carbides within subsurface region. Internal oxides like an interdendritic structure mainly contained Cr₂O₃ and silicon rich oxide. In addition to internal oxidation, subsurface carbide dissolution and internal carburization were evident. It is known that, ideally, oxide scales are impermeable to carbon and that Cr-containing alloys are protected against carburization; in this work, the chromium-rich oxide scales did not provide effective barriers to carbon ingress from CO/CO₂ gas.

The major catastrophe in carburization process is usually concerned with metal dusting which attacks iron, low and high alloyed steels and Co- or Ni-base alloys in strongly carburizing gas atmospheres at $a_c > 1$ in the temperature range 400 to 1000°C (Schnider, 2000).

Yin (Yin, 2004) investigated cyclic and isothermal carburization of Incoloy 800HT in CH₄/H₂ (O₂ impurity < 100 ppm) for 500h at 800-1100°C. The kinetic behaviour showed that the weight gain values obtained at the lower temperatures and volumetric ratios of CH₄/H₂ were lower than those obtained at higher value of these parameters. Kinetic curves at 1000°C and 1100°C in 10%CH₄/H₂ with $a_c > 1$, did not experience abrupt weight increase usually encountered in metal dusting failures. It was found that the low weight gains of Incoloy 800HT at 800°C and 900°C was the result of good protection by an external continuous layer consisting of Cr carbides and oxides. Poor protection, however, by semi-continuous or discontinuous outer layer was observed at higher temperatures. Higher ratio of CH₄ in H₂ also enhanced carbon and/or oxygen pickup.

Similarly, carburization of 310 austenitic stainless steel (Fe25CrMn) exposed to 2%CH₄/H₂ at 800-1100°C was studied by Yin (Yin, 2005). It was found that Cr is reactive with carbon but not with oxygen while Ni was reactive with neither carbon nor oxygen in these conditions. The kinetic behaviour showed that increasing temperature led to greater weight gains except at 1100°C due to spallation. In addition, good protection offered by the external continuous layer of (Cr,Mn)-oxides and (Cr-Fe)-carbide was observed at 800 and 900°C. Contrarily, poor

protection by semi-continuous or discontinuous of (Cr/Fe)-carbides was observed at higher temperatures.

The study of cyclic carburization of Haynes 556 in CH₄/H₂ (O₂ impurity < 100 ppm) at 800-1100°C up to 500h was reported by Allam et al (Allam, 2007). The kinetic behaviour of Haynes 556 indicated that the weight gain depended on temperature and was the combine sum of carbon and oxygen uptake. Scale morphology showed that some oxide such as Cr₂O₃, Al₂O₃ and SiO₂ formed thin well-adhering surface layer and contributed to the formation of a diffusion barrier for the inward carbon transport at 800 and 900°C. In the other hand, no continuous diffusion barrier layer could form at 1000 and 1100°C due to the instability of Cr₂O₃, with presence of carbon though the more stable Al₂O₃ and SiO₂ remain stable at this temperature.

A cast HP ModNb alloy (Fe-25Cr-35Ni-1Nb) was oxidised and carburised in CO-CO₂ at 1080°C by Oquab et al (Oquab, 2010). It was found that the external scale consisted of an outer layer of MnCr₂O₄ and a thicker, inner layer of Cr₂O₃. Internal oxidation was observed within the affected subsurface region, and internal carburization with fine precipitates of Cr₇C₃ deeper within the alloy. However, the internal carburization zone beneath an internal oxidation zone resulted from the rapid diffusion of carbon, combined with the fact that carbides were less stable than oxides.

Chapter III

Experimental methods

3.1 Materials

3.1.1 Stainless steels

Sheets of AISI 441 stainless steels were supplied by ArcelorMittal with thickness of 1 mm, whereas sheets of Crofer 22 APU used as reference material were supplied by ThyssenKrupp VDM, with thickness of 0.5 mm. Their chemical composition is shown in Table 3.1. According to Table 3.1, the content of Cr in AISI441 is about 18%, whereas the content of Cr in Crofer22 is 20 – 24 %wt. There are also different minor elements containing in both grades. The minor element of Crofer22 is La while the minor elements of Nb and Mo are added in grade of AISI 441 in contents of 0.49 and 0.01 %wt, respectively. In this report, these steels will be called 441 and Crofer consequently.

Table 3.1: Chemical composition of the stainless steels studied as interconnect materials (%wt)

Grade	Cr	Ni	C	Mn	Si	Al	Ti	Nb	Mo	others
AISI441 (Chemical analysis)	17.76	0.13	0.01	0.28	0.61	0.006	0.16	0.49	0.01	-
Crofer22APU (From supplier)	20-24	*na.	0.03max	0.3-0.8	0.5max	0.5max	0.03-0.2	-	-	La

*na. not analysed

3.1.2 Experimental gas supply

The stainless steels were exposed to various atmospheres as follows: pure carbon dioxide (CO₂), pure methane (CH₄) and mixtures of CO₂ and CH₄. Inert gas, argon, was also applied as flushing gas in the reactors before oxidation or used as a diluting component. In this study 99.995% pure compounds were supplied by Alphagaz Company, France. The impurity gas containing at 25°C are shown in Table 3.2.

Table 3.2: Impurity gas containing in supply gas in ppmv

	H ₂ O	O ₂	CO	CO ₂	C _n H _m	N ₂	H ₂	C ₂ H ₆
Ar	<3	<2	-	-	<0.5	-	-	-
CO ₂	7	10	2	-	5	25	1	-
CH ₄	5	5	-	1	5	15	1	15

3.2 Thermodynamic Calculations

In this study, all experiments will be carried out with 1 atm of synthetic biogas which was composed only of pure methane (CH₄) and carbon dioxide (CO₂). Various volumetric ratios of CH₄ in the synthetic biogas were used: 0% (pure CO₂), 30%, 50%, 70%, and 100% (pure CH₄).

In order to determine all possible species existing in the reactors, the thermodynamic software FactSage 5.5 with data from the Fact53 databank was applied to calculate activity of all species at equilibrium. The activity of species will be presented in terms of partial pressure for gas and activity for solid or liquid in the temperature range of 600 to 1000°C.

In addition, Thermo-Calc version R with TCFE5 database was also used to calculate the activity of elements in 441 with different temperature in order to construct the oxide stability diagram.

3.3 Kinetic Experiments

Kinetics of corrosion can be classified to several types: linear, parabolic, logarithmic or cubic (Sarrazin 2000 et al.). However, the kinetics of corrosion of steels at high temperature is often concerned with parabolic and linear laws. Both can be presented as following

a) Parabolic law

$$\left(\frac{\Delta m}{A}\right)^2 = k_p t \quad (3.1)$$

where $\frac{\Delta m}{A}$ is mass gain ($\text{mg}\cdot\text{cm}^{-2}$)

k_p is parabolic constant in $\text{mg}^2\cdot\text{cm}^{-4}\cdot\text{s}^{-1}$

This law corresponds to a corrosion rate limited by the control of diffusion through the compact scale

b) Linear law

$$\left(\frac{\Delta m}{A}\right) = k_l t \quad (3.2)$$

where k_l is linear constant in $\text{mg}\cdot\text{cm}^{-2}\cdot\text{s}^{-1}$

This rate is controlled by a rate-determining step governed by an interfacial process such as adsorption or reaction at oxide-gas or metal-oxide interface.

In addition, in order to explain the temperature dependence under constant pressure, the rate constant can obey Arrhenius law.

$$k = k_0 \exp\left(-\frac{E_a}{RT}\right) \quad (3.3)$$

where E_a is apparent activation energy of the process ($\text{kJ}\cdot\text{mol}^{-1}$)

The apparent activation energy can be calculated by plotting $\log k$ as a function of $1/T$.

In this study, the kinetics of corrosion of stainless steels were respectively studied: 1) Oxidation kinetics of ferritic stainless steels in CO₂ atmosphere and 2) Kinetics of corrosion of ferritic stainless steels exposed to synthetic biogas.

3.3.1 Oxidation kinetics of ferritic stainless steels in CO₂ atmosphere

3.3.1.1 Materials preparation

Samples were prepared with dimensions 15 x 20 mm². Before oxidation, each face of specimens was polished up to 1200 SiC grit, trimmed all edges and corners in order to protect scale spallation, and finally rinsed in distilled water. Some grease or fat were washed by acetone and they were further cleaned by alcohol in ultrasonic machine, and subsequently dry in air.

In this study, dynamic atmosphere with the linear velocity of gas of 1 mm.s⁻¹ at room temperature was applied for CO₂ oxidation runs.

3.3.1.2 Thermogravimetric monitoring

A continuous measurement of mass change of samples thermobalance was used for oxidation runs. The SETARAM thermobalance version B60 in this study was supplied by PHELMA Laboratory, France. The sensibility of this machine is 0.05 mg. In the first oxidation kinetics, carbon dioxide and argon were applied for oxidation atmospheres in this method.

According to the schema of thermobalance as show in Figure 3.1, a sample was first suspended with silica stem in a silica tube contained in an electrical furnace. It was then necessary to eliminate the gas existing in the tube by vacuum pump. It was evacuated until the total pressure displayed on pressure gauge equal to -1 bar. The actual pressure was in the order of 10⁻³ mbar. After that, CO₂ valve was opened and adjusted the flow rate. CO₂ was then flowed in the tube until the total pressure was equal to 1 bar. Experimental temperature was controlled by a thermocouple type K in the tube. The furnace was then heated to desired temperature with heating rate: 15°C.min⁻¹. After reaction, the regulator was switched off and

sample was furnace-cooled under reacting gas with cooling rate: $2^{\circ}\text{C}\cdot\text{min}^{-1}$. Mass change was recorded when temperature reached to 150°C for various oxidation periods up to 80h.

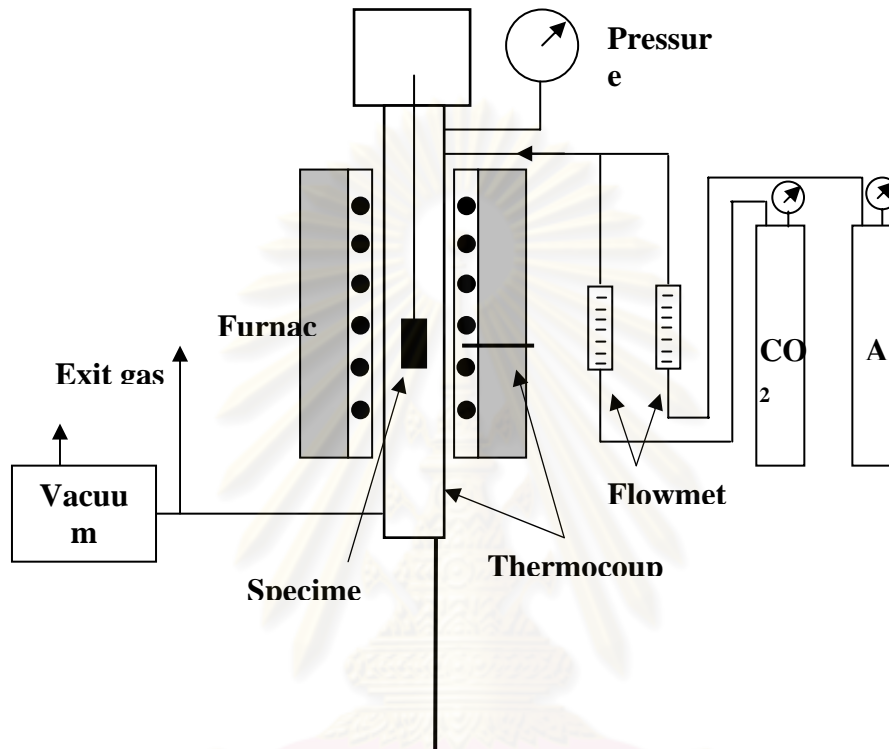


Figure 3.1: Experimental schema of thermobalance used for oxidation runs in CO_2 atmosphere.

Several effects of physical interaction between gas and specimen such as buoyancy, convection currents and thermomolecular fluxes may be concerned.

Thermogravimetric measurement will be significantly disturbed by buoyancy force, assuming ideal gas, with equation following:

$$B = gV \frac{M}{R} \frac{P}{T} \quad (3.4)$$

Where B = Buoyancy force (N)

M = Mean molar mass of gas mixture ($\text{kg}\cdot\text{mol}^{-1}$)

R = Universel gas constant = $8.314 \text{ J}\cdot\text{mol}^{-1}\cdot\text{K}^{-1}$

g = gravitational constant = $9.81 \text{ m}\cdot\text{s}^{-2}$

V = volume of solid immersed (m^3)

P = pressure (N.m^{-2})

T = Temperature (K)

In the case of CO_2 atmosphere, for $M = 44 \text{ g mol}^{-1}$, $V = 300 \times 10^{-9} \text{ m}^3$ for 441 and $150 \times 10^{-9} \text{ m}^3$ for Crofer samples respectively, The equation 3.4 become

$$B = 1.56 \times 10^{-8} \frac{P}{T} \quad \text{for 441} \quad (3.5)$$

and

$$B = 7.79 \times 10^{-9} \frac{P}{T} \quad \text{for Crofer} \quad (3.6)$$

According to equation (3.5) and (3.6), the pressure and temperature of gas play an important role to the buoyancy force. The variation of mass change will be theoretically about 0.1 mg at temperature between 800-1000°C and pressure at 1 atm.

The apparent mass of sample on thermogravimetric monitor will be equal to the difference of real mass of sample and its buoyancy.

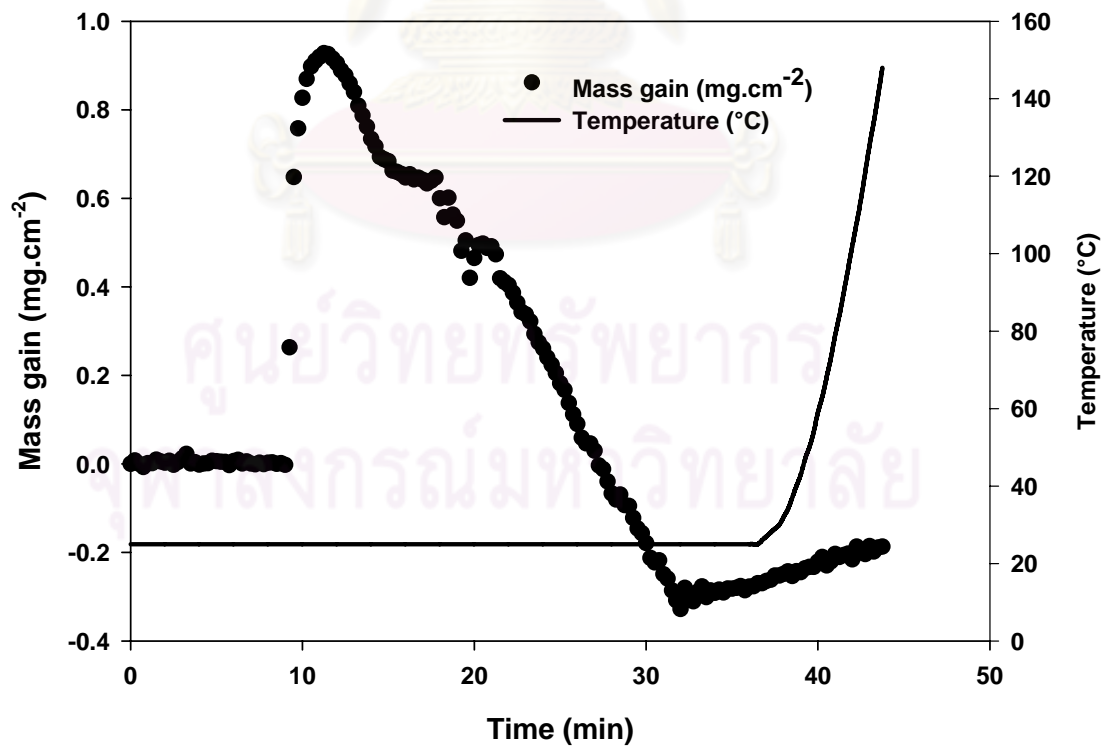


Figure 3.2: Pre-record of mass gain of 441 by thermobalance in the oxidation experiment.

The mass change in pre-record stage is revealed as shown in Figure 3.2. The initial stage showed apparently the mass gain increases rapidly in a few minute due to the decrement of buoyancy force by decreasing air pressure during vacuum pumping. The mass gain then decreased slightly in 15 minute because of the increasing of CO₂ pressure in the tube until the pressure equal to 1 bar. While the pressure was constant, the mass gain behaved constant at less than zero because the molecular weight of CO₂ was greater than that of air. The mass gain then increased a little when the temperature in the tube increased.

The mass gain of 441 in CO₂ was continuously registered at 150°C till to 80 h. the buoyancy force is presented as shown, for example, in figure 3.3 at 800°C and when the temperature reach to room temperature. The buoyancy force for steel with surface area of 6.70 cm² at 1000°C was closely equal to 0.18 mg cm⁻² or 1.2 x 10⁻⁵ N. By equation 3.5, the calculated buoyancy force is 1.7 x 10⁻⁵ N. The experiment and theoretical buoyancy are different about 30% due to the deviation of gas behaviour from ideality.

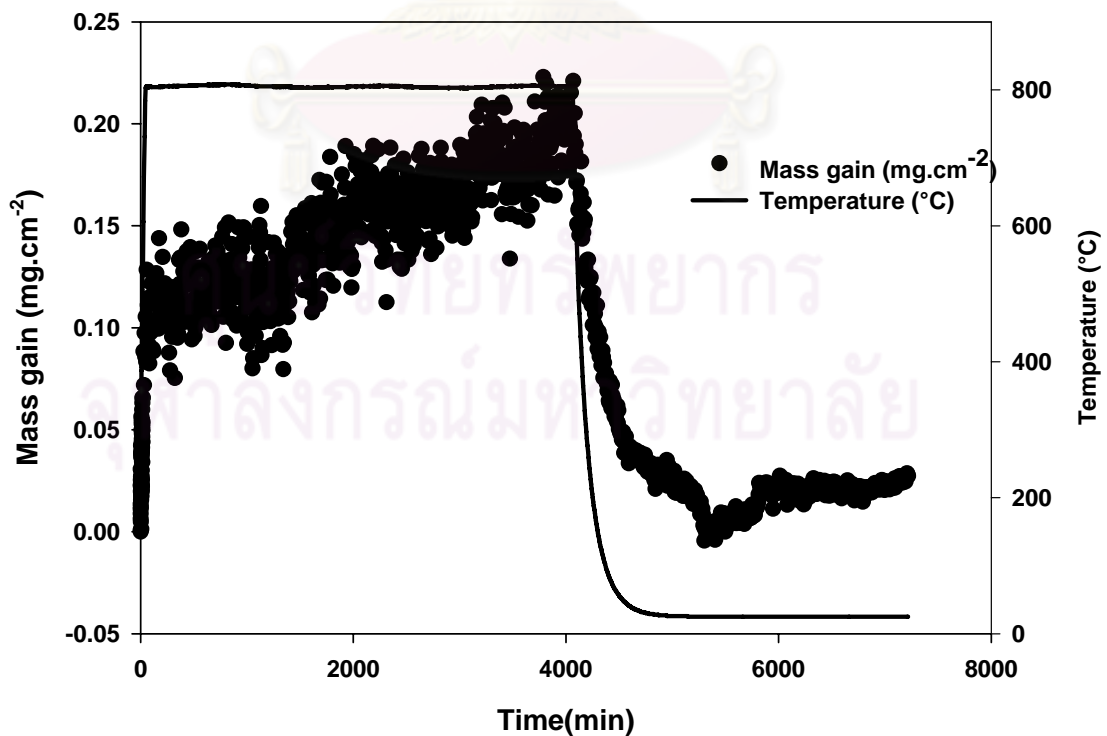


Figure 3.3: Decrease of buoyancy forces of 441 in thermobalance between 800°C and room temperature.

As seen in the figure 3.2 and 3.3, when the temperature and pressure were constant, the effect of convection led to a little variation around equilibrium position of sample (0.05 mg.cm^{-2}). The Knudsen forces by thermomolecular effect will also lead to very small mass change in the experiment because of high gas pressure in the thermobalance ($> 100 \text{ mbar}$). Therefore, these effects can be neglected in this study.

For oxidation kinetics of CO_2 , the necessary kinetics were studied as follows

a) Isothermal kinetics of oxidation

The kinetic oxidations of 441 and Crofer were carried out in the constant pressure equal to 1 bar of pure CO_2 in period up to 80h for the temperature range between 800 and 1000°C. The mass gain was then plotted with exposure time, and rate constants were also plotted versus temperature for determining the apparent activation energy.

b) Isobaric kinetics

The influence of the partial pressure of CO_2 on the oxidation kinetics of 441 was studied at constant temperature (800°C). The partial pressure of CO_2 was controlled by mixing CO_2 and Ar using different flow rates of CO_2 in the same total flow rate. The total pressure in the thermobalance tube was still equal to 1 bar. The partial pressure of CO_2 in this study was considered as 100, 200, 400, 600, 800 and 1000 mbar. The rate constants were then plotted with partial pressure of CO_2 in order to understand the mechanism of oxidation kinetics depending on the different partial pressures of CO_2

3.3.2 Kinetics of corrosion of ferritic stainless steels exposed to synthetic biogas

3.3.2.1 Materials preparation

Samples were prepared with dimensions 10 x 20 mm² for discontinuous measurement and 10 x 15 mm² for thermogravimetric monitoring. Before oxidation, all faces of specimens were polished up to 1200 SiC grit, trimmed all edges and corners in order to protect from scale spallation during oxidation, and finally rinsed in distilled water. Possible grease or fat was washed by acetone and the samples were further cleaned by alcohol in ultrasonic machine, and subsequently dry in air.

In this study, dynamic atmospheres of synthetic biogas, composed of CH₄ and CO₂, were also applied with the linear velocities given of gas at 1 mm.s⁻¹ for discontinuous record and 0.5 mm.s⁻¹ for thermogravimetric runs at room temperature.

3.3.2.2 Isothermal corrosion in horizontal furnace

The first physico-chemical characterizations of ferritic stainless steels subjected to synthetic biogas at temperature range of 700-900°C was carried out by discontinuous measurements in horizontal furnace for oxidation periods of 2, 25, and 80 hours.

The schematic diagram of the horizontal furnace is presented in Figure 3.4. The samples were primarily placed in the isothermal zone of the reactor. The distribution of temperature in the function of distance (zero-set at the middle of reactor) was measured and is revealed in Figure 3.5. It was noted that the isothermal zone was in range of ± 5 cm from the middle of the tube making possible to use several specimens (in this study, at most 4 specimens) in the same runs.

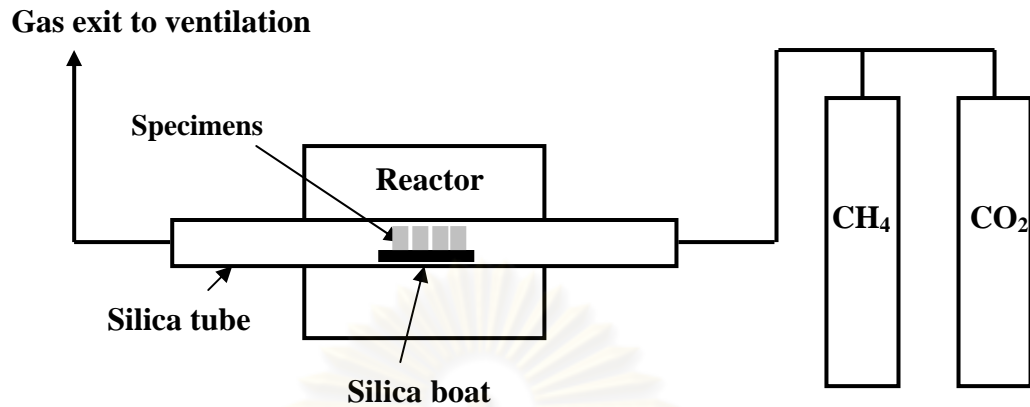


Figure 3.4: Schema of horizontal furnace used for oxidation of steels in synthetic biogas.

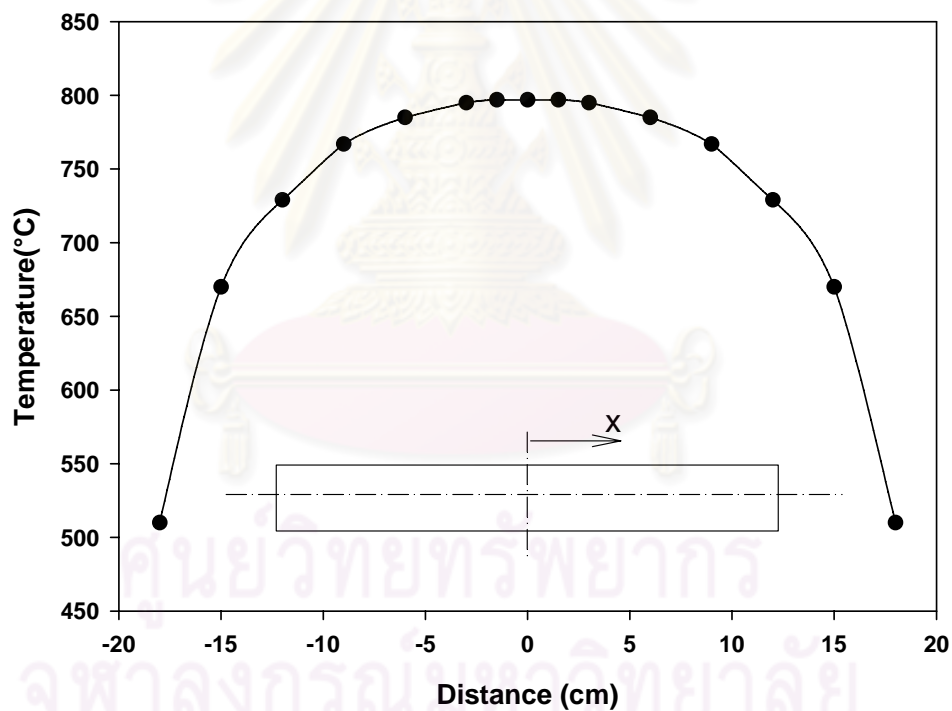


Figure 3.5: Distribution of temperature in function of distance in the horizontal furnace

Carbon dioxide was flowed as purging gas for 60 min. The chosen mixture of methane and carbon dioxide with a total pressure equal to 1 bar was then flowed into the reactor at room temperature for 60 min with a linear flow rate of $1 \text{ mm}\cdot\text{s}^{-1}$.

The furnace was then switched on. The temperature increase in function of time is shown in Figure 3.6. It was found that the temperature increased dramatically from start in 30 minutes and the temperature then increased to the desired temperature in 1 hour. After the desired time, the furnace was switched off and the temperature reach to room temperature in 500 min.

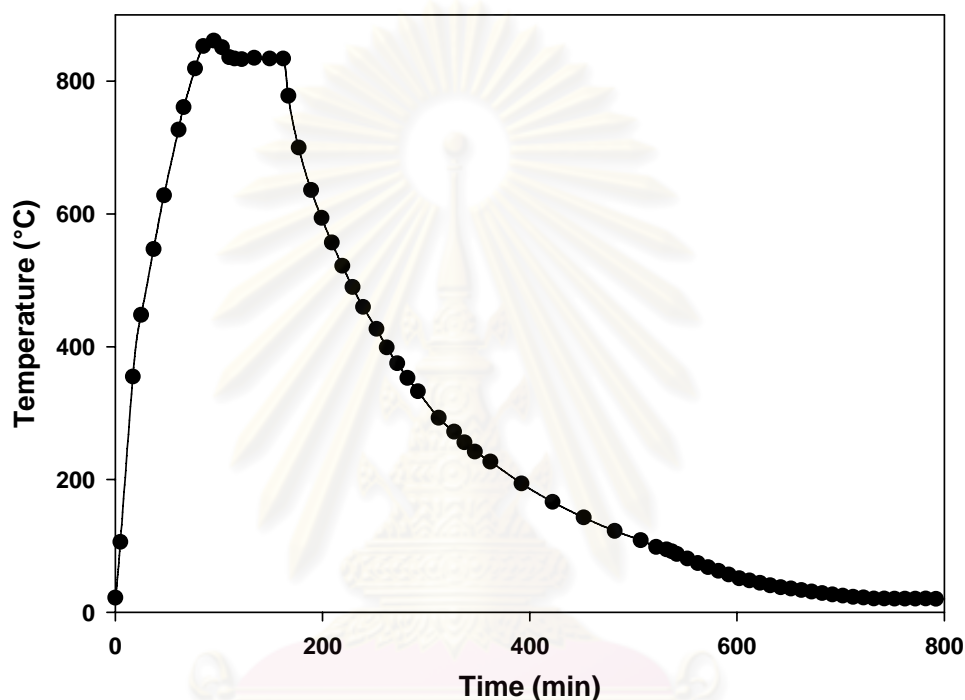


Figure 3.6: Temperature evolutions in function of time in the horizontal furnace

In these conditions, the precision on the duration of the reaction, supposed to occur in the 80% to 100% range of the operating temperature was ~ 20 min. Various volumetric ratios of CH_4 in the synthetic biogas were used: 0% (pure CO_2), 30%, 50%, 70%, and 100% (pure CH_4). Mass change of the samples was determined, without any cleaning procedure after the reaction, with an accuracy of $\pm 10 \mu\text{g}$.

3.3.2.3 Thermogravimetric experiments

A continuous record of mass change of samples using a thermobalance was used for oxidation runs. The SETARAM microthermobalance version B24 in this

study was also supplied by SIMaP Laboratory, France. The mass change was measured with sensibility of $0.5 \mu\text{g}$.

Pure carbon dioxide was used as protecting gas for the thermobalance electronic device and also flushing atmosphere. The methane was then applied and mixed with CO_2 below the balance head before the reaction. The synthetic biogas was flowed with a linear velocity of $0.5 \text{ mm}\cdot\text{s}^{-1}$ till 1 hour in order to assure that there was only synthetic biogas in the tube. The various volumetric ratios of CH_4 in synthetic biogas used in service were 50%, 70%, and 100% (pure methane) for the temperature range of $600\text{-}800^\circ\text{C}$.

Before experiments, an inert sample (silica sheet) with dimension of $12 \times 20 \times 2 \text{ mm}^3$ was used for the study of buoyancy force in this thermobalance in synthetic biogas ($70\%\text{CH}_4 + 30\%\text{CO}_2$) at 800°C . The mass change with time was therefore depicted as shown in Figure 3.7.

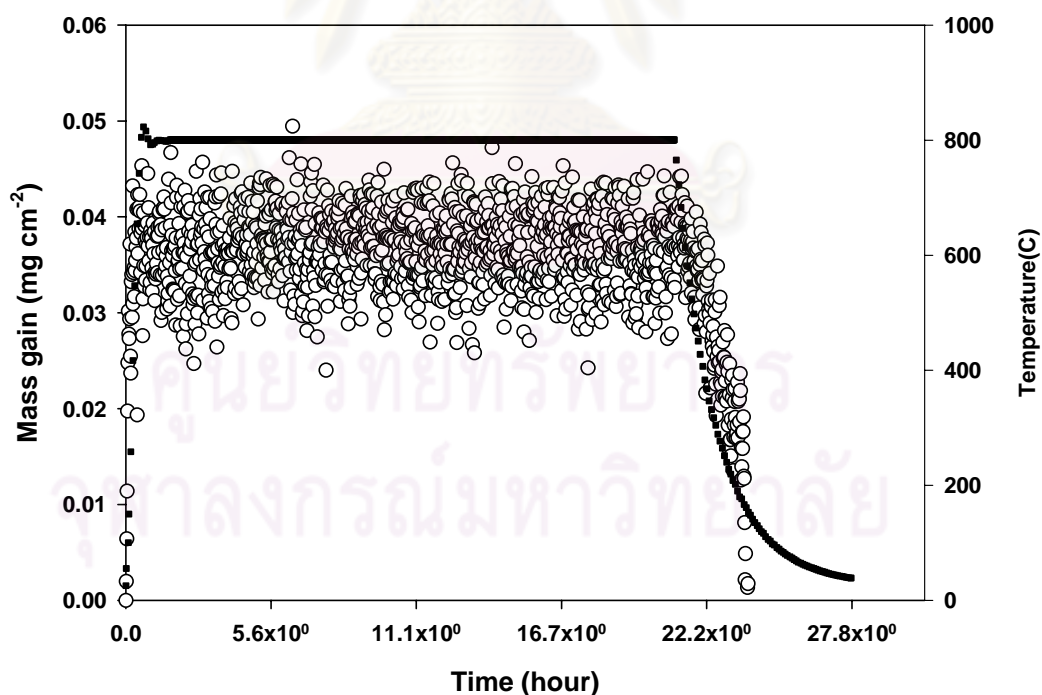


Figure 3.7: Apparent mass changes of silica sample in $70\%\text{CH}_4 + 30\%\text{CO}_2$ at 800°C due to buoyancy effect between room temperature and 800°C .

From Figure 3.7, the result shows that the buoyancy force of silica in this synthetic biogas at 800°C was 0.037 mg.cm^{-2} and variation during constant mass gain was $\pm 3.34 \times 10^{-3} \text{ mg.cm}^{-2}$.

3.4 Corrosion Scale Characterizations

Basic techniques of physico-chemical characterization such as scanning electron microscopy (SEM), Energy Dispersive X-ray spectrometry (EDX) and X-Ray Diffraction (XRD) were used for analysing corrosion scales.

A further experiment, photoelectrochemistry, was operated in this study in order to determine the electronic behaviour of oxide scale. The marker experiment was also employed in order to identify the direction of scale growth. Finally, the microhardness machine was employed for characterizing the carburization of the materials. These techniques will be explained briefly, following (Sarrazin 2000, Verhoeven 1975, Wouters 1996)

3.4.1 Scanning electron microscope and energy dispersion spectrometry

Scanning electron microscope (SEM) operates in similar mechanism as optical microscope. Instead of using light, a very small diameter electron beam is made to scan a square region on the sample surface and then trace out on the cathode-ray tube.

As electrons collide onto the sample surface, they interact with the atoms of the target, exciting electrons from their deep energy levels to a higher level. Secondary electrons are generated in the collision cascade and lose energy traveling to the surface. This energy is influenced by surface topography and these electrons are generally used to obtain image with magnification about 10000x.

In addition, when electrons enter to the sample, X-rays or photons X are also emitted. The wavelength of this energy is directly linked to the nature of element analyzed. Quantitative analysis of chemical composition is possibly performed by a solid state detector. This analysis is well-known as Energy Dispersive X-ray spectrometry (EDX).

LEO 440 SEM equipped with EDX for this study was supplied by CMTC Laboratory, Grenoble INP, France. Before observation, surface of samples oxidized was prepared to become electronically conductive surface by carbon deposition.

For the cross - sectional observation, the favorable methods were used as follows.

a) Fractography of corrosion scale

The sample was immersed and broken in liquid nitrogen. In order to easily break the sample, the sample should be firstly grooved by a diamond saw. However, this method is practically difficult to obtain good observation because all observation plans is possibly not at the same level.

b) Mounted sample

The cross-sectional observation of samples was obtained by polishing in the cross-section view. However, before polishing, samples should be enveloped for protection of corrosion scale during polishing. Firstly, due to the non metallic state of scale, the sample was covered with Au by sputtering method with a few microns in thickness. The electroless Ni coating was then deposited using ATF SYSTEMI 300 solution. The 8% ATF SYSTEMI 300A (aqueous solution containing Ni^{2+}) was mixed with 15% ATF SYSTEMI 300B (aqueous solution containing sodium hypophosphite) in distilled water. The optimized temperature was about 89°C with magnetic or mechanical agitation. Samples were then immersed in the solution prepared for 1 hour for thickness more than $100\ \mu\text{m}$ thick. Finally, samples coated with Ni were cold-mounted in resin.

3.4.2 X-Ray Diffraction

When an X-ray beam is impinged on a metal surface, a number of different and interesting interactions occur. One of these interactions causes the electrons of the

crystal atoms to emit electromagnetic radiation of the same wavelength, λ , as the impinging beam, and this produces a diffraction effect. The effect of diffraction is identical to reflection but, for a certain number of angles (θ) only, defined by Bragg's equation:

$$n\lambda = 2d_{hkl} \sin \theta \quad n = 1, 2, 3... \quad (3.7)$$

with d_{hkl} = planar distance between plan hkl

The identification of the peaks was made by comparison with the data from the ICDD (International Center for Diffraction Data) databank. Such an analysis is mainly qualitative and detects products in percentage amounts; generally, neither trace products nor amorphous phases in any amount, for example, glass, would be detected.

In this study, the conventional X-ray Diffraction Spectroscopy (X-RD) was applied to investigate the types of compounds. Cu-K α was used as the radiation source. The grazing angle X-Ray Diffraction (GAXRD) was also available in the range of 20-80° with speed of 0.1° min⁻¹. This machine was supplied by Phelma engineering school, Grenoble INP, France.

3.4.3 Photoelectrochemistry

Photoelectrochemistry (PEC) experiments were also performed to assess the electronic properties of the semi-conductor materials. When a semi-conductor is illuminated by light energy $h\nu$ at higher than its gap energy, the electrons can be excited from the valence band to conduction band and they will then create electron-hole pairs within or on the surface of materials. When the Fermi level of the semi-conductor is much more than that of the electrolyte, the major carriers are evacuated within the materials by applying potential, whereas the major carriers move toward the surface where they can be transferred to a reduction-oxidation reaction in the electrolyte. The photocurrent, I_{ph} , will be positive for semiconductor type n and negative for type p . The following equation was proposed by Gartner and Butler for an ideal interface semi-conductor/electrolyte (Gartner, 1959, Butler, 1977)

$$I_{ph} = e \cdot \Phi_0 \cdot \left(1 - \frac{\exp(-\alpha_\lambda \cdot W)}{1 + \alpha_\lambda \cdot L} \right) \quad (3.8)$$

where e is electron charge

Φ_0 is the flux of incident photon

α_λ is adsorption coefficient of light for wavelength λ

L is the diffusion distance of minor electronic carriers

W is the depth of charge region which

$$W = \frac{2 \cdot \varepsilon \cdot \varepsilon_0}{N} \cdot \sqrt{V - V_{pb}} \quad (3.9)$$

where ε is the dielectric constant of the semi-conductor

ε_0 is the dielectric constant of vacuum

N is the concentration of major carrier

If the penetration depth of light, α_λ^{-1} is very large, equation (3.9) become

$$I_{ph} = e \cdot \Phi_0 \cdot \alpha_\lambda \cdot W \quad (3.10)$$

PEC is a non-destructive ex-situ technique for measuring and predicting electrical currents generated by illuminating a semi-conductor in an electrolytic solution of 0.1M Na₂SO₄ with pH = 10. To identify the oxide phase, the applied potential was fixed at 500 mV. Photocurrent was then recorded and transformed in function of light energy. To determine the semi-conductor type of oxide scale, light energy was used at several energy gap of oxide. Photocurrent was also recorded in function of applied potential (-1500 to 500 mV). The photoelectrochemical set-up was entirely built at SIMaP laboratory, France.

3.4.4 Marker experiments

This experiment is based on the observation, after oxidation, of the location of inert markers deposited on the metal surface before oxidation. If the markers are located at the metal-scale interface, then the matter transport in the scale is the external growth by cationic transport. Contrarily, if the markers are located at the

scale-gas interface, the matter transport is the internal growth by anionic transport. It is possible that the markers may be located at a well-defined intermediate interface, showing that two subscales grow by opposite cationic and anionic transports.

In this study, powder of inert elements such as Pt was deposited on the 441 oxidized in CO₂ atmosphere at 800°C for 544 hours. The observation in the cross-section was carried out by SEM.

3.4.5 Microhardness

The Knoop microhardness test was used in the study of carburization characterization. Knoop indenter is a better choice for hard brittle materials where indentation cracking would be more extensive using the Vicker indenter at the same load. A pyramidal diamond point, with an included longitudinal and transverse angle of 172° 30' and 130° respectively, was pressed into the polished surface of the test material with a 10 g, for 10 s, and the resulting indentation was measured using a microscope. The hardness can be calculated with equation following

$$HK = \frac{14229P}{L^2} \quad (3.11)$$

where P is the applied load (gf)

L is the length of indentation along its long axis (μm)

The Buehler Micromet II microhardness machine was supplied by SIMaP, France.

Chapter IV

Oxidation kinetics of ferritic stainless steels in CO₂ atmosphere at high temperatures

4.1 Introduction

When ferritic stainless steels used as interconnectors in SOFC are exposed to biogas which contains mainly methane and carbon dioxide (Rasi, 2007), the possibly important oxidizing gas is carbon dioxide due to the existence of oxygen atoms in its molecule.

In this mixture, carbon dioxide will lead to steel oxidation whereas methane may induce carburization resulting in embrittlement and loss of oxidation resistance. The stability and formation kinetics of a thin and electrically conductive oxide scale is therefore an important challenge to suppress carburization (Yin, 2004; 2005), a non tolerable phenomenon for the required lifetime of the stacks.

The objective of this chapter is to study the oxidation kinetics of ferritic stainless steel grade 441 with Crofer22APU used as reference under pure CO₂ in order to understand the oxidation mechanism. It will be described in the term of thermodynamics, oxidation kinetics and oxide scale characterization consequently.

4.2 Thermodynamic Calculation

4.2.1 Partial pressure of oxygen

Their relative partial pressures are related by the reaction corresponding to dissociation of CO₂ into O₂ and CO at different temperatures. The activity of oxygen can be determined by the following reaction:



Assuming ideal gas, at equilibrium it is given by

$$a_{O_2} = P_{O_2} = K \left(\frac{P_{CO_2}}{P_{CO}} \right)^2 \quad (4.2)$$

where K is the equilibrium constant for equation (4.2) at temperature T .

The calculations of pressures of O_2 and CO_2 in function of reciprocal temperature are shown in Figure 4.1

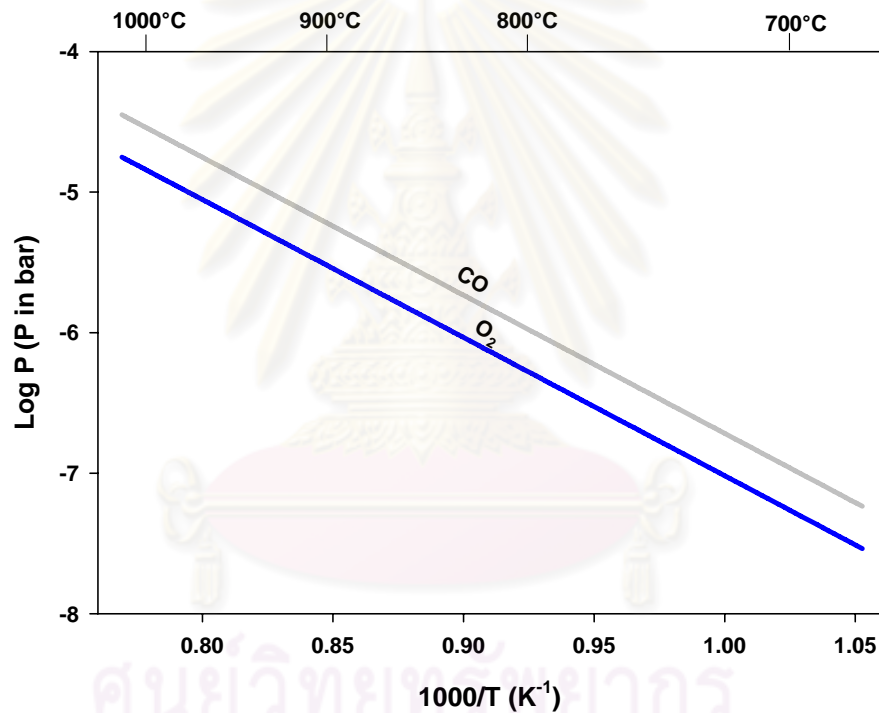


Figure 4.1: The logarithm of partial pressures of O_2 and CO_2 in function of reciprocal temperature.

The calculation showed that the pressure of CO is greater than that of O_2 by factor of 2 at all temperatures and both pressures in logarithmic function increased linearly with increasing temperature. In the range of 600°C to 1000°C , the pressures were in the order of $10^{-8.4}$ to $10^{-4.9}$ bar for O_2 and 10^{-8} to $10^{-4.6}$ bar for CO . The pressure of CO_2 was always fixed to 1 bar in this calculation. In this temperature

range, the carbon activity varied from $10^{-13.9}$ to $10^{-11.5}$, showing that no solid carbon nor stable carbide can be thermodynamically formed.

4.2.2 Oxide stability diagram

The diagram as shown in Figure 4.2 presents that the metallic elements of 441 can be thermodynamically oxidized, when they are subjected to the pure CO_2 atmosphere in which the dissociated pressure of oxygen is greater than that of the metal-oxide equilibrium.

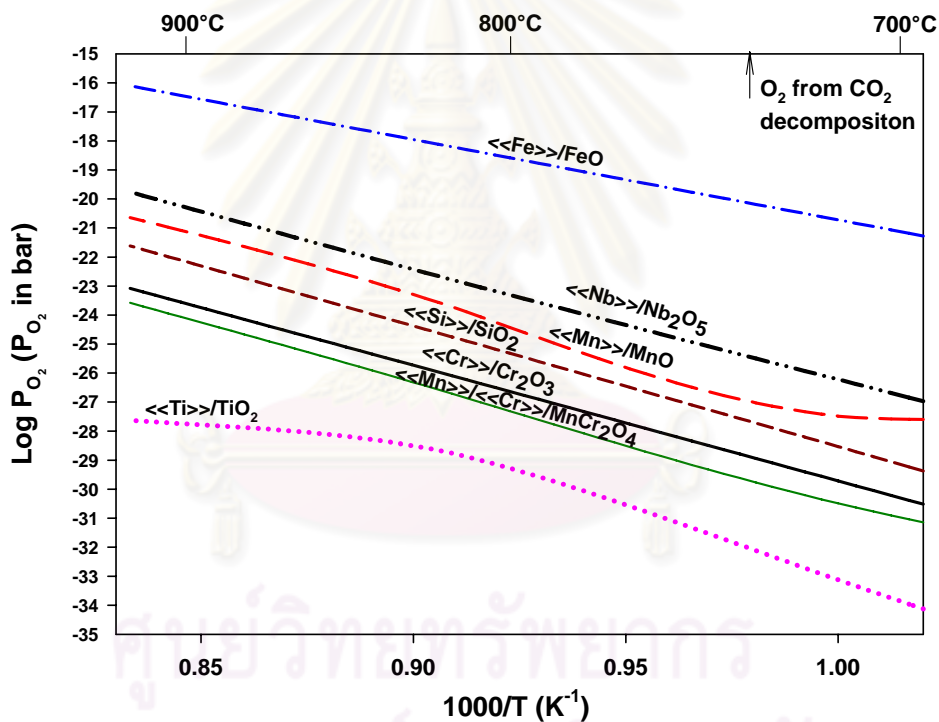


Figure 4.2: Oxide stability diagram plotted as $\text{Log } P_{\text{O}_2}$ in function of reciprocal temperature

To calculate this diagram, the activities of elements Fe, Cr, Mn, Si, Ti, Nb were determined using Thermocalc version R (detailed in Appendix A). The stability diagram shows that all partial pressures of oxygen at the metal-oxide equilibrium in 441 increases with increasing temperature in range of 700 to 900°C. As mentioned above for dissociate partial pressure of O_2 from in CO_2 , these values were

high adequate to make all the elements present in the steel oxidised to binary oxides as FeO, Cr₂O₃, SiO₂, TiO₂, Nb₂O₅. Concerning manganese oxidation, the spinel phase MnCr₂O₄ is the stable phase in contact with the metal. (activity of manganese in 441 equal to 10^{-2.6} at 800°C, as described in Appendix A).

4.3 Oxidation Kinetics

4.3.1 Isothermal oxidation kinetics

a) Oxidation kinetics of 441

Figure 4.3 presents the oxidation kinetics of stainless steel 441 under pure CO₂ at different temperatures.

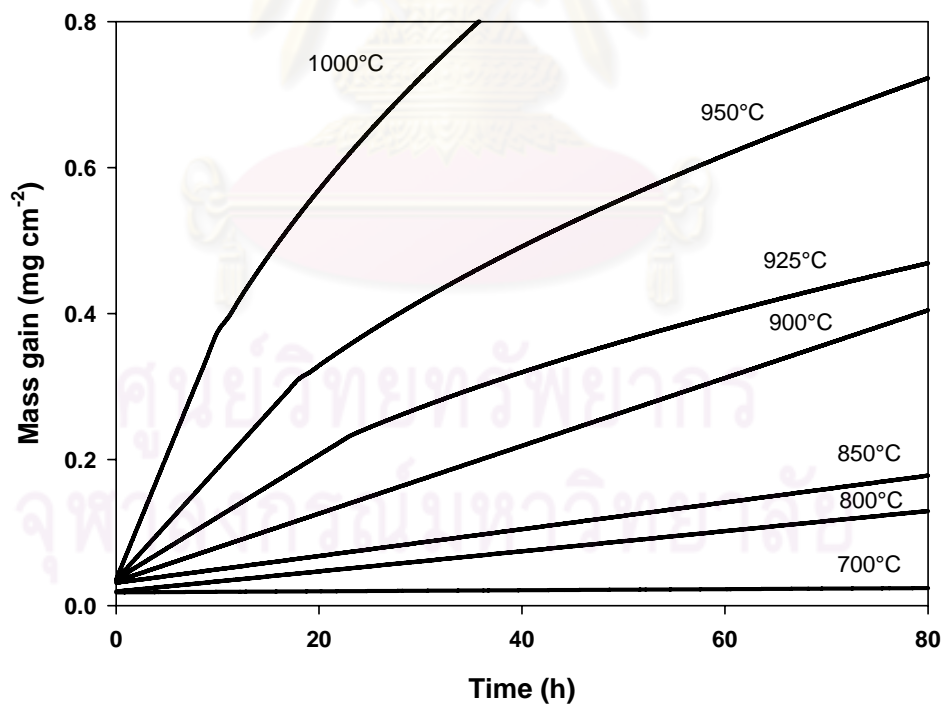


Figure 4.3: Oxidation kinetics of stainless steel 441 under 1 bar pure CO₂ at several temperatures.

According to Figure 4.3, all oxidation kinetics increased when the temperature increased. It was also observed that the mass gain at all temperatures increased very rapidly at the initial stage (20 min) to about 0.03-0.05 mg.cm⁻² due to rapid nucleation of oxide. After this short period, oxidation kinetics was linear during 80h from 700 to 900° C. On the contrary, from 925°C to 1000°C, kinetics was linear in the first step of oxidation, changing to roughly parabolic for longer times. The linear-to-parabolic transition occurred at a mass gain increasing with temperature: 0.25 mg.cm⁻² at 925°C, 0.30 mg.cm⁻² at 950°C and 0.45 mg.cm⁻² at 1000°C.

b) Oxidation kinetics of Crofer

The same experiments were performed with Crofer. The oxidation kinetics of Crofer under pure CO₂ at different temperature is revealed in Figure 4.4.

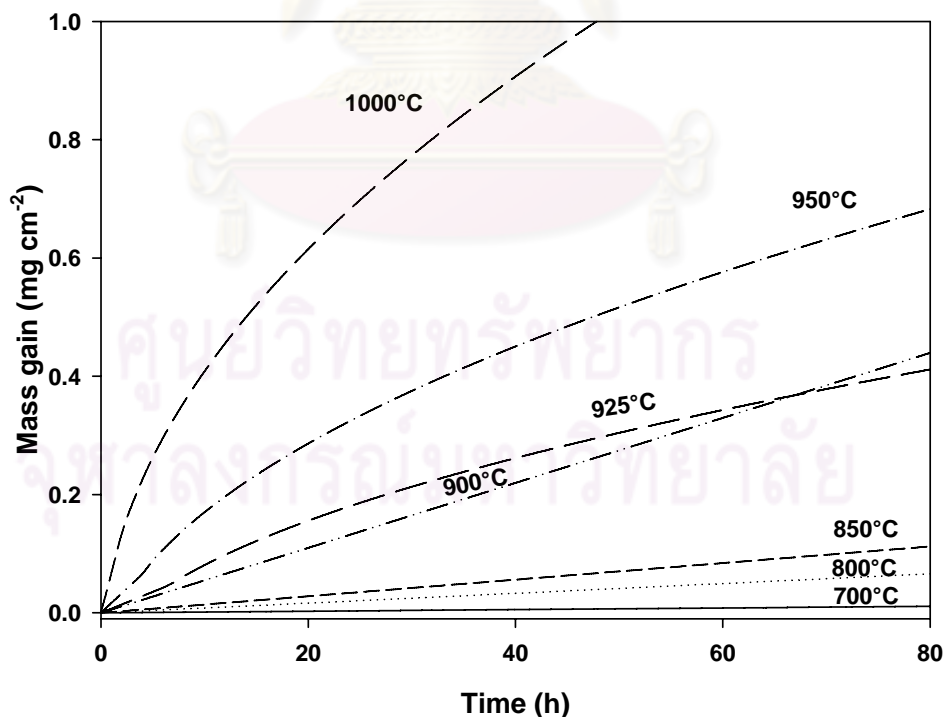


Figure 4.4: Oxidation kinetics of stainless steel Crofer under 1 bar pure CO₂ at several temperatures.

The kinetics of Crofer was shown to be very similar to 441. The kinetics of Crofer was linear at temperatures lower than 925°C. It was, however, found that no mass gain due to rapid nucleation was observed at the initial stage. In the other hand, the kinetics was parabolic at higher temperatures. Comparing the mass change obtained in the same conditions for 441 and Crofer, it was almost identical.

c) Arrhenius plot of temperature dependence

From the data in Figure 4.3 and 4.4, the temperature dependence of oxidation rate at 1 bar CO₂ constant pressure was plotted in Arrhenius coordinates as shown in Figure 4.5 for all linear rate constants and in Figure 4.6 for all parabolic rate constants.

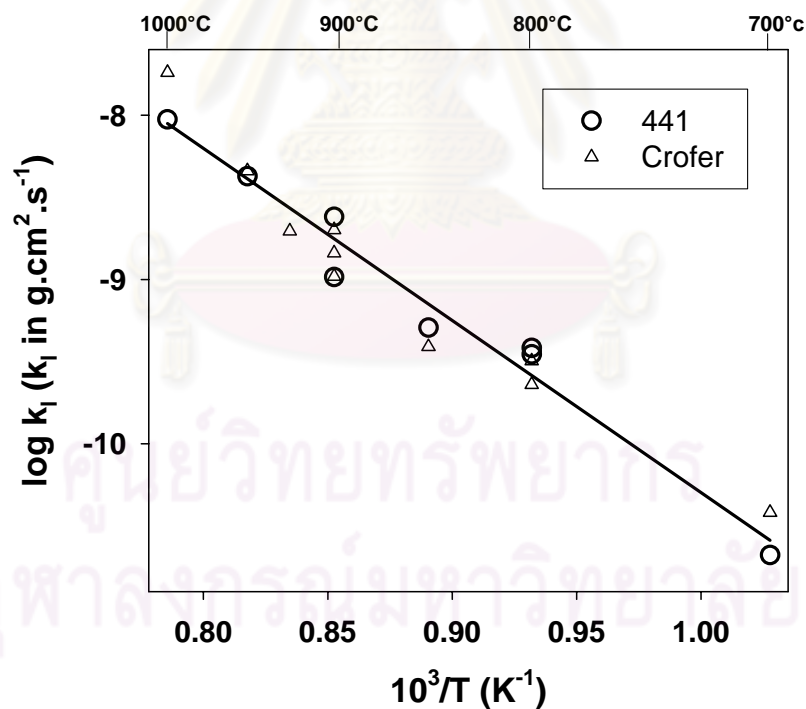


Figure 4.5: Arrhenius plot for the linear rate constants of 441 and Crofer oxidation under 1 bar pure CO₂.

From Figure 4.5, it was observed that the linear constants for 441 and Crofer were almost equal. Arrhenius law seemed to be followed with the

apparent activation energy $200.6 \text{ kJ}\cdot\text{mol}^{-1}$ or 2.07 eV for 441 and $198.5 \text{ kJ}\cdot\text{mol}^{-1}$ or 2.05 eV for Crofer. Comparing to the linear constant of iron oxidised in pure CO_2 by Valette et al. (Valette 2005), the activation energy of iron in CO_2 ($245.15 \text{ kJ}\cdot\text{mol}^{-1}$) was higher than that of 441 and Crofer. The linear constants of 441 and Crofer were also inferior to those of iron in the same conditions as depicted in Table 4.1. However, the linear constant of iron in CO_2 had a tendency to be lower than that of steels at lower temperatures.

Table 4.1: Linear constants of the oxidation (k_l) of some metals at 800°C

Grade	$k_l \text{ (g}\cdot\text{cm}^{-2}\cdot\text{s}^{-1}\text{)}$	References
441	3.50×10^{-10}	The present work
Crofer	2.29×10^{-10}	The present work
C40E steel	1.25×10^{-9}	Extrapolated (Valette, 2005)

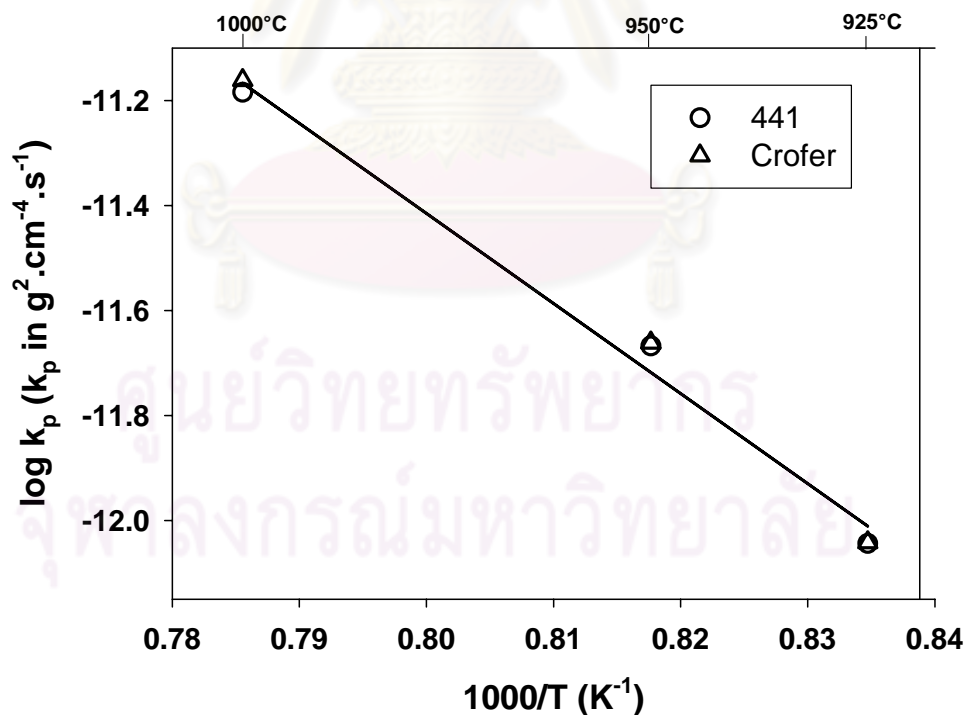


Figure 4.6: Arrhenius plot for the parabolic rate constants of 441 and Crofer oxidation under 1 bar pure CO_2 .

From figure 4.6, it was observed that $k_{p,s}$ for 441 and Crofer oxidation were also near identical. By comparison with literature data, it appeared that they lied in the same range as $k_{p,s}$ for oxidation of 441 in Ar-O₂ or N₂-O₂ (Chandra-ambhorn, 2006; Toscan, 2004). They obey the Arrhenius law with an apparent activation energy of 328.70 and 337.00 kJ.mol⁻¹ or 3.40 and 3.49 eV for 441 and Crofer respectively, significantly higher than the values obtained in synthetic air (Chandra-ambhorn, 2006) and 20%O₂/Ar (Toscan, 2004) (242 kJ and 264 kJ mol⁻¹ respectively).

Nevertheless, comparing parabolic constants of steels oxidized in pure CO₂ by several literature data as shown in Table 4.2, the parabolic constants remained the same range except 304L in CO₂.

Table 4.2: Parabolic constants of the oxidation (k_p) of some steels at 1000°C

Grade	Atmosphere	K_p (g ² . cm ⁻⁴ . s ⁻¹)	References
441	CO ₂	6.54 x 10 ⁻¹²	The present work
441	Synthetic air	3.98 x 10 ⁻¹²	(Chandra-ambhorn 2006)
Fe-18Cr-Ti-Nb	Ar + 20%O ₂	9.38 x 10 ⁻¹²	Interpolated (Toscan 2004)
304L	CO ₂	2.01 x 10 ⁻¹⁰	(Goutier 2010)
Inconel 600	CO ₂	8.91 x 10 ⁻¹³	(Moosa 2007)
Crofer	CO ₂	6.90 x 10 ⁻¹²	The present work

4.3.2 Isobaric oxidation kinetics of 441

The influence of partial pressure of CO₂ was performed in this study. Figure 4.7 exposes the effect of partial pressure of CO₂ on the linear kinetics of 441 at 800°C. The experimental results showed that the kinetics increase rapidly for low partial pressures to 400 mbar and much slightly increased for higher partial pressures.

Once again, the mass gain increased quickly at the initial state with the mass gain of approximate 0.01 mg cm^{-2} at all partial pressures.

The pressure dependence of 441 on the linear kinetics constants was plotted as shown in Figure 4.8. The result showed that this constant increases with increasing P (CO_2), tending to a constant value for the highest pressures.

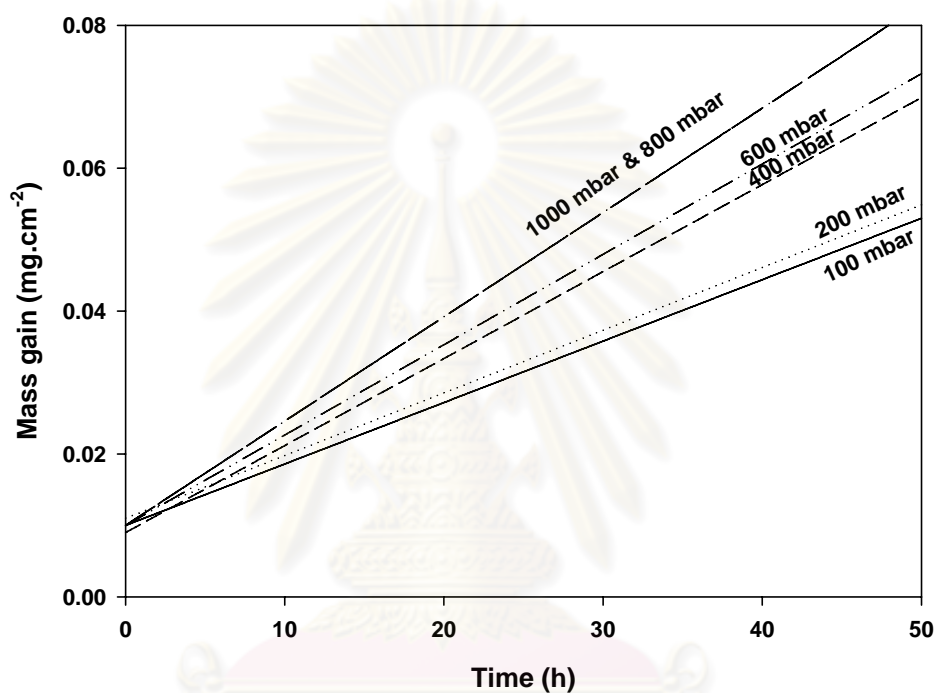


Figure 4.7: Oxidation kinetics of 441 under several partial pressures of CO_2 at 800°C .

ศูนย์วิทยทรัพยากร
จุฬาลงกรณ์มหาวิทยาลัย

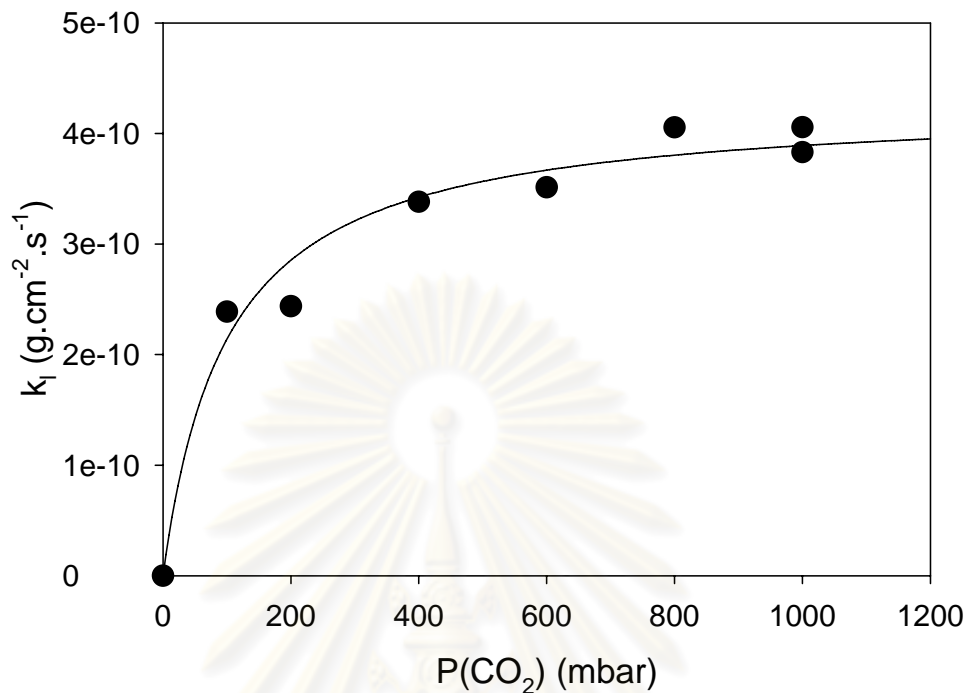


Figure 4.8: Pressure dependence of 441 on the linear kinetics constants at 800°C.

The constants in figure 4.8 were correctly fitted with the curve, resulting in the classical hyperbolic function following

$$k_l = \frac{AP_{CO_2}}{1 + BP_{CO_2}} \quad (4.3)$$

with A and B constant values given in Table 4.3.

Table 4.3: Constants of the hyperbolic equation (4.3) by regression method

Parameter	Value	StdErr	CV(%)	Dependencies
A (mg.cm ⁻² .s ⁻¹ .mbar ⁻¹)	3.92 x 10 ⁻¹²	7.75 x 10 ⁻¹³	19.77	0.98
B (mbar ⁻¹)	8.99 x 10 ⁻³	2.14 x 10 ⁻³	23.79	0.98

According to the result above, it is found that the linear constants depend on the adsorption of CO₂ molecule. This experiment will lead to the discussion of the possible model of oxidation kinetics later.

4.4 Scale Characterization

4.4.1 AISI 441

4.4.1.1 X-ray diffraction analysis

XRD was used for analysing the phases existing in the scale of 441 grade oxidized in pure CO₂ at 800°C for period up to 200h. The result of XRD is depicted in Figure 4.9.

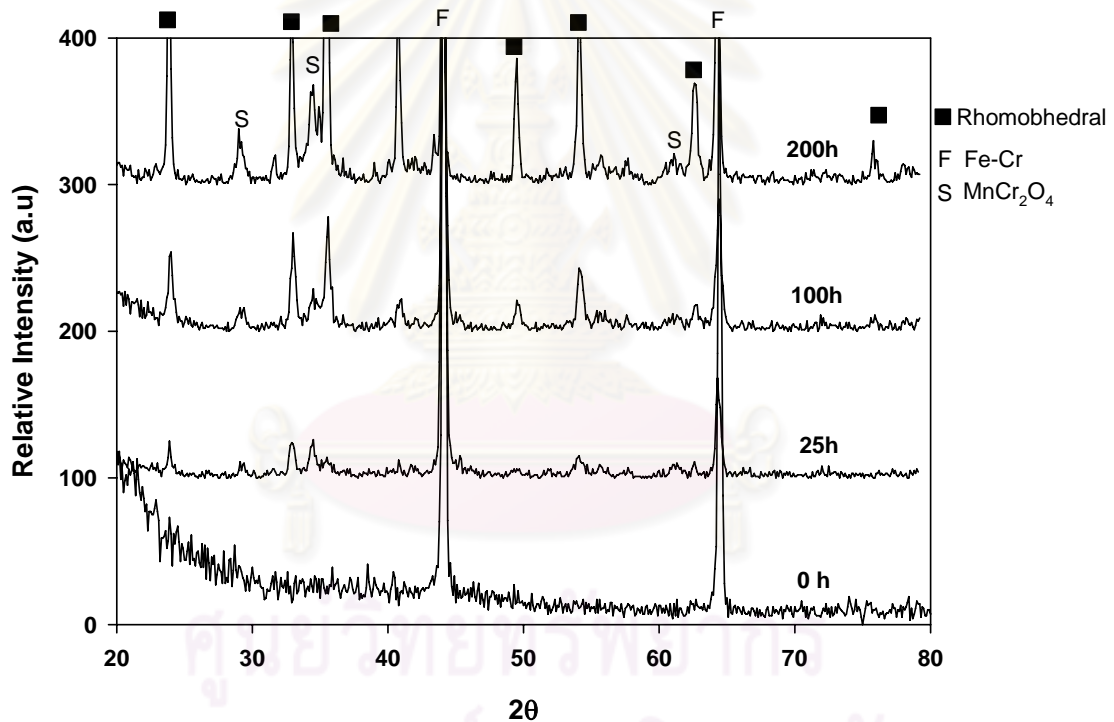


Figure 4.9: XRD pattern of 441 oxidised in pure CO₂ at 800°C for period up to 200h.

X-ray diffraction analysis of scales grown at 800°C for various times showed the presence of rhombohedral of (Fe,Cr)₂O₃ or chromia Cr₂O₃ (ICDD card 38-1479) and chromium-manganese spinel (Cr,Mn)₃O₄ (ICDD card 54-0876). Solid solution of (Fe, Cr)₂O₃ appeared as the major phase, but the amount of phases increased with increased oxidation time due to the increasing intensity.

4.4.1.2 Photoelectrochemistry experiments

The results of PEC experiments are presented in Figure 4.10 and 4.11 for a sample oxidised at 800°C for 100 h. As observed for oxidation of 441 in O₂ at 650°C by Srisrual et al. (Srisrual 2009), they showed the presence n-type semi-conducting iron and iron /chromium oxides via the detection of 2 energy gaps (2.0 and 2.6 eV).

Transform in Figure 4.10 shows the energy gap of the first contribution to be close to 2.3 eV, corresponding to the rhombohedral (Fe, Cr)₂O₃ solid solution (Srisrual 2009) and the second contribution to be 3 eV, corresponding to chromia (Srisrual 2009; Young 1985).

The several photocurrent curves in function of potential with fix energy for oxide scale obtained by CO₂ oxidation at 800°C for 100h are revealed in Figure 4.11. Photocurrent versus potential spectra was recorded at light energy corresponding to energy gaps from figure 4.10 in order to determine the type of electronic conduction of the oxide scale. The curves in Figure 4.11 show continuously increasing photocurrent with increasing potential, leading to a clear characteristic of n-type semiconducting oxides. This is in agreement with n-type behaviour when chromia equilibrated with a low oxygen partial pressure (Srisrual 2009; Young 1985). This may be also the result of doping with Fe³⁺.

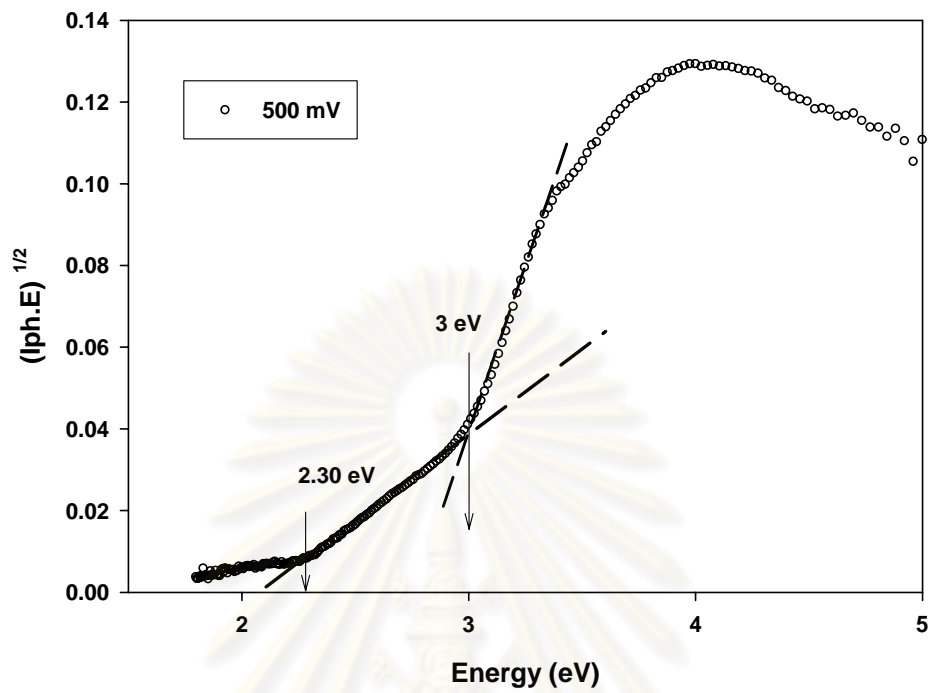


Figure 4.10: Linear transforms of curves from energy spectra for 441 oxidised at 800°C in CO₂ for 100h.

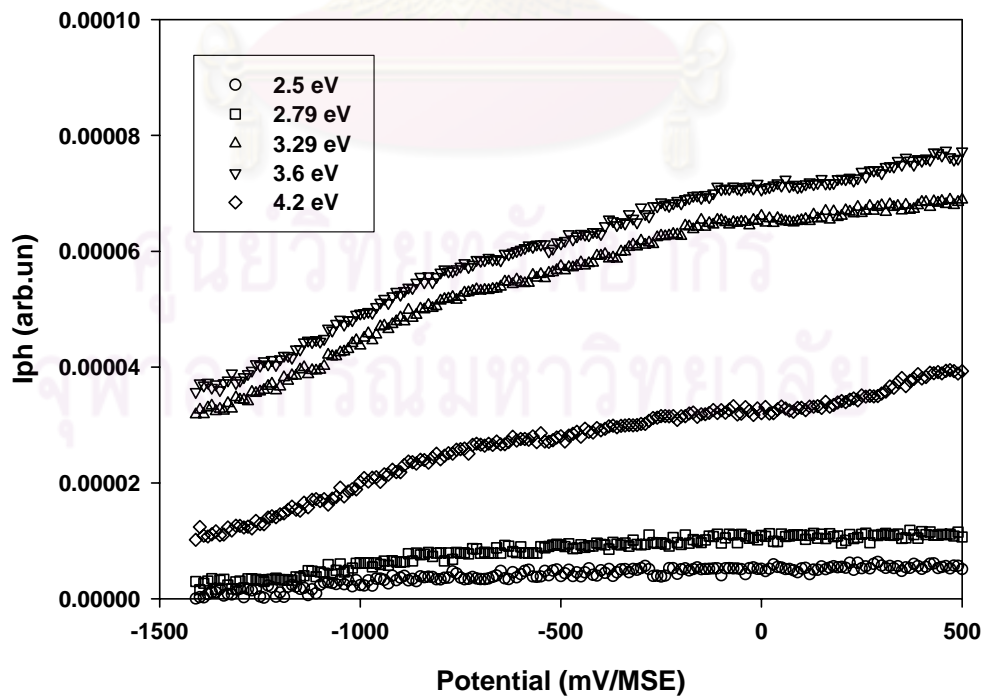
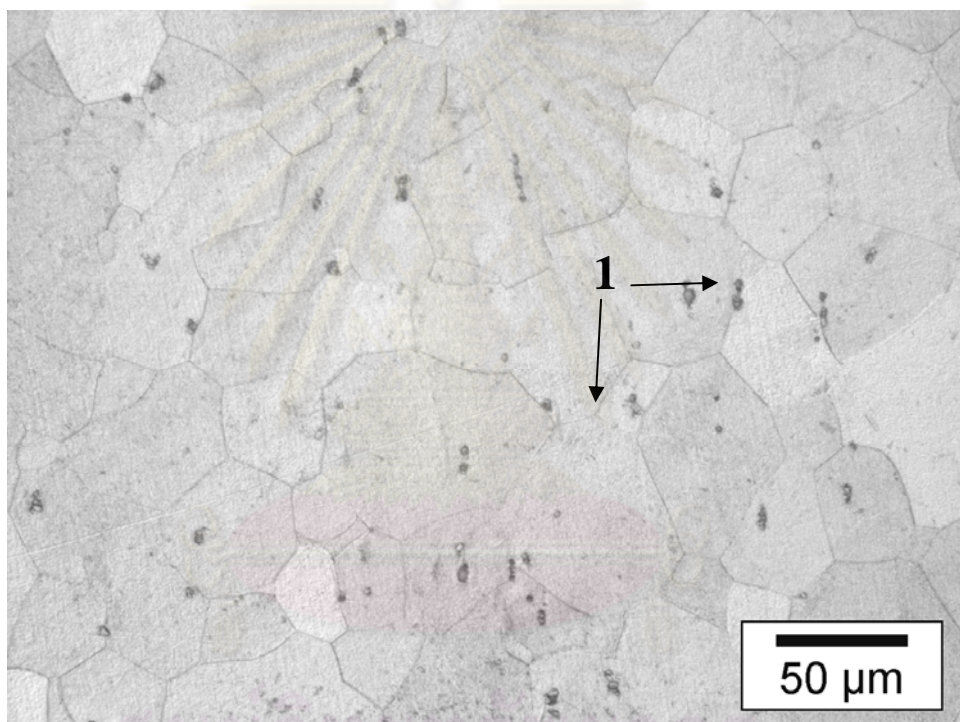


Figure 4.11: Photocurrent vs. potential curves for the sample of Fig. 4.11 analyzed at several light energy.

4.4.1.3 Scale morphology

The 441 before oxidation was ground, polished and chemically etched in order to examine grain boundaries by using conventional optical microscope as shown in Figure 4.12. The average grain size is about 80 μm and there are some precipitation appearing near grain boundaries. The precipitated phase (designated as 1) was determined by EDX. It was found that this phase in Ti- and Nb-rich may be Laves phase (Fe_2Nb or Fe_2Ti).



a)

ศูนย์วิจัยเทคโนโลยีการ
จุฬาลงกรณ์มหาวิทยาลัย

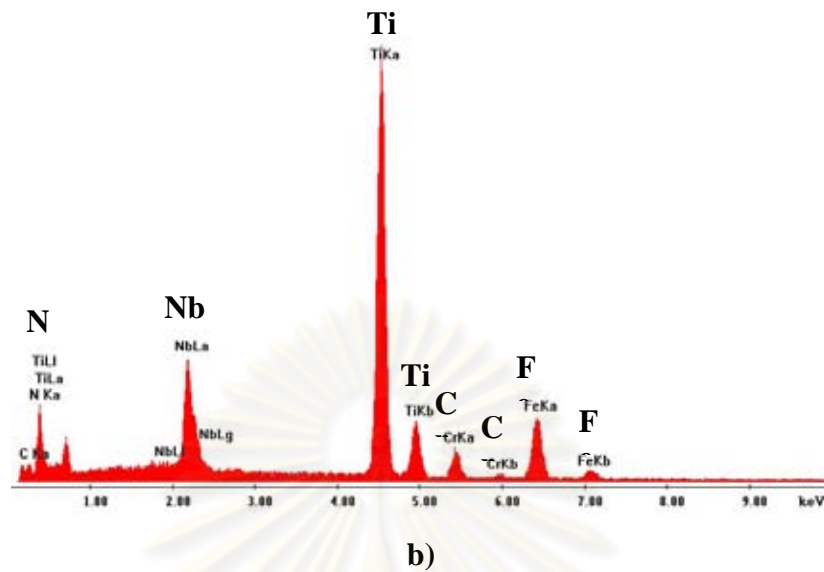


Figure 4.12: a) Metal surface observed by optical microscopy and b) EDX analysis of the precipitated phase in 441 before oxidation.

Figure 4.13 depicts the surface morphology of 441 oxidised during 25 h at 800°C in pure CO₂. The surface is rather smooth with oxide about 1 μm in size. The oxide surface (designated as 1) is enriched in chromium (Cr). Cr₂O₃ formed as the major scale on the surface, showing also a small Si peak due to SiO₂. Nodular oxides in Ti-rich were also dispersed over the entire scale surface.

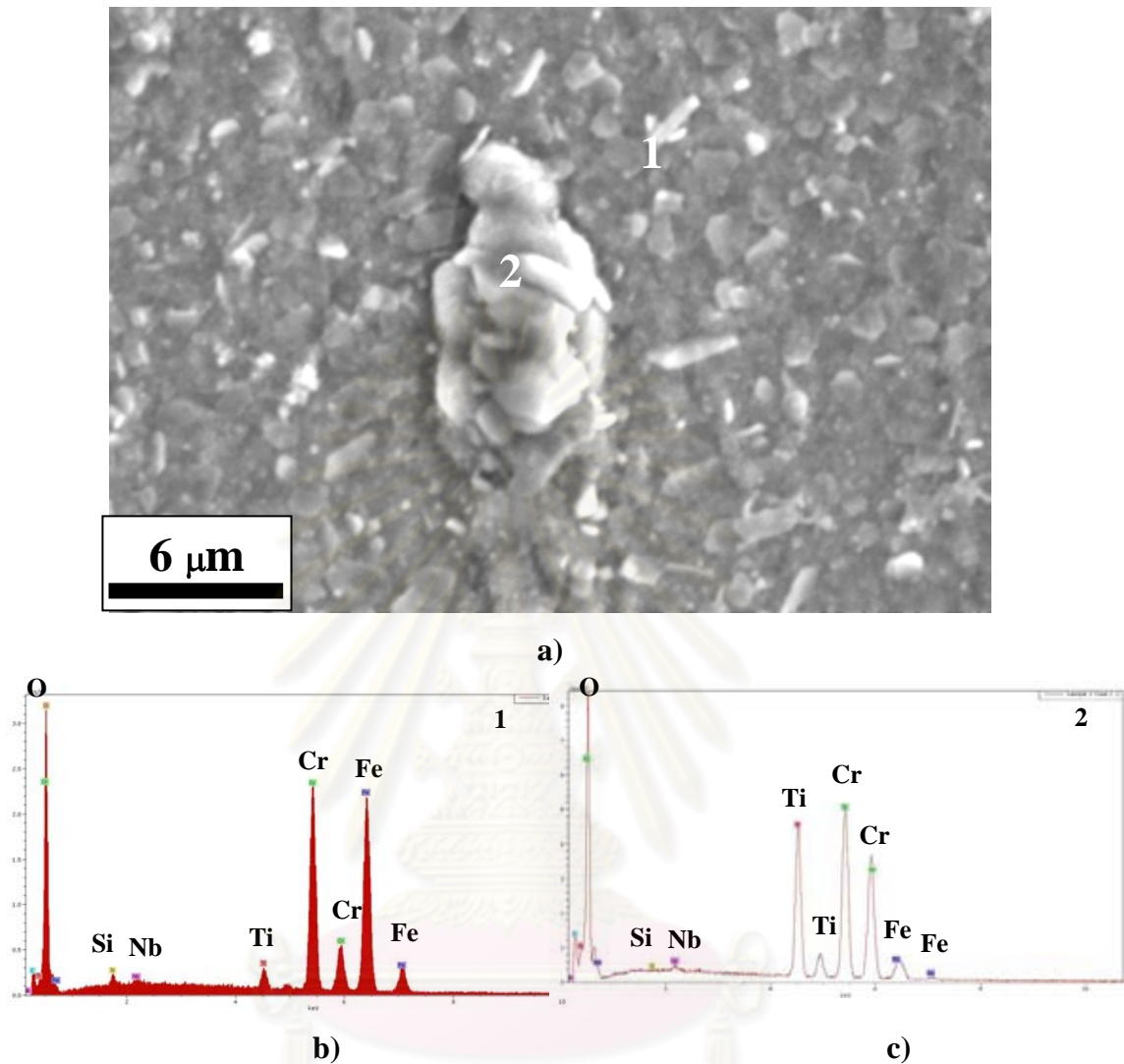


Figure 4.13: a) Surface morphology of 441 oxidised during 25h at 800° in pure CO₂;
 b) EDX analysis of point 1 and c) EDX analysis of point 2

Figure 4.14 presents the surface morphology of 441 oxidised at 800°C during 100h. It was found that the general features of Cr oxide were formed on the surface with additional small spherical nodules of oxide in Ti-rich (designated as 1). It may be noted that the size of nodular TiO₂ was various. Moreover, small faceted crystals (designated as 2) were observed which may be the spinel phase (Mn,Cr)₃O₄.

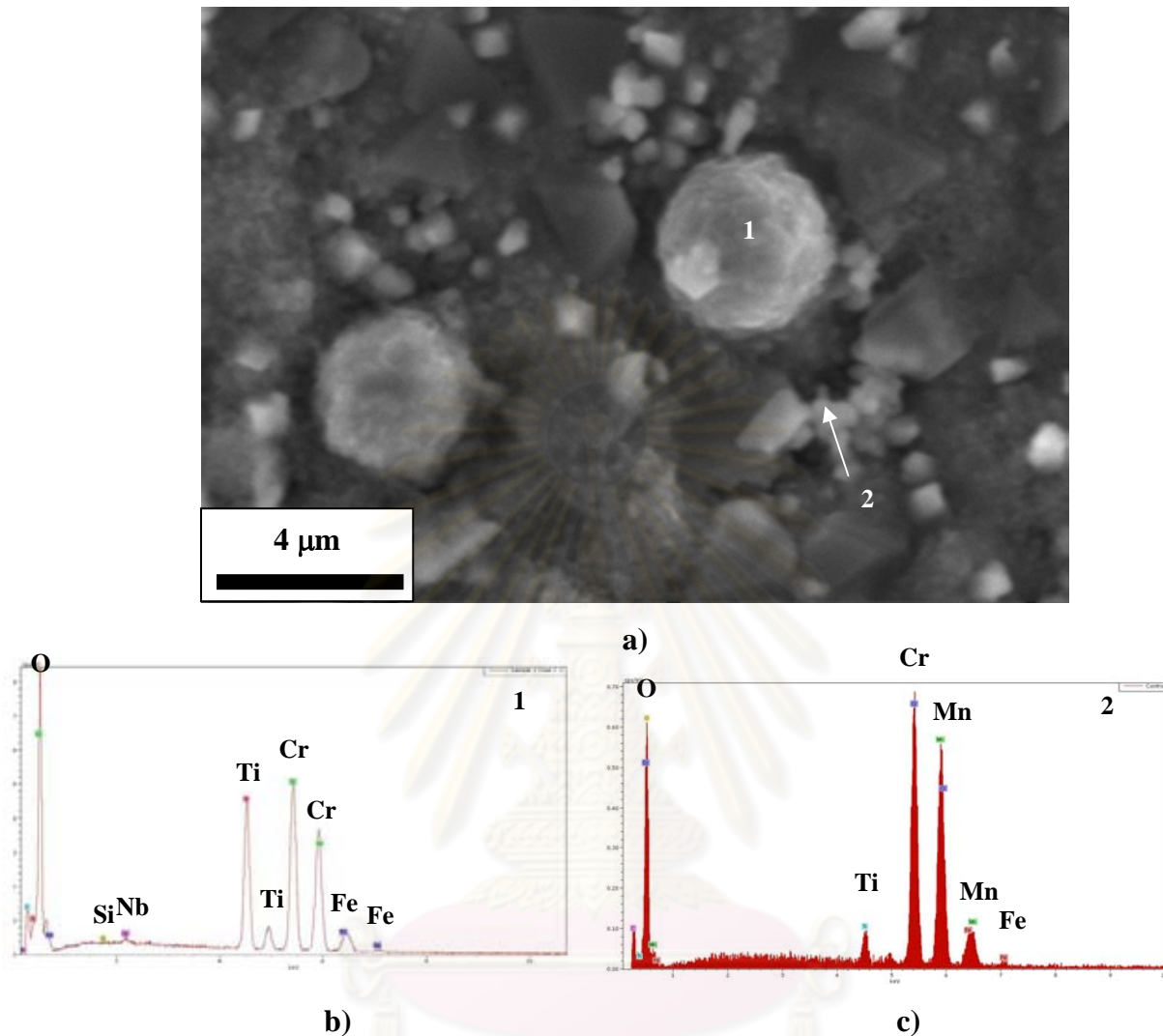


Figure 4.14: a) Surface morphology of 441 oxidised during 100h at 800° in pure CO₂
 b) EDX analysis of nodular oxide and c) EDX analysis of faceted crystals

Figure 4.15 depicts the surface morphology of 441 oxidised in pure CO₂ at 800°C up to 200h. It was observed that the oxide nodules size was in order of 10 μm and the nodules grew while the duration increased. It can be noted that the massive nodules in Ti-rich were spread on the top layer of pyramidal crystal of spinel Mn, Cr.

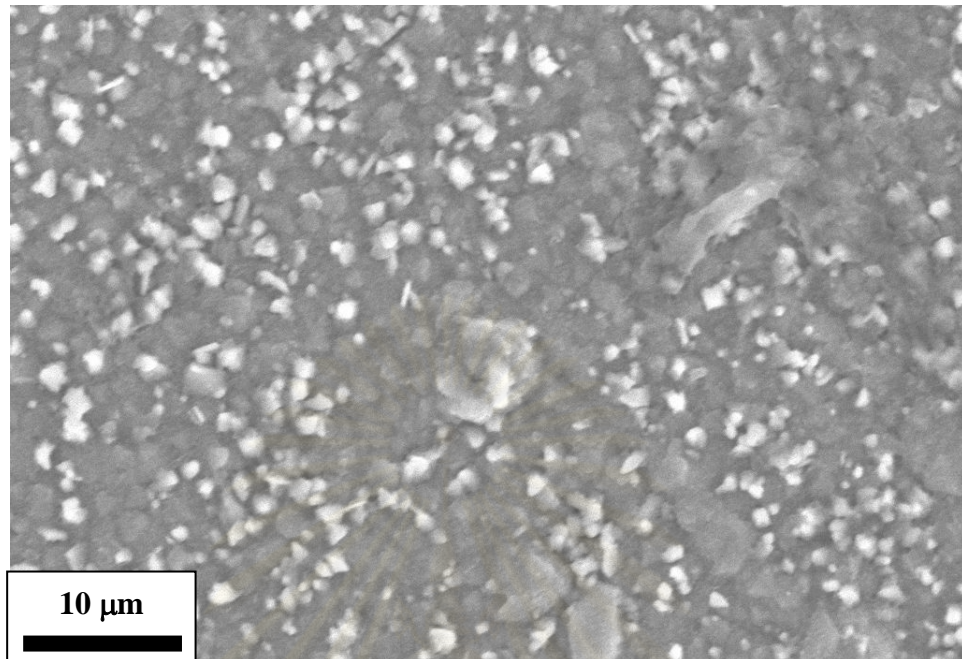


Figure 4.15: Surface morphology of 441 oxidised in pure CO₂ at 800° C during 200h

4.4.1.4 Markers experiment

In order to observe the transport mechanisms, the Pt markers experiments were performed by deposition small Pt particles on the metal prior to oxidation. After 100h at 800°C, Pt location can not be identified apparently in the cross section. It can possibly show that the chromia scale can developed by inward anionic or outward cationic growth or both.

4.4.2 Crofer22APU

4.4.2.1 X-ray diffraction analysis

The XRD results obtained after Crofer oxidation were shown the similar features. Figure 4.16 reveals the comparison of XRD patterns of 441 and Crofer22APU oxidised in pure CO₂ at 800°C for oxidation period of 200h.

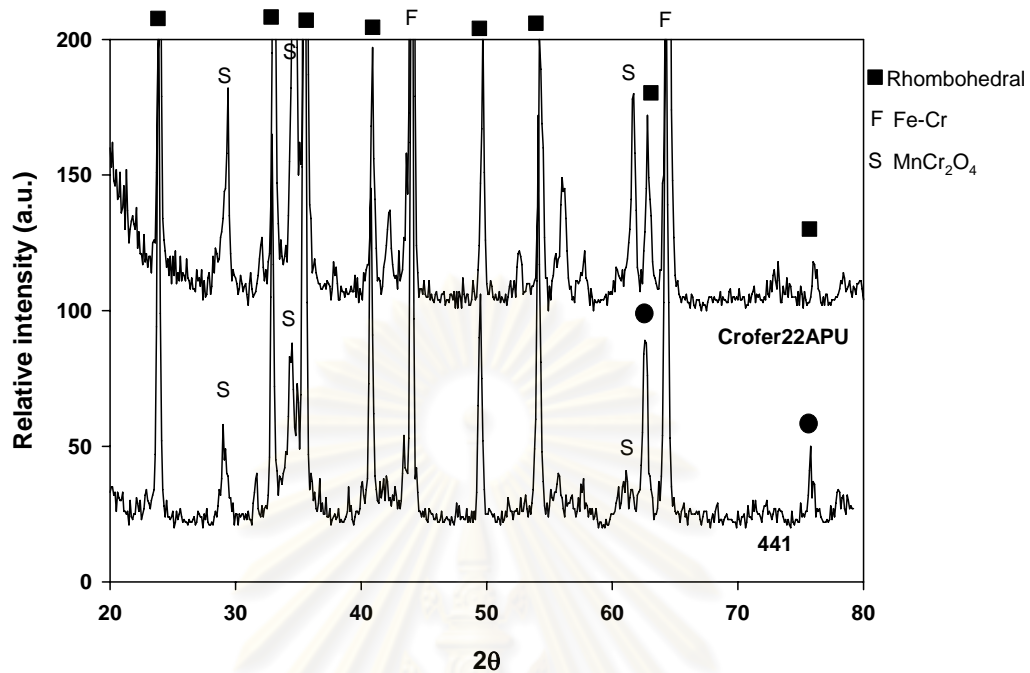


Figure 4.16: Comparison of XRD patterns of 441 and Crofer22APU oxidized in pure CO_2 at 800°C for 200h.

The peaks of rhombohedral $(\text{Fe,Cr})_2\text{O}_3$ or chromia Cr_2O_3 (ICDD card 38-1479) as well as chromium-manganese spinel $(\text{Cr,Mn})_3\text{O}_4$ (ICDD card 54-0876) were observed. This observation is identical to the case of conventional stainless steels, AISI441, in the same condition.

4.4.2.2 Scale morphology

Figure 4.17 reveals the oxide morphology of Crofer22APU oxidized in pure CO_2 at 800°C for oxidation period of 200h. The observation of oxide morphology was identical to that of 441. The elliptical Ti oxide nodule (designated as 1) was observed on the Cr oxide and spinel Mn-Cr layer (designated as 2). It seemed that the oxide surface was smoother than that of 441.

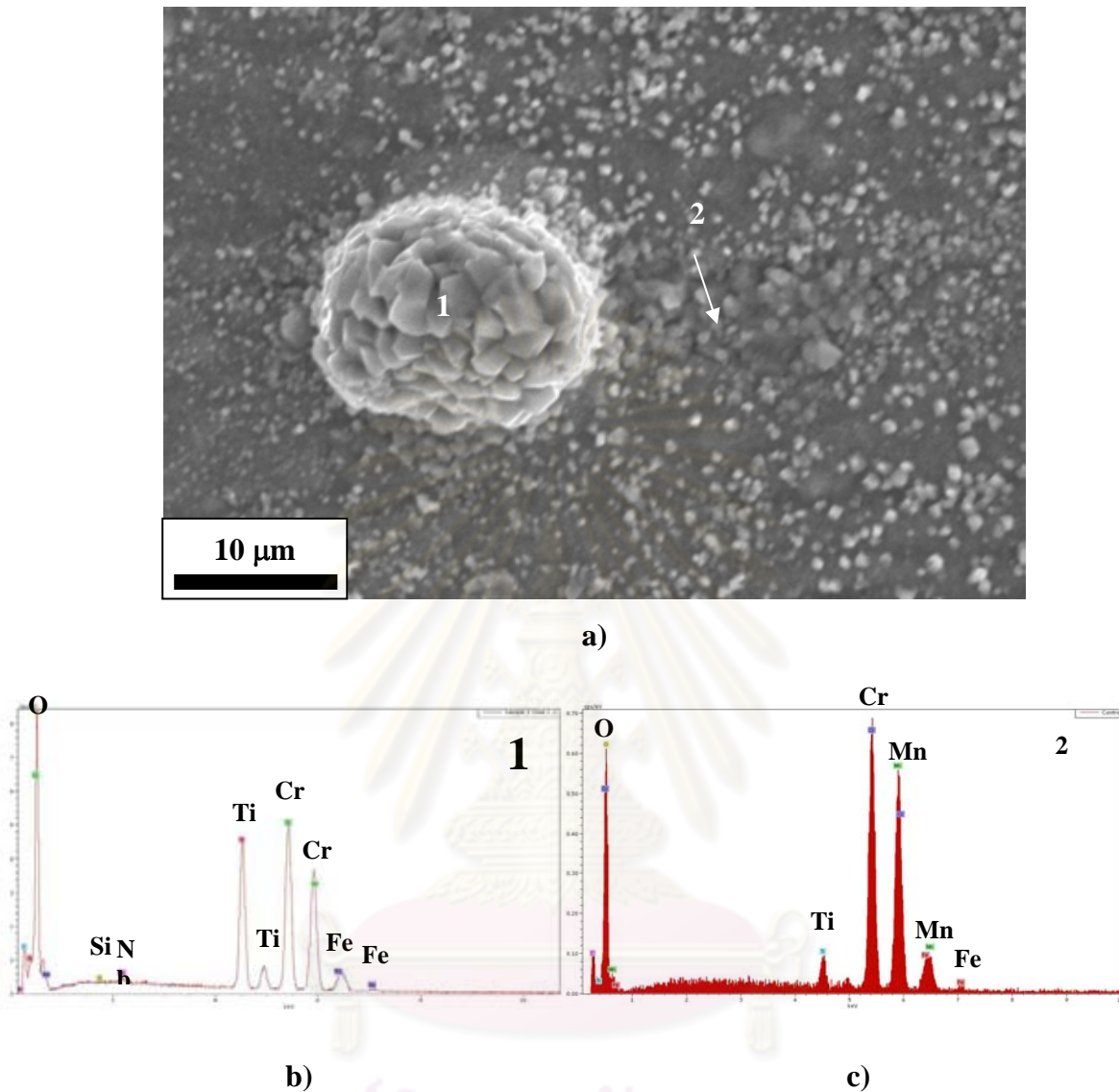


Figure 4.17: a) Surface morphology of Crofer22APU oxidised during 200h at 800° C in pure CO₂ b) EDX analysis of point 1 and c) EDX analysis of point 2

Basing on the SEM-EDX and XRD results, the schematic sketch of the evolution of the growth of oxide scale on 441 and Crofer22APU is schematised in Figure 4.18. It may be discussed that at the early stages of oxidation (25 h in this study), the major oxide is the rhombohedral oxide (Fe,Cr)₂O₃, in addition the existence of SiO₂ near the metal–oxide interface, with a top dispersion of (Mn, Cr)₃O₄ crystallites. When the oxidation progressed, the dispersed Mn,Cr spinel became dense and covered the Cr₂O₃ major oxide. TiO₂ was also dispersed on the spinel phase.

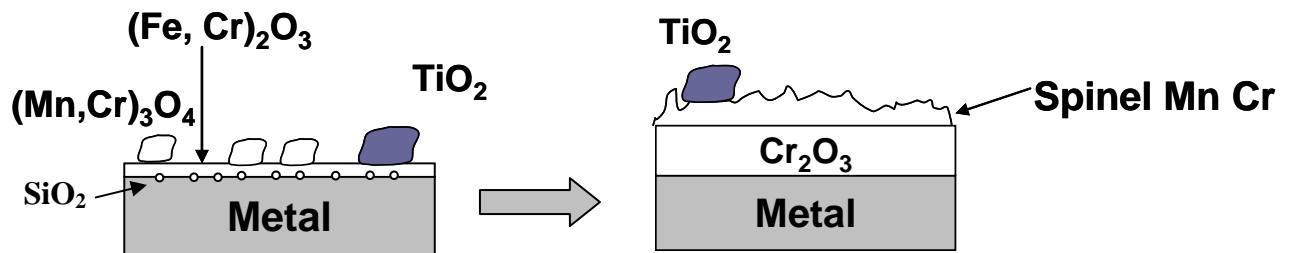


Figure 4.18: Schematic sketch of the evolution of the growth of oxide scale on 441 and Crofer22APU oxidised in pure CO_2

Knoop microhardness experiments were performed in the subsurface zone (10 μm from alloy-scale interface) on cross sections of samples oxidized in pure CO_2 at 800°C during 100 h to assess the presence of carbon. The results showed high hardness values (29 HK) in this zone, compared to the bulk value (~ 4 HK). Such a high value may reveal the carburization of the subsurface zone. Chemical etching for revealing carbides was therefore applied and showed that carburization of the steel is effective in these corrosion conditions (Figure 4.19). Titanium carbide seems the major product of this carburization, as revealed by EDX.

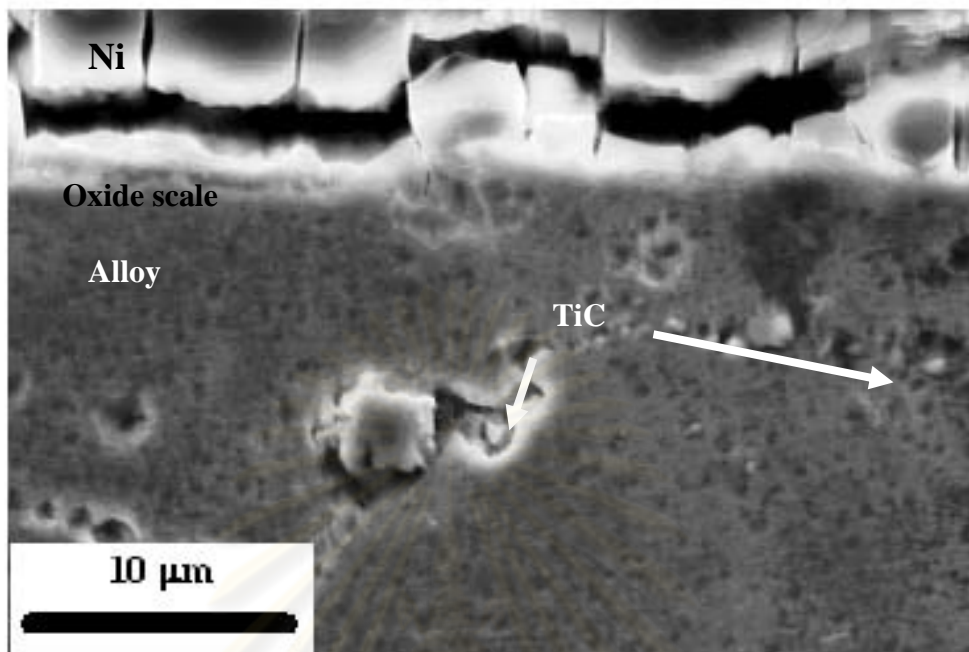


Figure 4.19: Cross section of 441 oxidised in pure CO_2 at 800°C during 100 h after chemical etching for carbides.

4.5 Mechanism of Oxidation Modeling

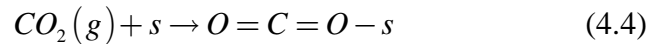
The formation of the chromia-rich scale topped with manganese spinel is the commonly observed situation when oxidising 441 in oxygen or air. In these atmospheres, oxidation kinetics are parabolic, resulting from limitation by chromium diffusion through the growing scale. This is what was observed in the present work for high temperatures and long oxidation exposures at intermediate temperatures.

However, a particular behaviour was evidenced at the lowest temperatures, where oxidation kinetics were shown to be linear. This may be due to chemical limitation at the scale-gas interface. Several models may be proposed to describe oxygen incorporation in chromia at this interface. They depend on the nature of the major point defect of this oxide.

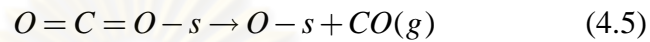
According to PEC experiment, assuming only the appearance of Cr oxide, n-type chromia with $\text{Cr}_i^{\bullet\bullet\bullet}$ interstitial chromium ions was proposed as the major defect,

a possible scenario can be written as follows (Kröger and Vink notation for point defects):

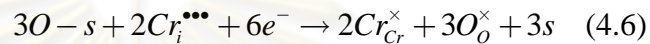
Chemisorption of carbon dioxide onto chromia (s is an adsorption site)



Adsorbed carbon dioxide decomposition with evolution of gaseous carbon monoxide



Oxygen transfer to the oxide



Reaction at the metal-chromia interface



In such a model, all 4 steps considered to be rate-limiting alone lead to linear kinetics, but the only one fitting with the experimentally observed homographic influence of pressure described by equation (4.3) is the decomposition step (4.5). The reaction rate r_d limited by carbon dioxide decomposition can be written:

$$r_d = k' \theta_{CO_2} \quad (4.8)$$

Extracting the surface coverage by CO_2 from the equilibrium constant (Langmuir isotherm)

$$\theta_{CO_2} = \frac{K_s P}{1 + K_s P} \quad (4.9)$$

The reaction rate comes as follows

$$r_d = k' \frac{K_s P}{1 + K_s P} \quad (4.10)$$

where k' is the rate constant for the CO_2 decomposition step (the reverse reaction being supposed infinitely slow), P the CO_2 pressure, K_s the equilibrium constant for CO_2 adsorption and θ_s the equilibrium surface coverage of the oxide by CO_2 .

This expression fits very well the experimental data with the following parameters

$$k' = 4.36 \times 10^{-10} \text{ g.cm}^{-2}.\text{s}^{-1}$$

$$K_s = 8.99 \times 10^{-3} \text{ mbar}^{-1}$$

The apparent activation energy of 200 kJ.mol^{-1} was measured on the pressure plateau of figure 4.8, where $K_s P \gg 1$. It appears therefore that this value refers to the actual activation energy on k' and refers to the decomposition step only.

Comparing the linear rate constants obtained in this work with those reported by Vallette et al. (Vallette, 2005) for oxidation of iron in CO_2 , shows that the present linear constants are inferior by several orders of magnitude. Activation energy is also slightly lower (245 kJ.mol^{-1} for the reaction $\text{Fe} + \text{CO}_2$). This is not surprising as surface chemisorption and catalysis highly depend on the chemistry of the growing oxide. However, the presented reaction model is not dependent on the choice of the formed oxide as the oxygen incorporation into the oxide does not appear in the kinetic equation for rate law. Remembering that the oxide-gas reaction may involve chromium-manganese spinel and not chromia does not change the discussion and the fit to the CO_2 pressure influence.

In the parabolic regime, all surface steps are considered to achieve equilibrium and the reaction rate is classically described by the Wagner theory. Assuming chromia formation only, the scale thickness can be expressed as

$$\frac{2}{i} \frac{dy}{dt} = 3D_{Cr} \frac{(Cr_i^{\bullet\bullet\bullet})_{int} - (Cr_i^{\bullet\bullet\bullet})_{ext}}{y} \quad (4.11)$$

with y the chromia thickness

t the time of oxidation

$1/2 i$ the equivalent volume of chromia for 1 mol Cr ($i = 7.13 \text{ cm}^3.\text{mol}^{-1}$)

D_{Cr} the diffusion coefficient of interstitial chromium defects in chromia.

$(Cr_i^{\bullet\bullet\bullet})_{int}$ and $(Cr_i^{\bullet\bullet\bullet})_{ext}$ the molar fraction of chromium defects at the internal and external interfaces respectively.

Assuming no molar fraction of chromium defect at external interface, it is observed that the parabolic constant (k_p), equivalent to the diffusion coefficient of Cr in chromia is the multiplication of diffusion coefficient of interstitial chromium defect in chromia and the molar fraction of chromium defects at internal.

As observed in experiments, the thickness of the scale is given, for 925 - 1000°C, by

$$y^2(cm^2) = 77.06 \exp\left(\frac{-3.95 \times 10^4}{T}\right) t \quad (4.12)$$

The oxidation kinetics of ferritic stainless steel type AISI441 under CO₂ atmosphere can be summarized as follows:

a) The surface morphology shows the major Cr oxide topped with spinel Mn–Cr with dispersed TiO₂ by SEM-EDS and XRD in agreement with thermodynamic calculation.

b) The oxidation kinetics is in parabolic function at high temperatures (>925 °C) due to molecule diffusion and in linear function at lower temperatures and initial stage due to interface limitation.

c) The kinetic constants of 441 are identical to Crofer under CO₂ atmosphere

d) The parabolic constants of ferritic stainless steels in CO₂ are higher compared with those in synthetic air or 20% O₂/Ar.

e) The linear constants of ferritic stainless steels are inferior to that of iron in the same atmosphere

f) Oxide behave as n-type of semiconduction with the possible phase such as Fe³⁺ doped Cr₂O₃.

g) A defect model was proposed with n-type chromia containing Cr_i^{••} interstitial chromium ions as the major defect

ศูนย์วิจัยทรัพยากร
จุฬาลงกรณ์มหาวิทยาลัย

Chapter V

Corrosion behaviour of ferritic stainless steels exposed to synthetic biogas at high temperatures

5.1 Introduction

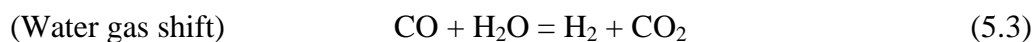
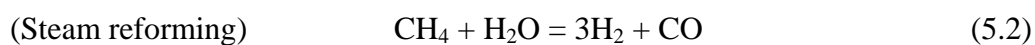
The success of use of ferritic stainless steels as SOFCs applications in synthetic air and hydrogen humidified was reported by Chandra-ambhorn (Chandra-ambhorn, 2006). However, for experimental use of fermentative biogas instead of hydrogen as a superior choice atmosphere in anode side due to their primitive and renewable nature (Herle, 2004-1), unfortunately, the corrosion behaviour have been not extensively studied. According to biogas composition, therefore, it is possible that the corrosion process would be not only oxidation but also carburization.

The objective of this study is to understand the corrosion behaviour of ferritic stainless steels under synthetic biogas. The study was carried out in terms of thermodynamic calculations, kinetic measurements and physico-chemical characterisation of the oxide scales formed in the presence of methane-carbon dioxide mixtures.

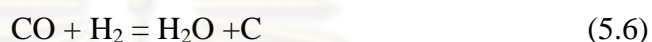
5.2 Thermodynamic Calculations

5.2.1 Thermodynamics of biogas

The possible reaction associated with the hydrogen production from biogas for SOFC are shown as follows



The possible carbon formation can be also described by the reactions as follows:



The most stable reaction involved the production hydrogen from biogas in SOFCs is reactions (5.1 and 5.5). The thermodynamic program Factsage with Fact53 database was used to calculate the complex equilibrium species and also the carbon activity (a_c). The carbon can be observed in the system when its activity is at least equal to 1. The results are shown with three volumetric ratio of methane in synthetic biogas.

a) 30% CH_4 + 70% CO_2

When methane is added in CO_2 , the reaction of this mixture will be more complicated than that of pure CO_2 (as described in chapter IV). The partial pressure of gases and activity of carbon are then determined in function of inverse temperature as shown in Figure 5.1.

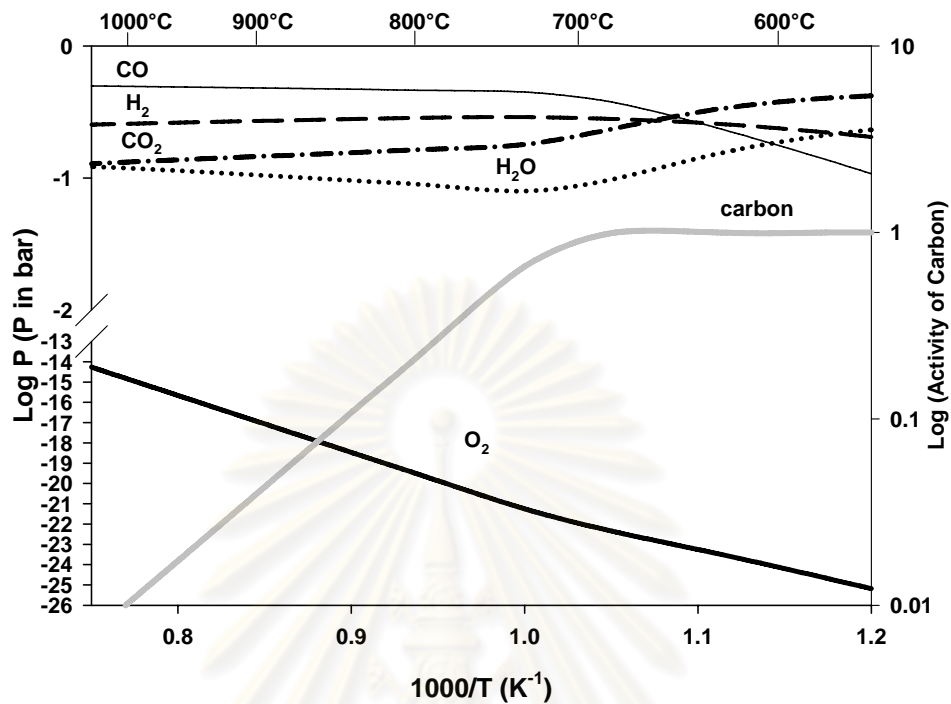


Figure 5.1: The logarithm of partial pressure of gases and activity of carbon in function of the reciprocal temperature in presence of 70% CO₂ + 30% CH₄.

It was found that, due to their biogas reactions, the partial pressures of O₂, CO and H₂ increase with increasing temperature. The partial pressures of CO and H₂ are, however, almost constant when temperature reaches to 700°C. Contrarily, pressure of CO₂ decreased while temperature increases. On the other hand, the water vapour decreased until 700°C and then slightly increased with increasing temperature. Moreover, the result showed that graphite can be possibly formed at temperature below 700°C.

b) 50% CH₄ + 50% CO₂

The possible equilibrium gases in 50% CH₄ + 50% CO₂ were computed at different temperatures as revealed in Figure 5.2.

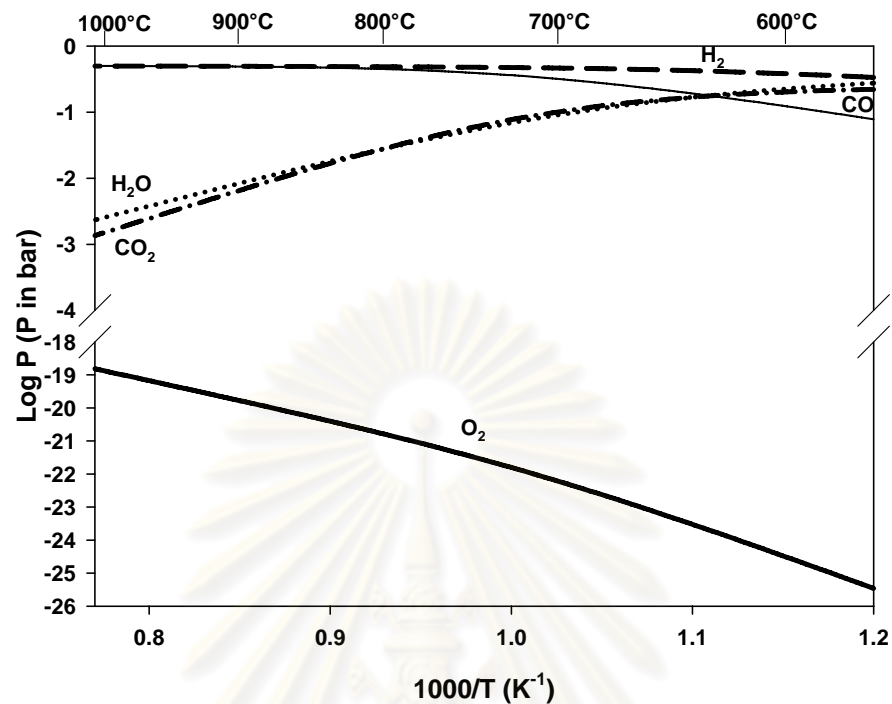


Figure 5.2: The logarithm of partial pressure of equilibrium gases in 50%CH₄ + 50%CO₂ in function of the reciprocal temperature.

The calculations showed that partial pressures of O₂, H₂, and CO increase when temperature also increases except water vapour (H₂O) and CO₂. The pressures of H₂ and CO are nearly constant when temperature reaches 800°C. Moreover, the calculation showed that the activity of carbon is always equal to 1, i.e. graphite is possibly formed in this condition.

c) 70% CH₄ + 30%CO₂

As same manner, the result of the calculations of partial pressures of gases is exhibited in Figure 5.3.

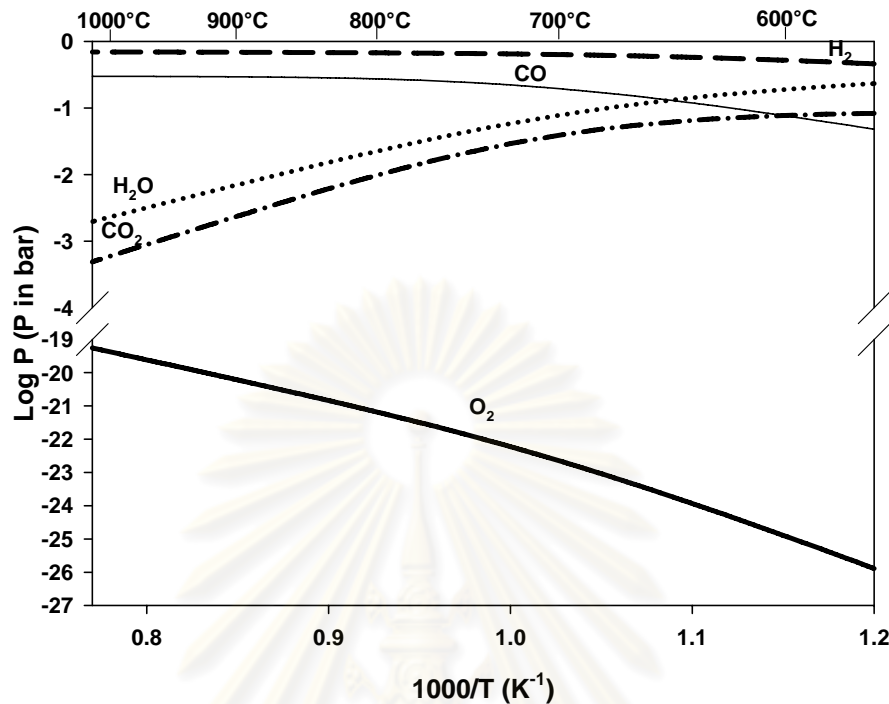


Figure 5.3: The logarithm of partial pressure of equilibrium gases in 70%CH₄ + 30%CO₂ in function of the reciprocal temperatures.

Same as the previous results, all pressures of gas increase when temperature also increases, except water vapour (H₂O) and CO₂. Moreover, the activity of carbon is always equal to 1. Therefore, graphite can be formed at all temperatures.

The partial pressure of O₂, H₂, H₂O and carbon can be concluded in function of the volumetric ratio of methane in the biogas as follows:

a) Oxygen

The logarithm of partial pressure of oxygen in function of the volumetric ratio of CH₄ is plotted in the temperature range of 600 – 1000°C as shown in Figure 5.4.

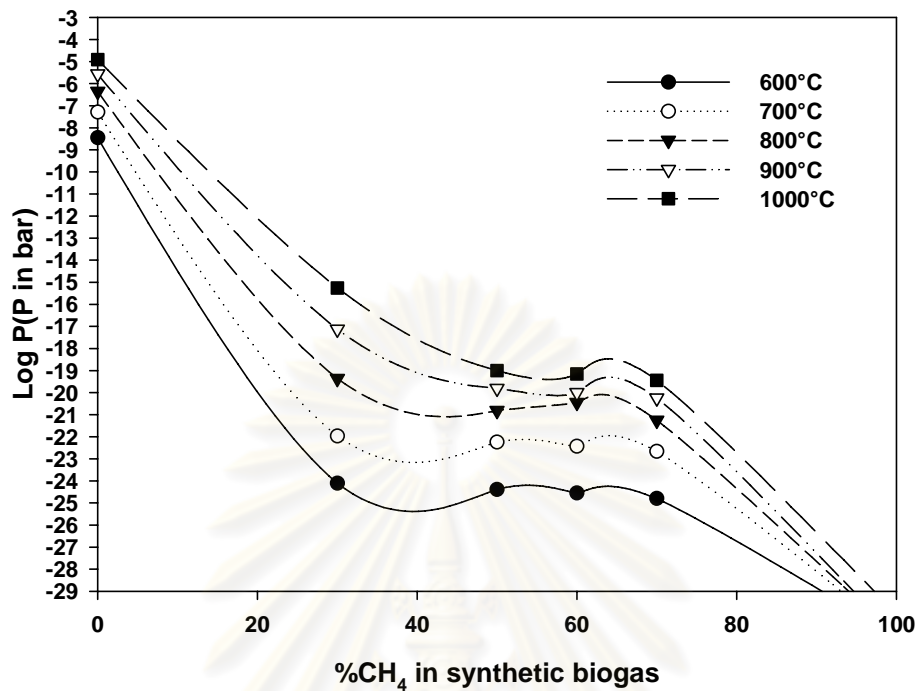


Figure 5.4: Partial pressure of oxygen plotted with volumetric ratio of CH₄ in synthetic biogas between 600 and 1000°C.

It can be concluded that, when the content of CH₄ in synthetic biogas increases, the partial pressure of oxygen decreases rapidly. When the quantity of methane reaches its composition in biogas (50-70%CH₄), the partial pressure of oxygen is almost identical at the same temperature. The calculations revealed that the partial pressure of oxygen in synthetic biogas (50-70%CH₄ and 30-50%CO₂) was 10⁻²⁵ to 10⁻²¹ bar at the range of intermediate temperatures of SOFCs (600 - 800°C).

Comparing to calculation of the partial pressure of oxygen in 2%H₂O/H₂ between 700 and 900°C by Chandra-ambhon (Chandra-ambhon, 2006), both calculations are approximately equal. It is therefore possible that the same type of oxides may be thermodynamically formed on steels in both atmospheres.

b) Hydrogen

Although hydrogen may be insignificant for the formation of metal oxide, it plays an important role in anodic reactions as gas oxidizing in SOFCs.

Using biogas instead of pure hydrogen may then reduce electrical efficiency due to concentration of hydrogen (Piroonlerkgul, 2008). The partial pressures of hydrogen in function of %CH₄ are therefore plotted in the temperature range of 600-1000° as shown in Figure 5.5.

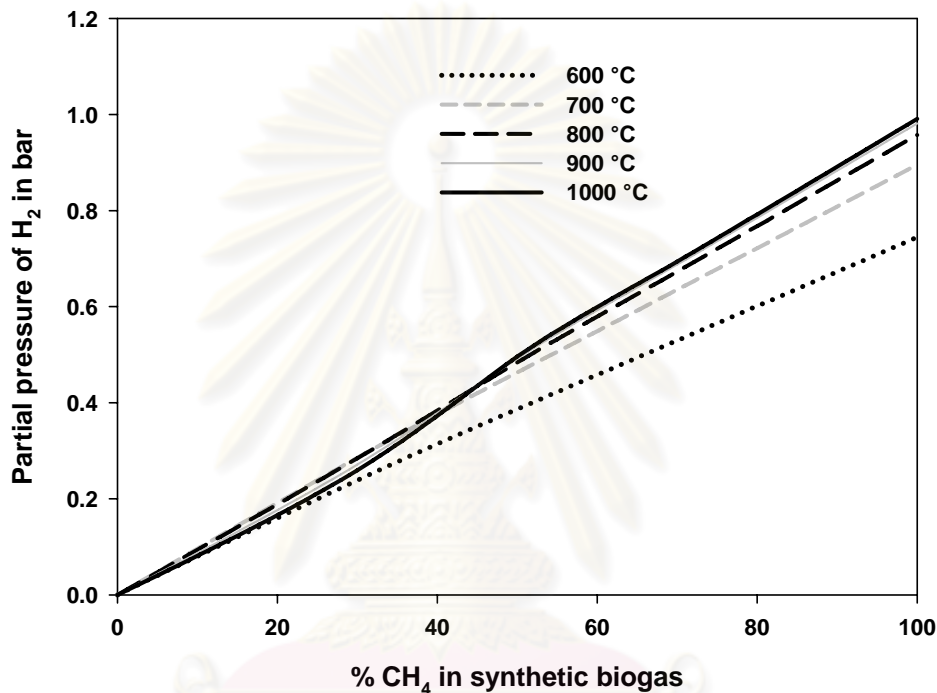


Figure 5.5: Partial pressure of hydrogen in function of volumetric ratio of CH₄ in synthetic biogas between 600 and 1000°C.

The calculations showed that the partial pressure of hydrogen increases near linearly while the content of methane in biogas also increases. The partial pressure of hydrogen obtained by the reaction in synthetic biogas (50-70%CH₄ and 30-50%CO₂) is about 0.4 to 0.75 bar between 600 and 1000 °C. The electrical efficiency may be so reduced by comparing with using pure hydrogen or humid hydrogen.

c) Water vapour (H₂O)

The partial pressures of water vapour in function of volumetric ratio of CH₄ are plotted in the temperature range of 600 – 1000°C as shown in Figure 5.6.

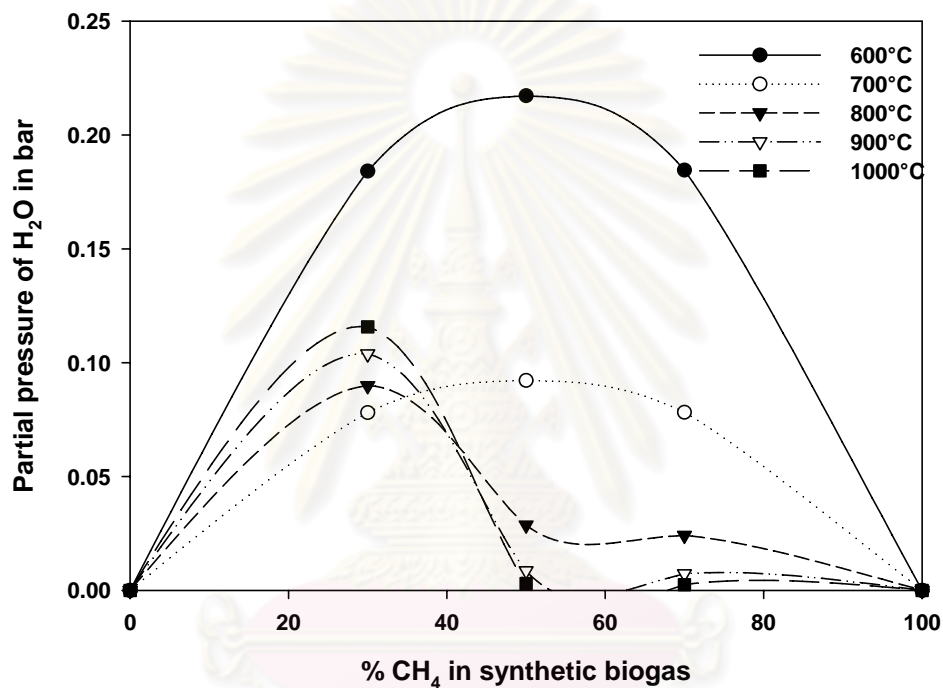


Figure 5.6: Partial pressure of water vapour in function of volumetric ratio of CH₄ in the synthetic biogas between 600 and 1000°C.

It is found that no water vapour formed at 0% and 100% CH₄ because of lack of oxygen. The partial pressure of water vapour at 600°C and 700°C increases swiftly with the increasing percentage of CH₄ up to 50% and then decreases alike parabolic shape. In the other hand, its pressure increased with the increasing content of methane till 30% and then decreases rapidly for higher temperatures. In addition, the partial pressure of water vapour is in order of 0.00251 to 0.23 bar (0.25 – 23%) between temperature in range of 600- 1000°C for biogas.

d) Solid carbon

It is possible that the graphite may be found in biogas system as shown in Figure 5.7. The grey zone represents the conditions in which carbon can be formed ($a_c > 1$), contrarily, there is no carbon in the white zone.

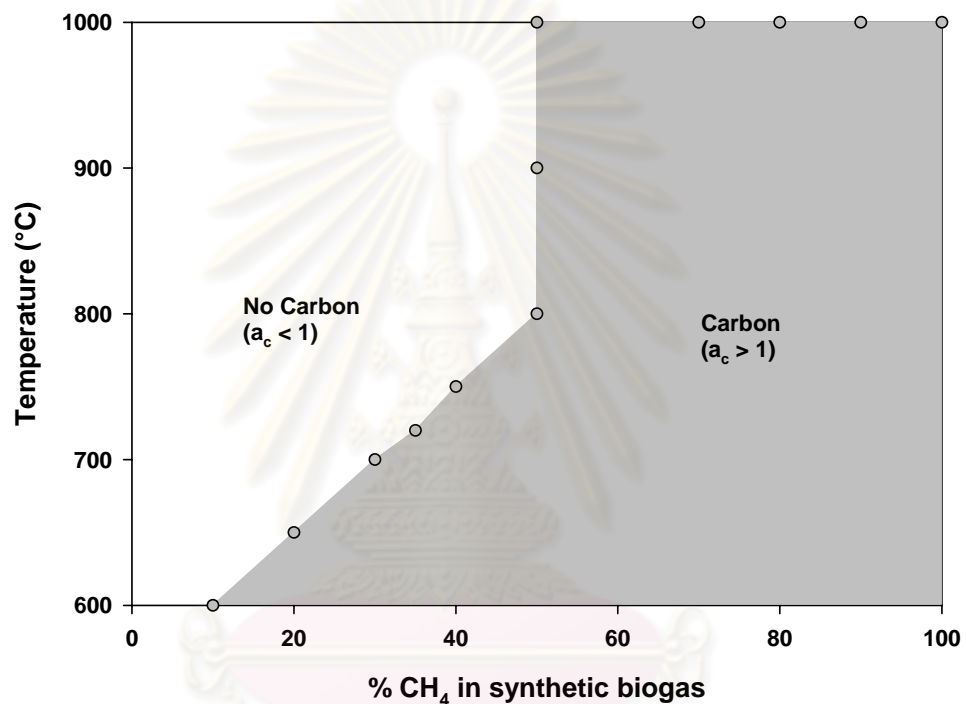


Figure 5.7: Schematic diagram of activity of carbon in synthetic biogas between 600 – 1000°C.

The result showed that the formation of carbon depends on the quantity of methane in the synthetic biogas and at the temperature. Graphite can be formed from 15% CH₄ in synthetic biogas at 600°C. However, according to the calculation, the carbon was feasibly formed in the system from 50% CH₄ at operating temperature of SOFCs (600-1000 °C). Therefore, the reactivity of stainless steels and synthetic biogas will probably lead to the mixing material degradation of oxidation and carburization.

It was, however, observed that there may be a relation between the formation of carbon and the existence of water vapour in the system. That is,

when water vapour in system is sufficient, the carbon can be feasibly eliminated. As revealed in reaction (5.6), when water vapour or steam is added in system, the activity of carbon will decrease at equilibrium.

The calculations of other researchers (Assabumrungrat, 2006; Piroonlerkgul, 2008) have reported that a reforming agent (air or steam) is required to inhibit the carbon formation. In these calculations, water vapour was the best choice for inhibiting the formation of carbon in biogas. The calculation of the mass fraction of water vapour required to inhibit carbon formation is displayed in Figure 5.8.

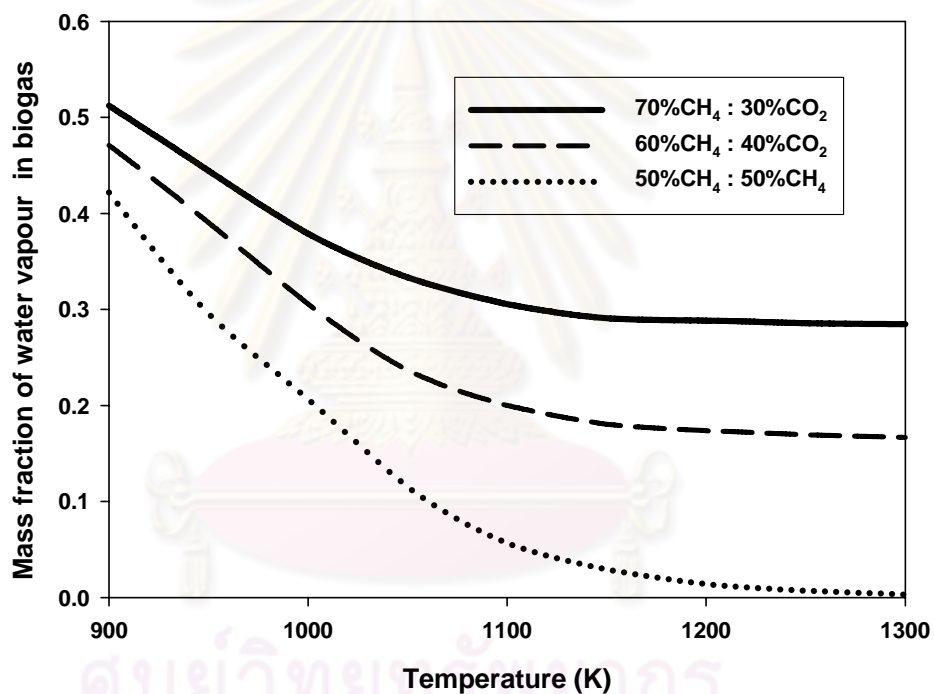


Figure 5.8: Mass fraction of water vapour required to inhibit carbon formation in different temperature and composition of biogas (Carbon is unstable above each curve).

This calculation shows the mass fraction of water vapour required decreases hyperbolically with increasing temperature, attaining almost constant value above about 1200 K. The mass fraction of water vapour is also required more in higher content of methane in order to eliminate thermodynamically the carbon formation. However, when the mass fraction of steam increases, the

electrical efficiency always decreases because the hydrogen in system also decreases (Piroonlerkgul, 2008).

Adding steam in the system can change the pressure of important gases in the system. Percent change of pressure of gas with mass fraction of water vapour required to inhibit the carbon formation in $70\%CH_4 + 30\%CO_2$ is exhibited in Figure 5.9.

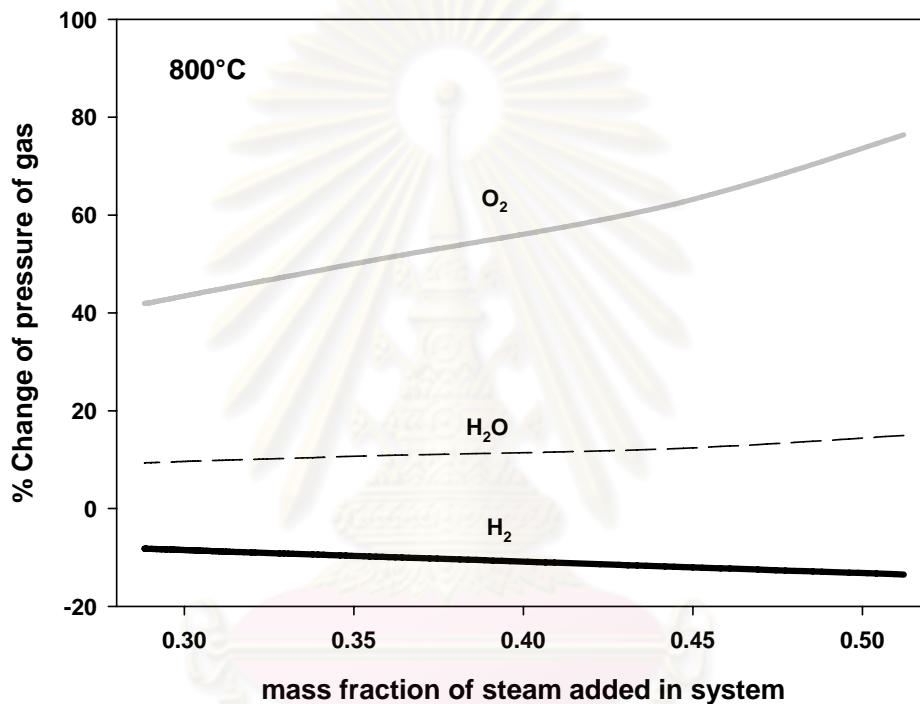


Figure 5.9: Percent change of pressure of H₂, H₂O and O₂ with the mass fraction of steam required in system of $70\%CH_4 + 30\% CO_2$.

It is found that the pressure of hydrogen will decrease slightly with the increasing mass fraction of steam. Inversely, the pressure of oxygen and water vapour will increase when the mass fraction of steam also increases. However, because the pressure of oxygen increases in order of 40 – 80%, the metal may be more oxidized in this condition.

5.2.2 Oxide stability diagram of AISI441

The oxide stability diagram of AISI441 in Figure 5.10 was derived from the appendix A by superposing the oxygen partial pressure generated by the biogas atmospheres.

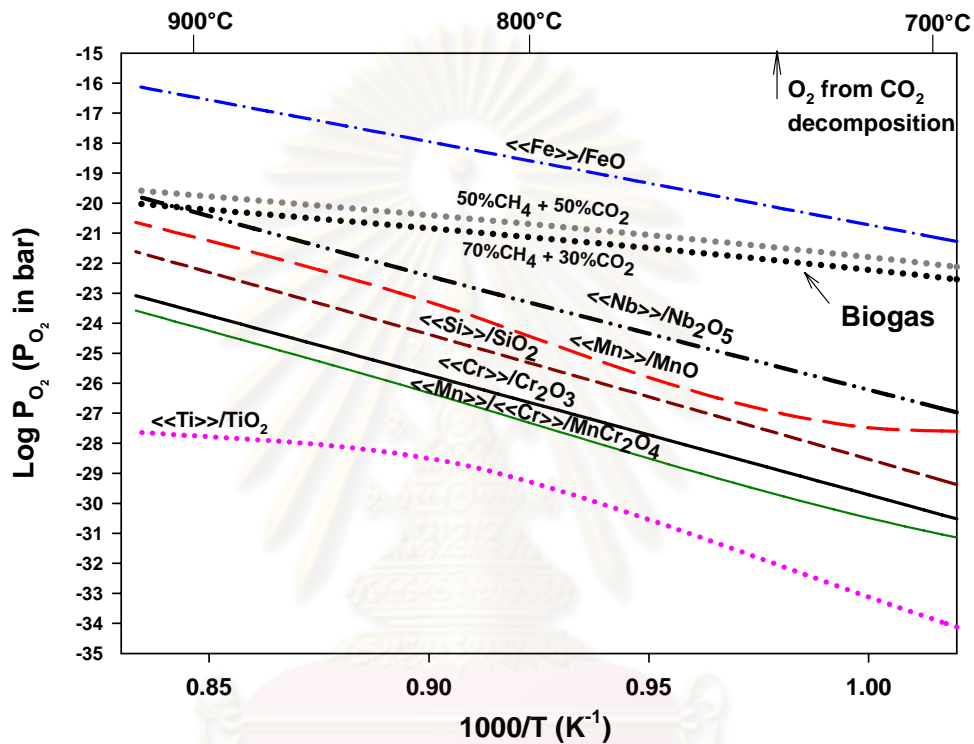


Figure 5.10: Oxide stability diagram of AISI441 in synthetic biogas for the temperature range 700-900°C.

In the range of 700 to 900°C, all important oxides will be possibly formed on 441 in contact with biogas except FeO. On the contrary, FeO can be formed in the 100% CO₂ atmosphere.

To assess the possible formation of iron oxide(s), leading to catastrophic oxidation, the pressures of oxygen with the evolution of methane in synthetic biogas was calculated and plotted in Figure 5.11.

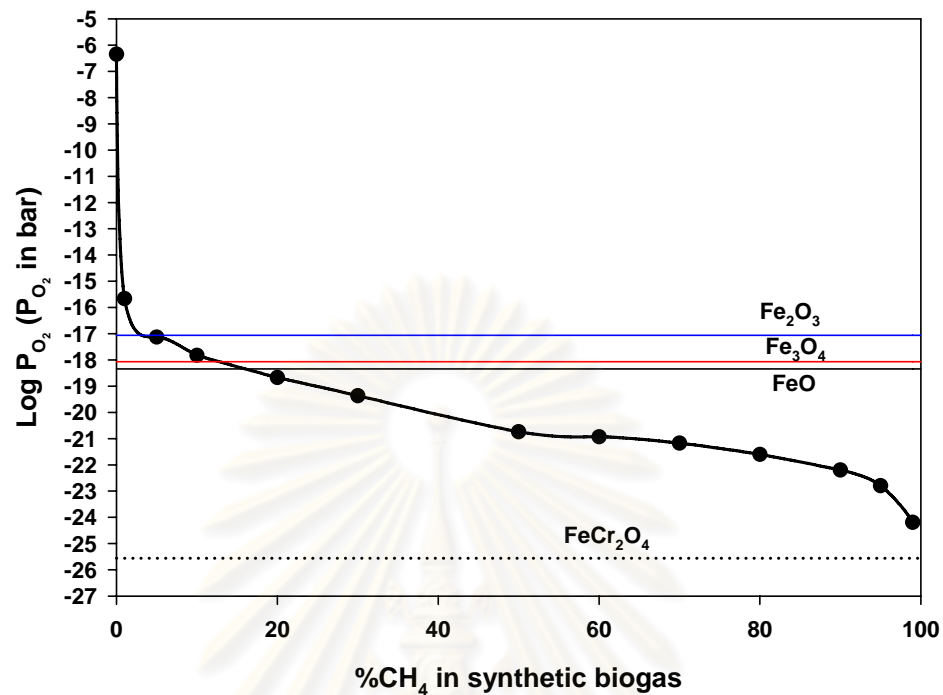


Figure 5.11: Pressure of oxygen with the evolution of CH₄ in the biogas comparing to the formation of iron oxide at 800°C.

It is observed that no catastrophic oxidation with iron oxides appearing on 441 subjected to biogas atmosphere could appear as the existence of iron oxides occurs in contact with a maximum of 19%CH₄ in synthetic biogas. However, the spinel (Fe, Cr)₃O₄ may be formed at all percent methane in biogas conditions.

The presence of another spinel phase as MnCr₂O₄ is known to be much beneficial for some properties such as Cr-evaporation and oxidation. The oxide stability diagram of spinel (Mn, Cr)₃O₄ in equilibrium with AISI441 exposed to synthetic biogas at 800°C was then calculated as described in Appendix A and drawn as shown in Figure 5.12.

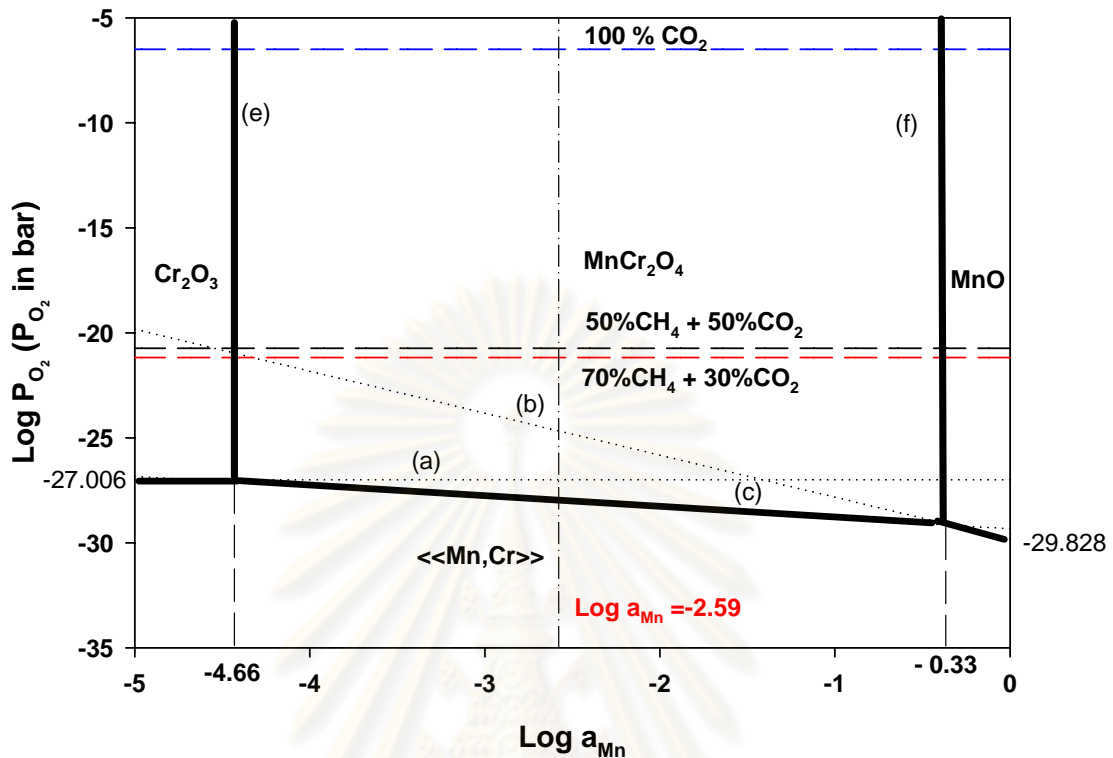


Figure 5.12: Stability diagram of MnCr_2O_4 in AISI 441 subjected to synthetic biogas at 800°C .

In this study, the calculated activity of Mn in 441 is equal to $10^{-2.59}$ at 1073 K. It is found that there is conceivable phase of MnCr_2O_4 formed in contact with biogas. Moreover, thermodynamics shows a large driving force at this contact, where it effectively appears but also a small driving force at the metal-scale interface where this compound may thermodynamically form.

5.2.3 Carbide stability of AISI441 in biogas

Considering the biogas atmospheres, not only a number of oxides can be formed on 441, but metal carbides can be also formed thermodynamically due to the presence of carbon in the system. According to the Gibbs free energy diagram of carbides, the stability of carbide in carburization increases from Fe_3C to TiC (Kofstad, 1988).

It is noted that the activity of carbon may be lower than 1 in the carbide formation at equilibrium. Figure 5.13 shows activity of carbon to form carbides with the AISI441 solution ($a_{\text{metal}} < 1$) in AISI441 in terms of activity of carbon as a function of temperature.

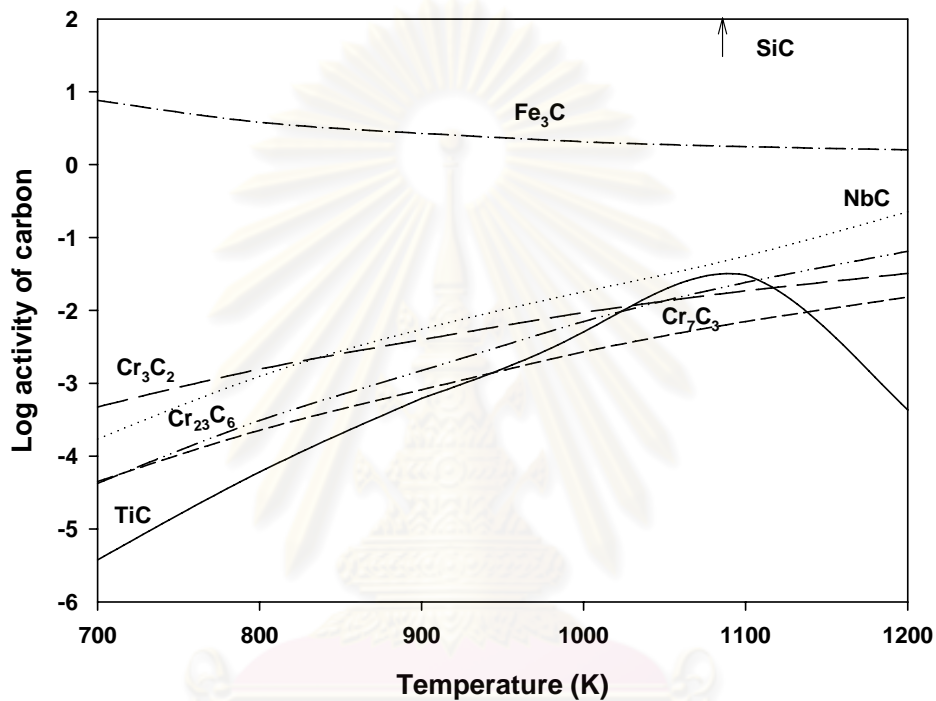


Figure 5.13: The activity of carbon to form various carbides with solid solution in AISI441 in function of temperature.

The calculation showed that the lowest activity of carbon concerns the formation of TiC at low temperatures. However, at SOFC operating temperature (600 – 1000°C) it seems that the formation of Cr_7C_3 has the lowest carbon. These activities were compared to the activity of carbon in the synthetic biogas and transformed to biogas composition in Figure 5.14. The line and dotted line in Figure 5.14 represent the boundary of carbide formation in synthetic biogas for TiC and Cr_7C_3 respectively.

It is observed that TiC and Cr_7C_3 can always be formed in the synthetic biogas composition at temperatures between 600 and 1000°C. These results therefore show

that carbide formation will be an important challenge in synthetic biogas at operating temperatures of SOFCs.

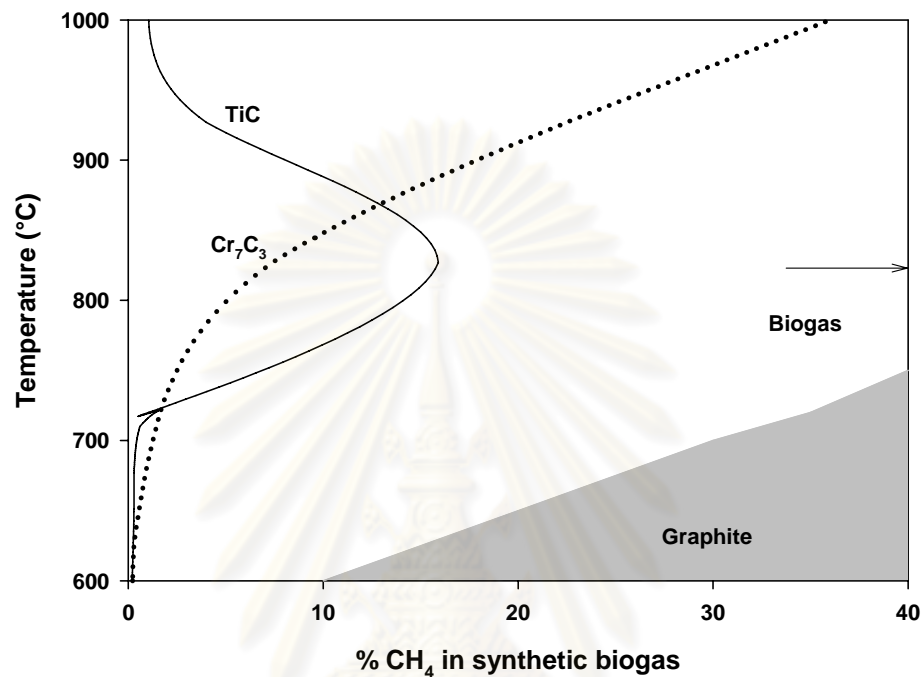


Figure 5.14: Schematic boundary of carbide formation in function of temperature and %CH₄ in synthetic biogas. Grey area represents graphite formation

5.3 Kinetics Behaviour of Ferritic Stainless Steels

5.3.1 Isothermal kinetics of corrosion

As observed by naked eye immediately after oxidation and before determining the mass change, spallation was noticed on the surfaces of samples subjected to synthetic biogas (50-70%CH₄ + 30-50%CO₂) at 900°C only and to pure methane at 800 and 900°C. In these situations, the weight gains were badly reproducible. In the other hand, at lower temperatures (700°C in methane, 700 and 800°C in biogas), no spallation was detected but all samples were covered with a thin black carbon deposit which was estimated to be negligible on the weight gain measurements. However, the

mass gain were presented with error bars indicated minimum and maximum value of 2 measurements

The corrosion kinetics of 441 at 800°C is shown in Figure 5.15. It was found that all kinetics were linear, except that in pure methane, and that increasing methane fraction in the biogas led to greater reaction rate. This was especially visible at 800 and 900°C. The mass gain obtained for samples corroded in pure CH₄ decreased apparently at 80 h due to spallation of the corrosion scale.

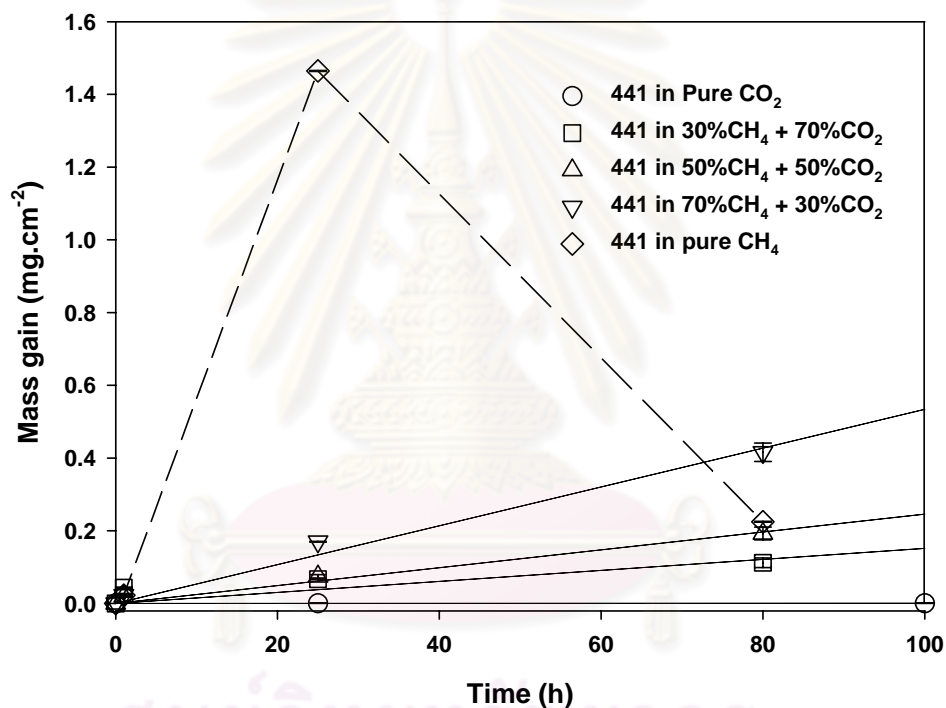


Figure 5.15: Corrosion kinetics of 441 in the different gas atmospheres at 800°C.

The kinetics of 441 in synthetic biogas at lower (700°C) and higher (900°C) temperatures in Figure 5.16 and 5.17 exhibited the same linear shape but scale spallation was always observed at 900°C, leading to weight loss. According to Figure 5.16, where no spallation was observed at 700°C, the mass gain of 441 in 70CH₄ + 30CO₂ was greater than that in pure CH₄.

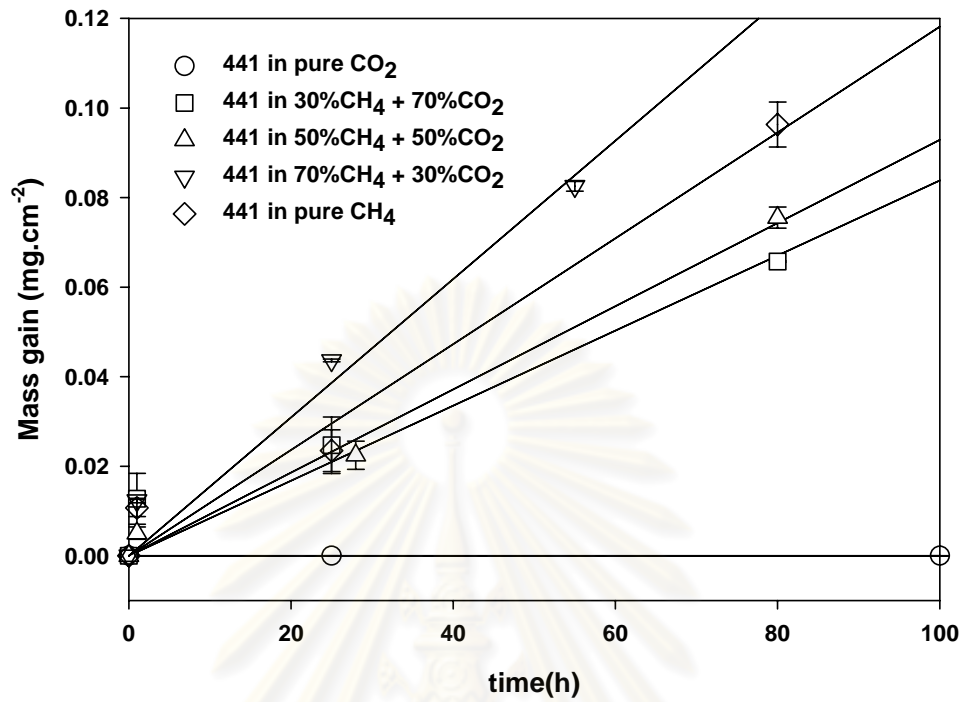


Figure 5.16: Corrosion kinetics of 441 in the different gas atmospheres at 700°C.

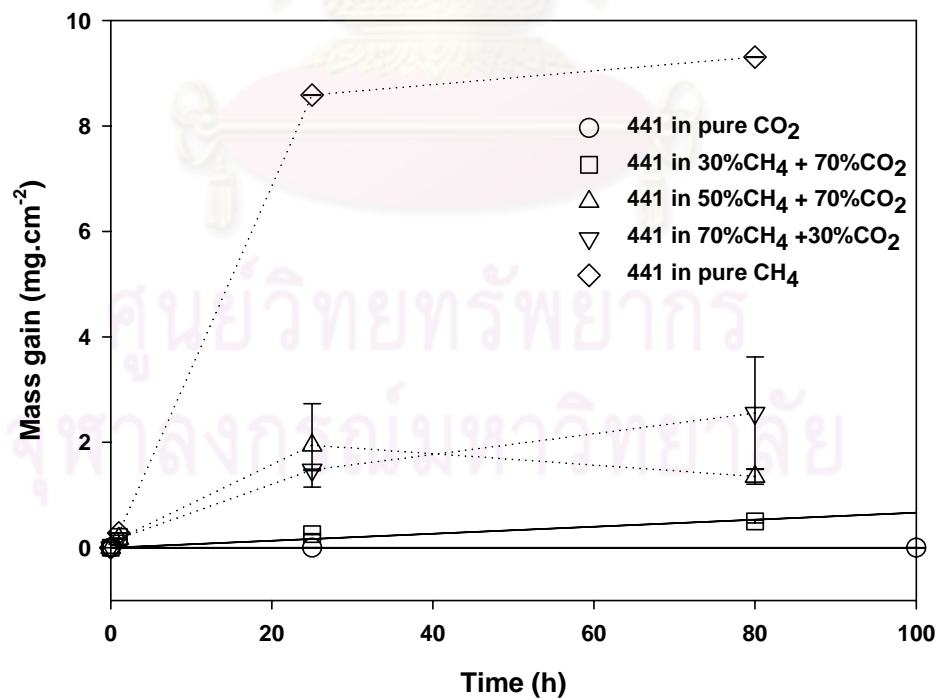


Figure 5.17: Corrosion kinetics of 441 in the different gas atmospheres at 900°C.

From Figure 5.17, the spallation was observed at 900°C when the exposure time reached to 80 hours. The kinetic constant at this temperature were estimated without consideration of mass gain for 80 hours.

The linear rate constants at several temperatures were plotted in function of the methane fraction in synthetic biogas as shown in Figure 5.18. It was found that the constant regularly increased with the methane fraction except 700°C.

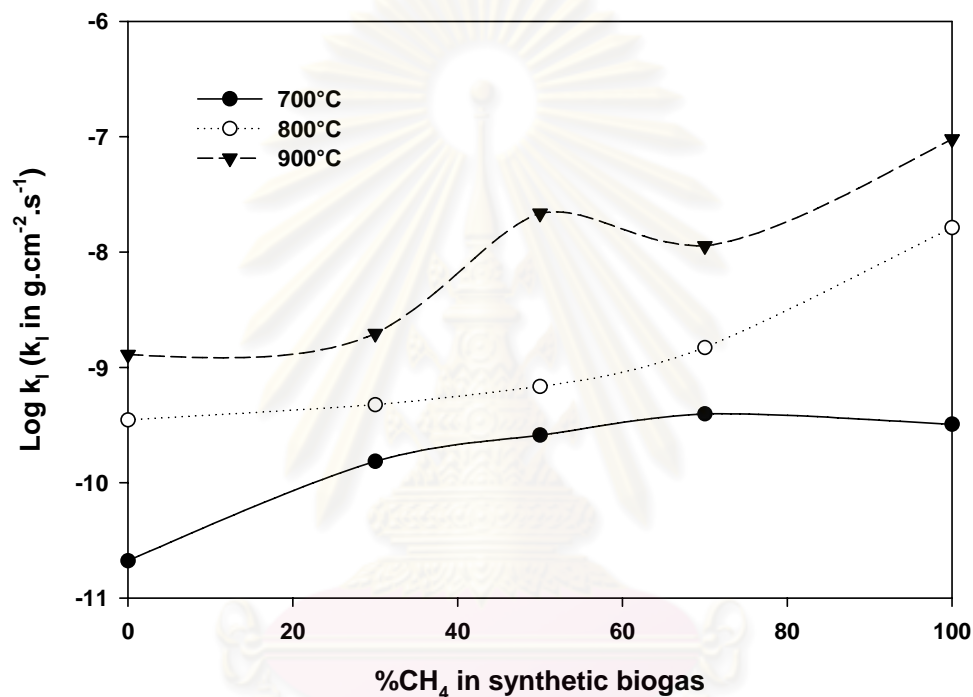


Figure 5.18: linear rate constants plotted with methane fraction in biogas at various temperatures.

All the described experiments were also carried out with Crofer as shown in Figure 5.19. It presented that the corrosion kinetics of Crofer behaved with identical manner as 441, with also larger rate value than in pure CO₂.

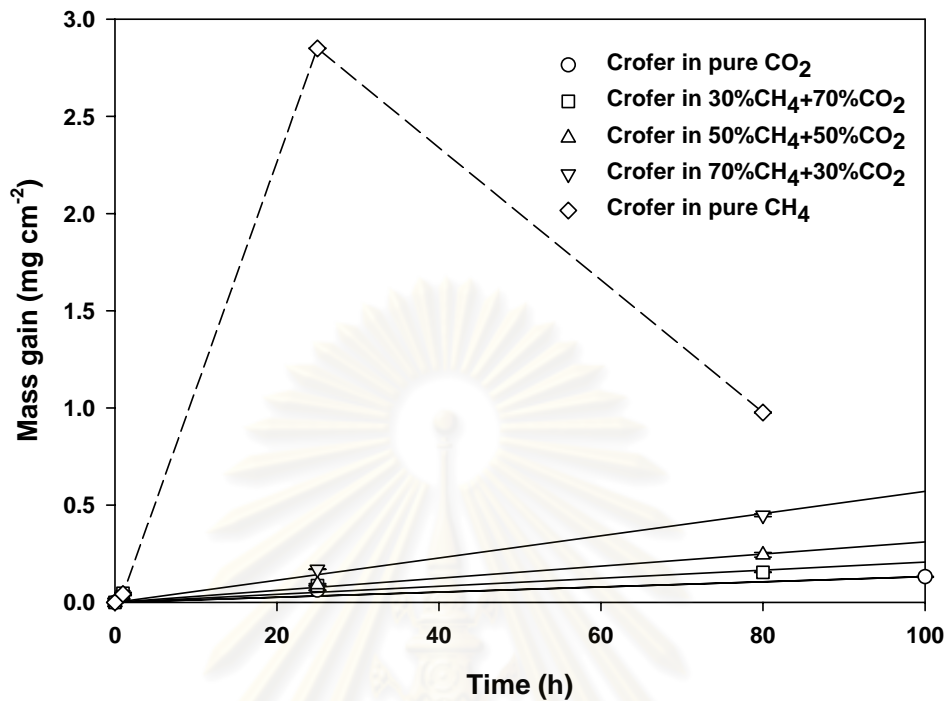


Figure 5.19: Kinetics of Crofer in the different gas atmosphere at 800°C.

5.3.2 Temperature dependence of corrosion kinetics

The comparison between the kinetic constant of 441 and Crofer in synthetic biogas is depicted in Figure 5.20. It was observed that the linear constants for 441 and Crofer subjected to the same methane fraction in synthetic biogas are also almost identical.

ศูนย์วิทยทรัพยากร
จุฬาลงกรณ์มหาวิทยาลัย

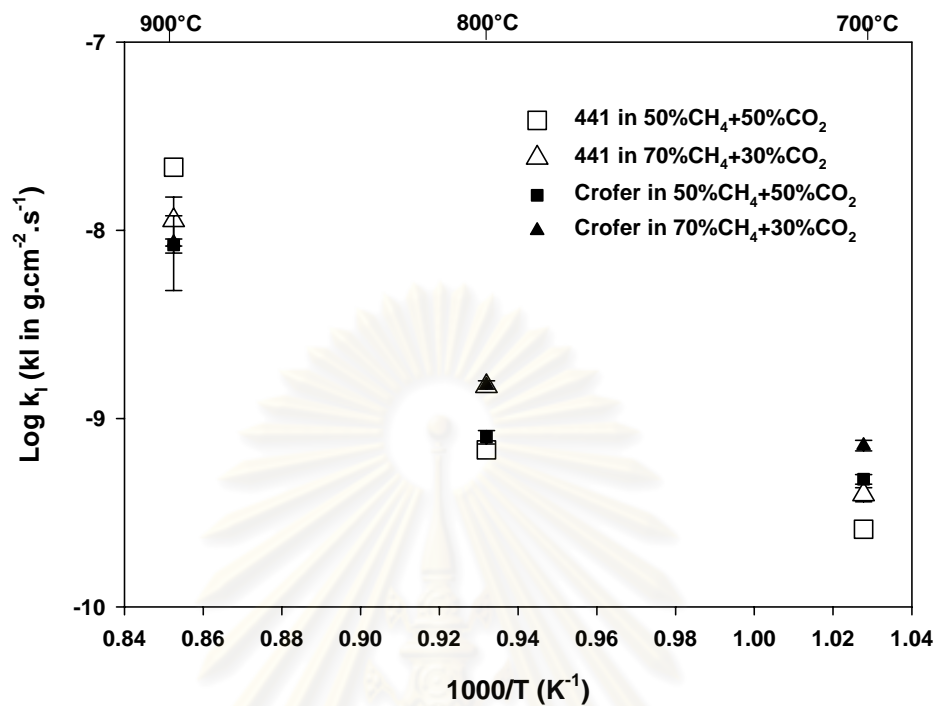


Figure 5.20: Comparison of linear constants between 441 and Crofer in synthetic biogas.

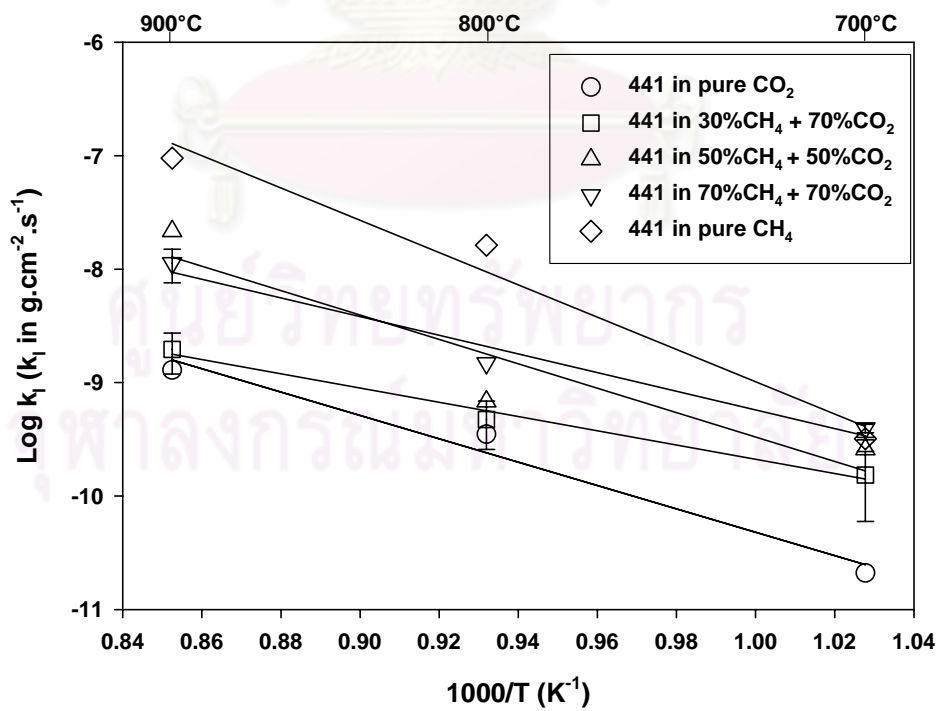


Figure 5.21: Arrhenius plot for linear kinetic constants of 441 in several atmospheres.

Comparing the kinetics in different atmospheres is shown in Figure 5.21. It was found that the linear constants of 441 in the range of biogas (50-70%CH₄) have a tendency to be greater than that of 441 in pure CO₂ at 700-900°C. The linear constants of 441 in the mixture of methane and carbon dioxide were almost equal at 700°C. The apparent activation energy of 441 obeyed by Arrhenius law with activation energy of 120, 206, 158, and 273 kJ.mol⁻¹ for 30%, 50%, 70%, and, 100% of methane in biogas consequently.

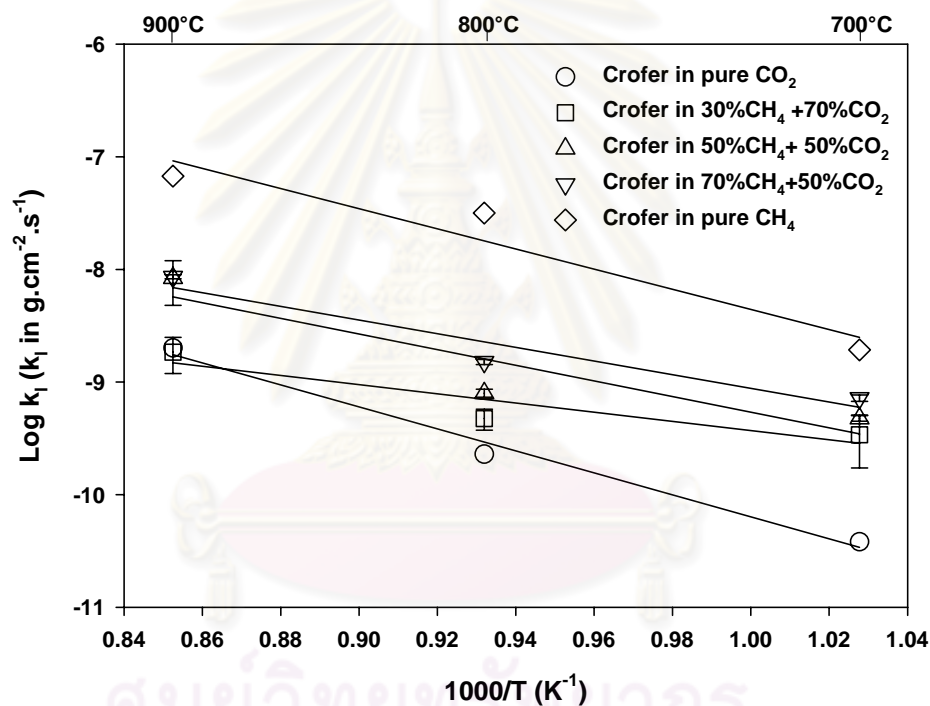


Figure 5.22: Arrhenius plot for linear kinetic constant of Crofer in several atmospheres.

For Crofer (Figure 5.22), the linear constants obey the Arrhenius law with an apparent activation energy of 78, 133, 116 and 171 kJ.mol⁻¹ for 30%, 50%, 70%, and 100% of methane in biogas, with the same tendency as 441.

To confirm these results, the corrosion kinetics of stainless steels were also performed with the thermobalance. All kinetics were also linear but it was found that the linear constants with discontinuous measurement were superior to that obtained using the thermogravimetric monitoring in the same atmospheres as presented in

Figure 5.23. The linear constant of 441 obeyed the Arrhenius laws with apparent activation energies of 182 and 144 kJ.mol⁻¹ for 50% and 70% of methane in biogas respectively.

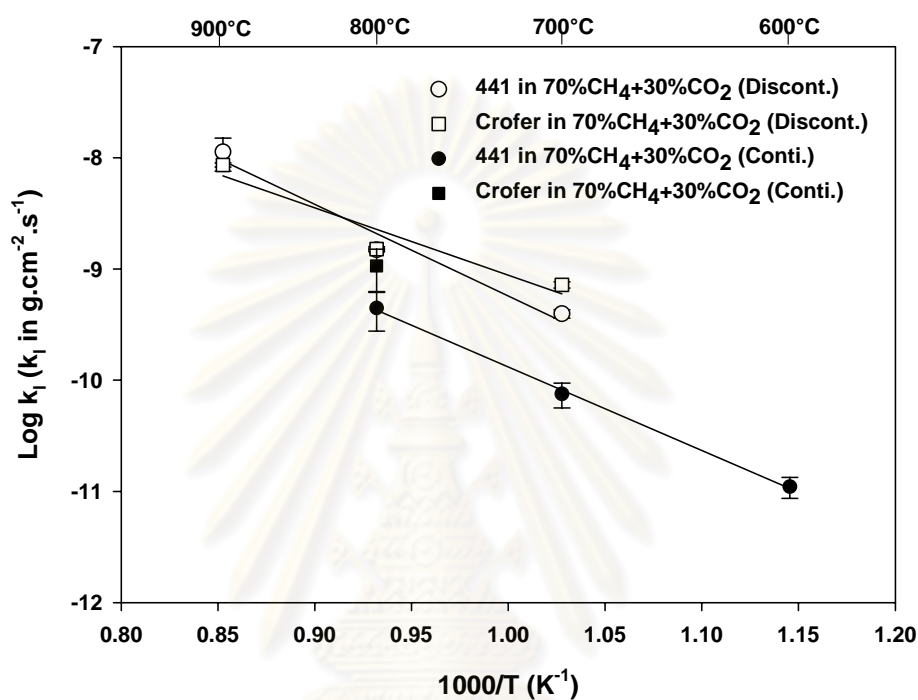


Figure 5.23: Comparison of kinetics between discontinuous measurement (discont.) and thermogravimetric monitoring (conti.).

The linear constants in pure CH₄ obtained with the thermobalance were also inferior to that obtained with the horizontal furnace (5.6 x 10⁻¹⁰ and 1.6 x 10⁻⁸ g.cm⁻².s⁻¹ for thermobalance and horizontal furnace respectively) but the constants in pure CO₂ with different methods were in the similar range (2.9 x 10⁻¹⁰, 3.9 x 10⁻¹⁰ and 3.5 x 10⁻¹⁰ g.cm⁻².s⁻¹ for microthermobalance B24, horizontal furnace, and thermobalance B70 respectively).

It can be explained as follows: 1) The temperature may be different due to different reactors (at most ±10°C). 2) The kinetics depends on the linear velocity of gas due to different velocity in each method (0.5 mm.s⁻¹ and 1 mm.s⁻¹ for microthermobalance and horizontal furnace consequently). In this study, it was noted

that the linear velocity of CH_4 affected more the kinetics than did CO_2 that may be concerned with the equilibrium of CH_4 in the reactors.

However, the linear constants of 441 and Crofer subjected to synthetic biogas (50-70% CH_4) were compared as revealed in Figure 5.24. The results showed that the constants were in the same range. Moreover, it was found that the methane fraction in biogas is not significantly influenced to the kinetic constants.

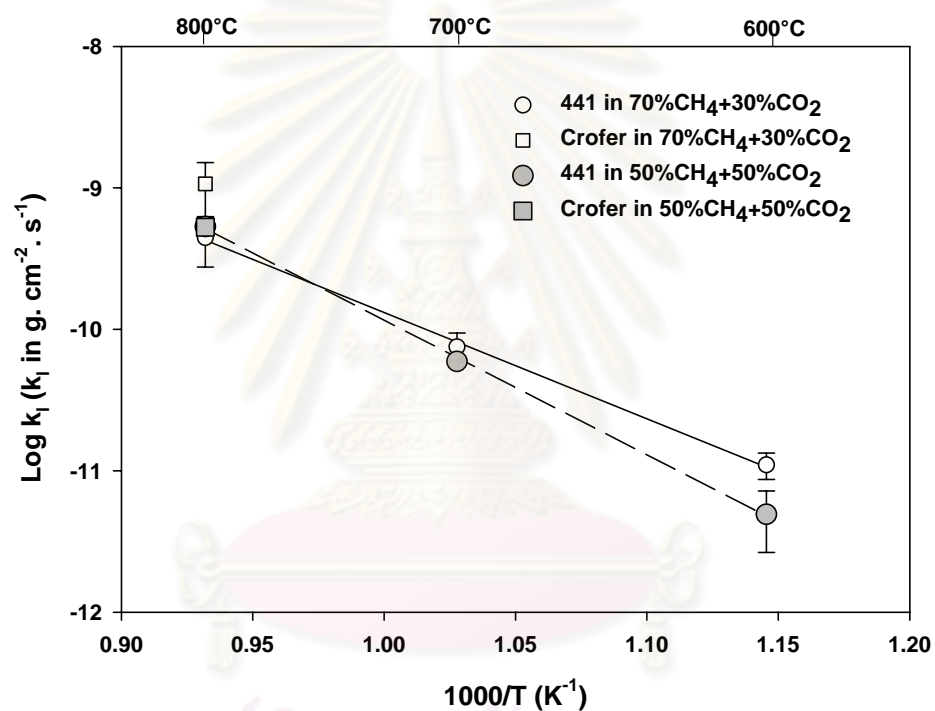
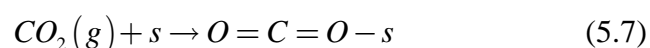
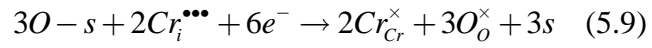
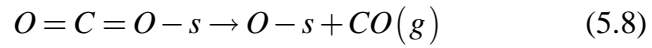


Figure 5.24: Linear constant of 441 and Crofer exposed to synthetic biogas.

The corrosion kinetics of stainless steels in biogas may be explained by mechanisms with sequence: 1) Oxidation by CO_2 and 2) Carburation by CH_4 .

As described in the chapter IV, the results showed that the oxidation kinetics of 441 was linear between 800 and 900°C due to chemical limitation at the scale – gas interface. For n-type chromia with interstitial chromium ions as a major defect, possible reaction can be reminded as follows:





These reactions led to linear kinetics depending only on CO₂ partial pressure. The model reaction rate can be recalled as follows

$$k_l = \frac{3.92 \times 10^{-12} P_{CO_2}}{1 + 8.99 \times 10^{-3} P_{CO_2}} \quad \text{g.cm}^{-2}.\text{s}^{-1} \quad (5.11)$$

where k_l is the linear constant and P_{CO_2} is the partial pressure of CO₂ in mbar

The explanation of the carburization process was accomplished by a series of experiences of 441 in pure CH₄ with the microthemobalance as depicted in Figure 5.25

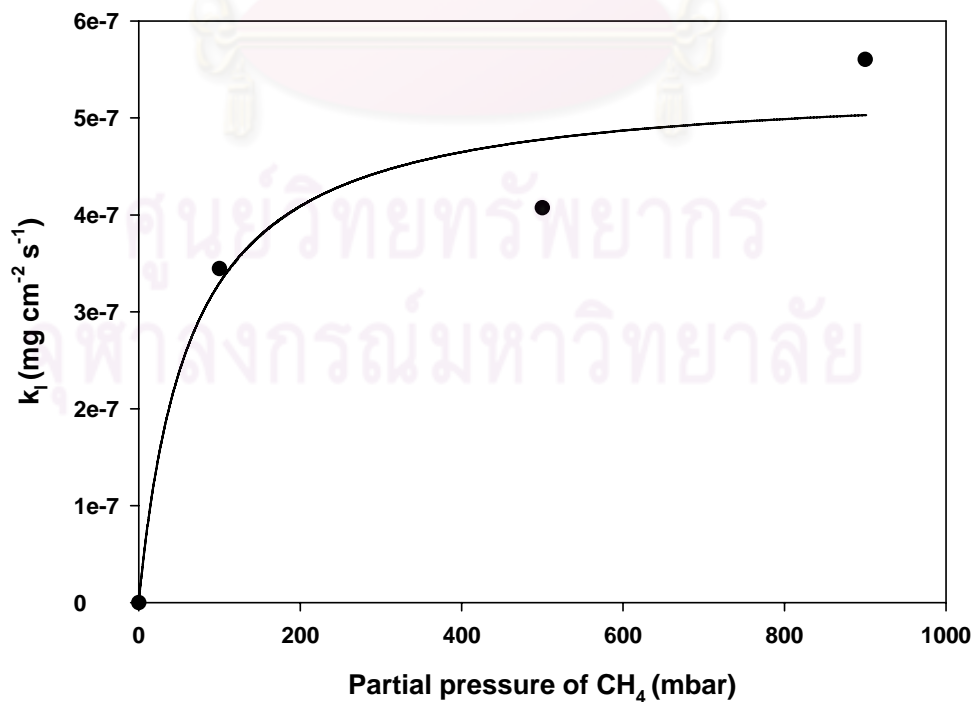


Figure 5.25: the influence of partial pressure of CH₄ on the kinetic constants of 441 at 800°C.

The constants in Figure 5.25 were correctly fit with the curve, resulting in the classical hyperbolic function following

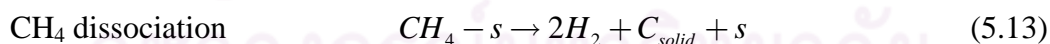
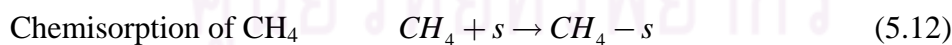
$$k_l = \frac{CP_{CH_4}}{1 + DP_{CH_4}} \quad (5.12)$$

with *C* and *D* constants values given in Table 5.1.

Table 5.1: Constants of the hyperbolic equation (5.12) by regression method

Parameter	Value	StdErr	CV(%)	Dependencies
C (mg.cm ⁻² .s ⁻¹ .mbar ⁻¹)	8.51 x 10 ⁻⁹	5.22 x 10 ⁻⁹	61.41	0.98
D (mbar⁻¹)	1.58 x 10 ⁻²	1.12 x 10 ⁻⁹	70.96	0.98

It was found that the manner of constant plot was identical to the case of 441 in CO₂ atmosphere. The feasible mechanisms can be summarized as follows



According to reaction as mention above, assuming mass gain by carbon only, the kinetic constants was proportional to the adsorption coverage ratio on the surface of the steels. The formation of carbon can be then written kinetically as

$$k_l = \frac{8.51 \times 10^{-12} P_{CH_4}}{1 + 1.58 \times 10^{-2} P_{CH_4}} \quad \text{g.cm}^{-2}.\text{s}^{-1} \quad (5.14)$$

where k_l is the linear constant and P_{CH_4} is the partial pressure of CH_4 in mbar

Due to higher gas velocity in the horizontal furnace and the same tendency of linear constant manner, the constants in the horizontal furnace were greater than those in microthermobalance in factor of 28.6. The equation (5.14) become

$$k_l = \frac{2.43 \times 10^{-10} P_{CH_4}}{1 + 1.58 \times 10^{-2} P_{CH_4}} \quad \text{g.cm}^{-2}.\text{s}^{-1} \quad (5.15)$$

The equation (5.11) and (5.15) show the linear constant depending only on the partial pressure of carbon dioxide or methane. The combination of both equations will also lead to linear function with constant partial pressure.

Comparing between equations (5.11) and (5.15), the mass gain by carbon deposit with equation (5.15) will be therefore greater than that by oxidation.

After that, carbon may then dissolve into the metal by diffusion and possibly form the carbide phases.

5.4 Scale Characterization

5.4.1 XRD analysis

X-ray diffraction analysis of 441 after exposure in different atmospheres at 800°C for 80h is shown in Figure 5.26. In order to compare the XRD pattern with particular carbide phase, the corrosion products on the sample 441 exposed to pure CH_4 atmosphere were also identified by XRD. By this situation, carbides can be detected with the major phases Cr_7C_3 (ICDD card 36-1482) or Cr_3C_2 (ICDD card 35-0804). Practically, the chromia phase was unexpectedly observed in the plane [012] ($2\theta = 24.5^\circ$, ICDD card 38-1479).

The spectra recorded on samples corroded in biogas were surprisingly very similar to those recorded on samples oxidised in pure CO₂, as detailed in chapter IV, with the major phases Cr₂O₃ and (Mn,Cr)₃O₄. The presence of eventual carbides is difficult to assess due to many line overlapping. Possible carbide(s) can be observed as a shoulder of the [100] line of the ferritic phase, corresponding to the most intense lines of Cr₇C₃ ([151] line at $2\theta = 44.167^\circ$, ICDD card 36-1482) or Cr₂₃C₆ ([511] line at $2\theta = 44.097^\circ$, ICDD card 35-0783). An extra line, corresponding to none of the above compounds also appears at $2\theta = 40.9^\circ$, possibly indexed as the intense [200] reflexion of Cr₃C₂ (ICDD card 35-0804), but it must be noted that the most intense line of this phase is always absent from the spectra.

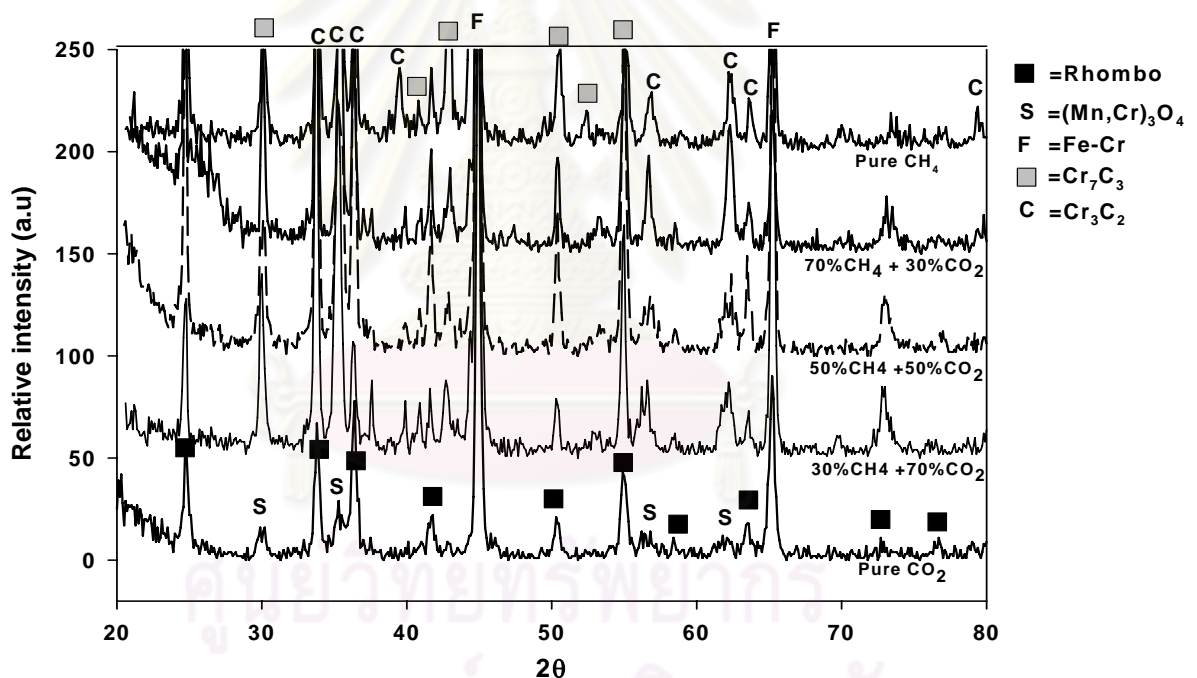


Figure 5.26: X-ray diffraction of 441 in different gas at 800°C for 80h.

Figure 5.27 exhibits the XRD spectra recorded on sample 441 corroded for different oxidation time. It was observed that the spectrum was similar pattern with the chromia phase, spinel phase and Cr₇C₃ phase. The amount of phases also increased with increased oxidation time.

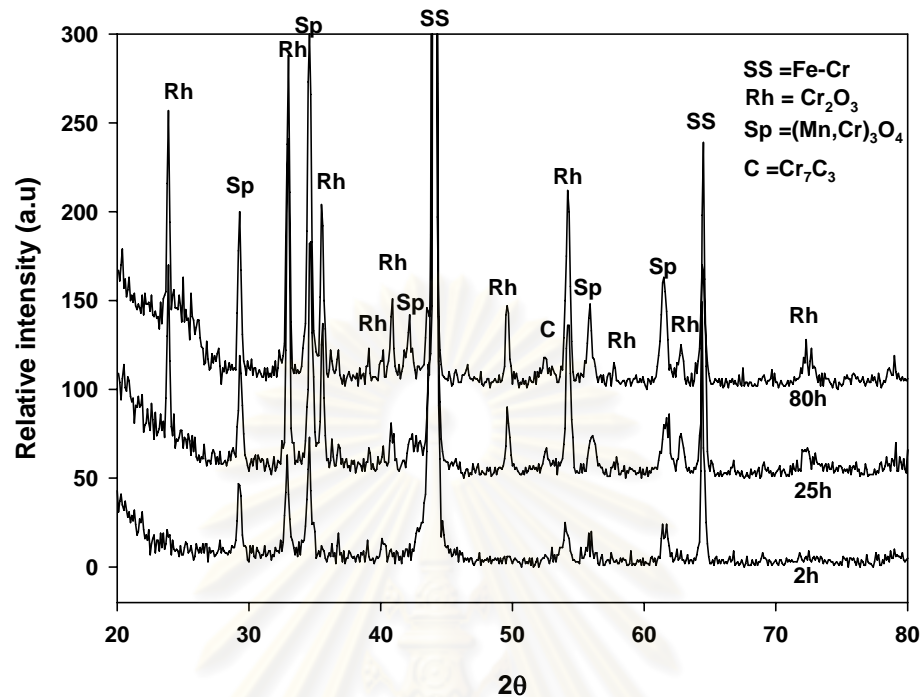


Figure 5.27 X-ray diffraction of 441 in 70%CH₄+30%CO₂ for different oxidation periods at 800°C.

Comparing the XRD pattern of Crofer to that of 441 in the same condition, Figure 5.28 shows that the spectra were similar, indicating the major phase of Cr₂O₃ and MnCr₂O₄ in addition of carbide. This observation was identical to the other temperature for ferritic stainless steels exposed to biogas.

ศูนย์วิทยทรัพยากร
 จุฬาลงกรณ์มหาวิทยาลัย

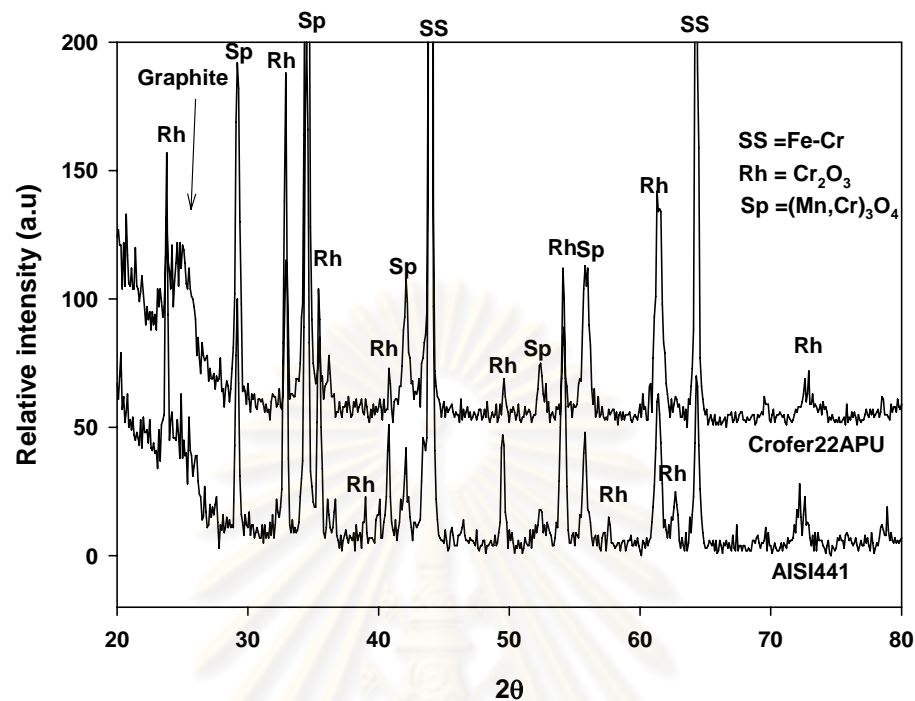
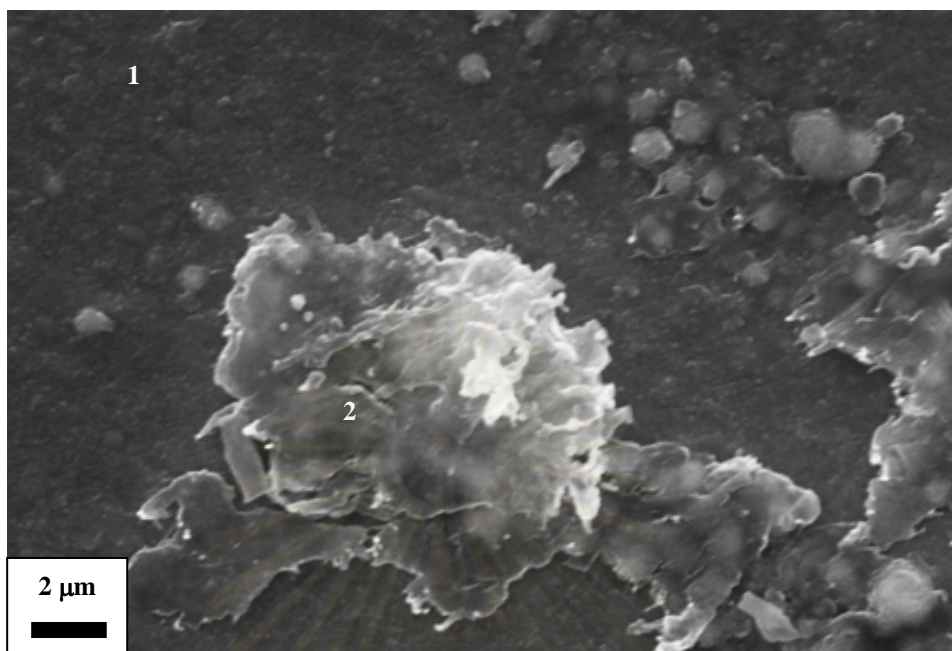


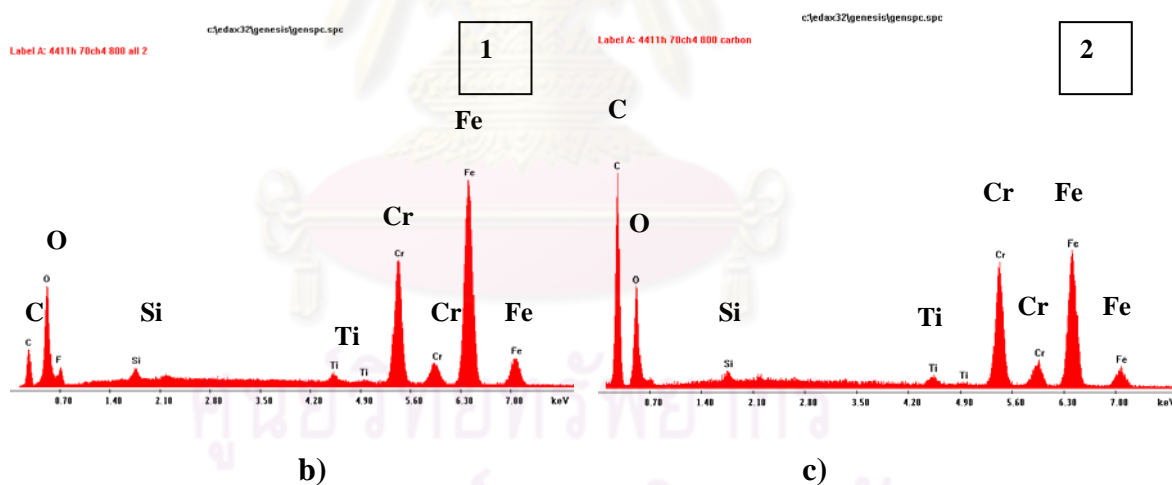
Figure 5.28 X-ray diffraction of ferritic stainless steels in 70%CH₄+30%CO₂ for 80h at 800°C.

5.4.2 Scale morphology

The surface morphology of 441 corroded in synthetic biogas atmosphere during 2 hours is shown in Figure 5.29. It was observed that carbon (designated as 2 in the figure) can be deposited with different size on the Cr oxide scale (1).



a)



b)

c)

Figure 5.29: SEM and EDX analysis of 441 exposed to 70%CH₄+30%CO₂ during 2 hours a) Surface morphology b) EDX for oxide scale and c) EDX for carbon or graphite.

When the corrosion advanced, the surface morphology of 441 exposed to 70%CH₄+30%CO₂ at 800°C during 80 h is shown in Figure 5.30. It was found that more carbon particles were deposited on the scale surface. Oxide platelets were

observed between carbon particles. It seemed that the homogeneous carbon particles were accumulated on the surface more than that during 2 hours.

On the cross section (Figure 5.31), the scale appears as a dense phase with quite uniform thickness, between 4 and 5 μm . Some small nodules analyzed as detected in C-rich can be observed in the oxide layer with 0.5 μm in diameter.

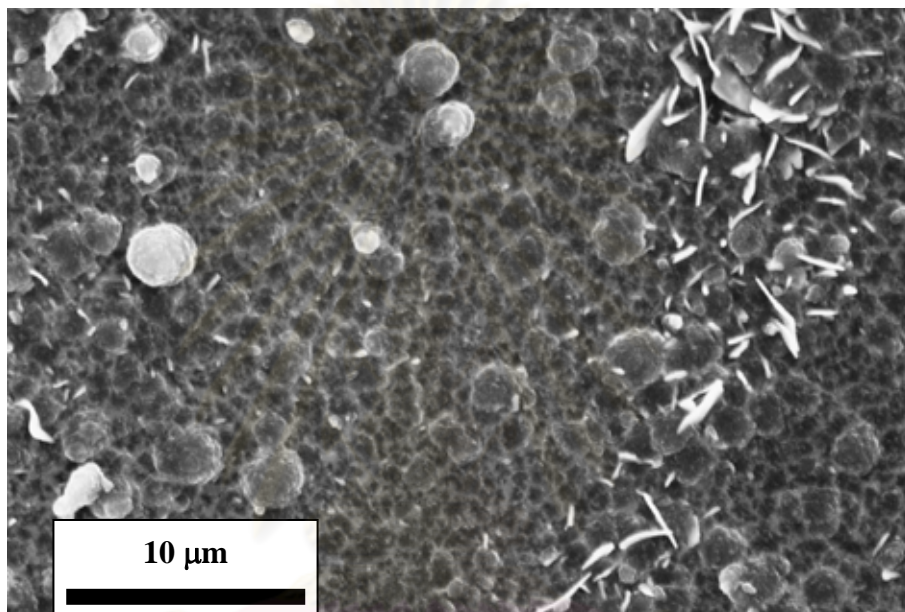


Figure 5.30: Surface morphology of 441 exposed to 70%CH₄+30%CO₂ at 800°C during 80h.

ศูนย์วิทยทรัพยากร
จุฬาลงกรณ์มหาวิทยาลัย

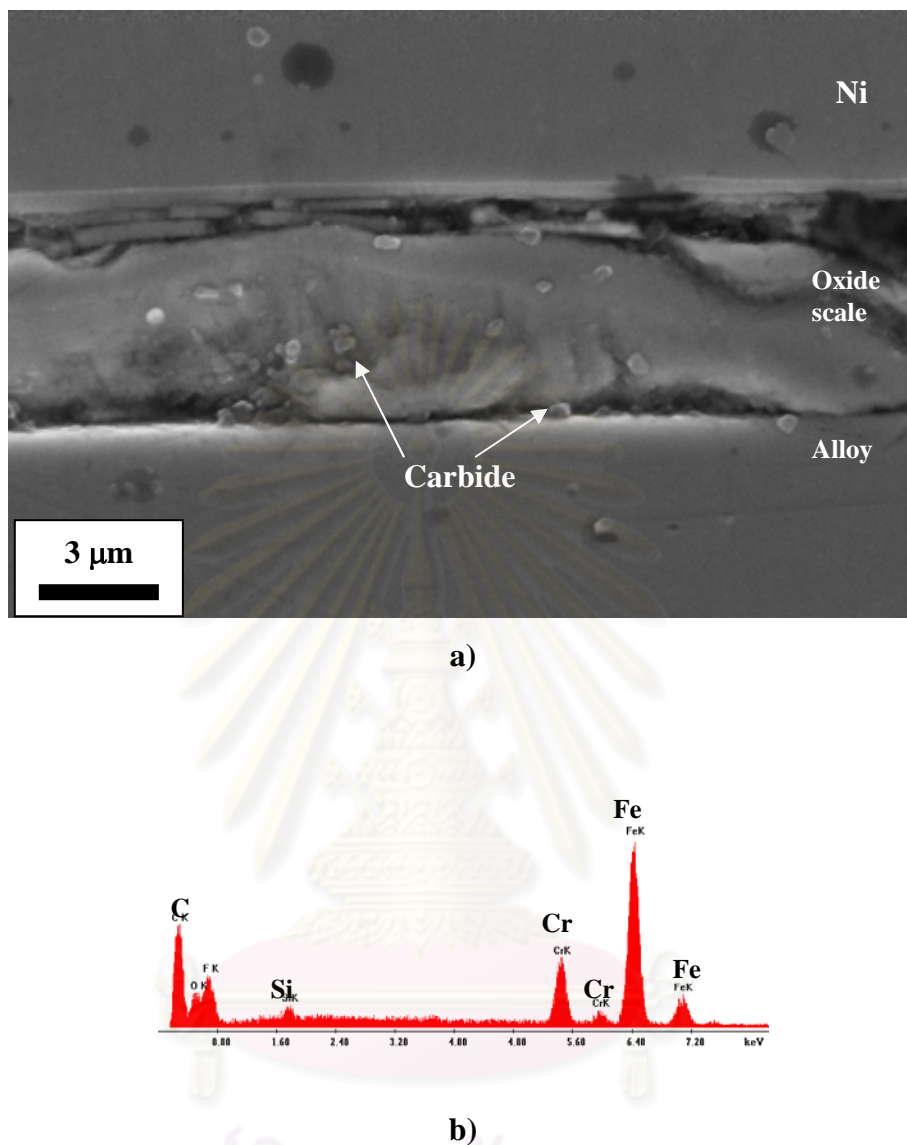


Figure 5.31: Cross section of 441 exposed to 70%CH₄+30%CO₂ at 800°C during 80h
 a) Morphology of corrosion scale and b) EDX analysis for carbides.

The morphology of the corrosion scale formed in the biogas (50%CH₄+50%CO₂) is presented in Figure 5.32 for surface and Figure 5.33 for cross section. Whiskers, platelets and fleecy forms of chromia were visibly observed on the dense chromia scale in addition to carbon particles. Spherical carbon particles tend to sit near the chromia whiskers with an average size of 4 μm. Small nodules rich in Ti were also detected on the surface, a typical observation for such ferritic stainless steels.

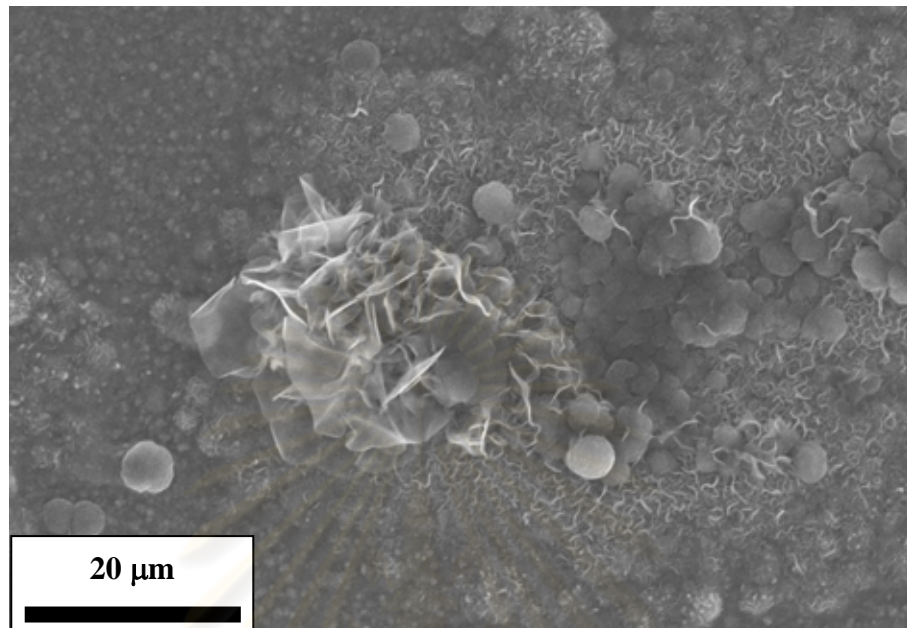


Figure 5.32: Surface morphology of 441 exposed to 50%CH₄+30%CO₂ at 800°C during 80h.

The cross section in Figure 5.33 shows that the scale is dense with non uniform thickness. Isolated voids can be observed within the scales, often filled with possible Cr carbide, as detected by EDS (designated as 1 in figure). Carbon deposit is also observed on top of the oxide scale.

ศูนย์วิทยทรัพยากร
จุฬาลงกรณ์มหาวิทยาลัย

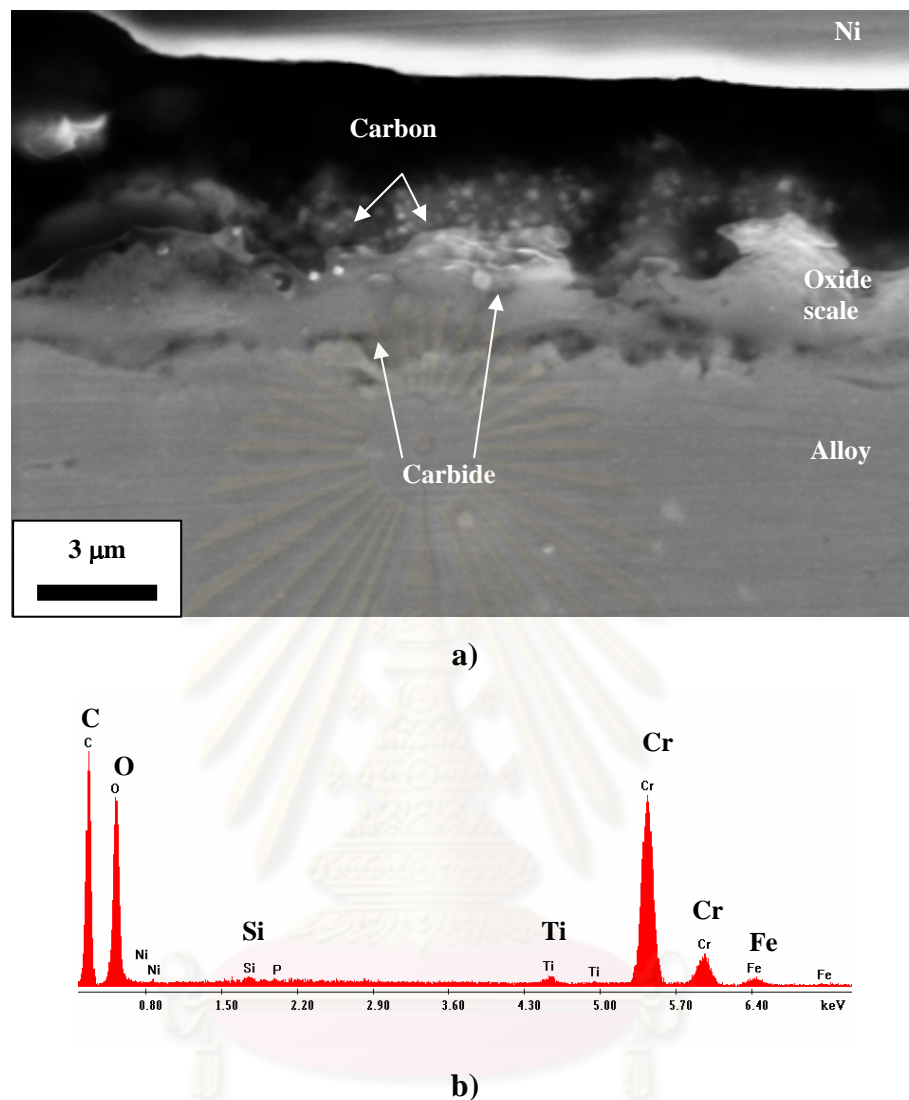


Figure 5.33: Cross section of 441 exposed to 50%CH₄+50%CO₂ at 800°C during 80h
 a) Morphology of corrosion scale and b) EDX analysis for carbides.

The morphology of the corrosion scales obtained at higher temperature (900°C) for 441 exposed to 70%CH₄+30%CO₂ during 80 h appears in Figure 5.34 for surface and in Figure 5.35 for cross section. From Figure 5.34, the porous state of the scale was evidenced, with carbon within pores. Surface was rather rough comparing with the surface of samples exposed to the same atmosphere, but at lower temperatures. Discontinuous pores or voids occurred within the scale (Figure 5.35). Such scales seemed poorly adherent due to the presence of large voids at the metal-scale interface, in good agreement with the observed spallation. On all samples, a

thick carbon deposit was grown during the corrosion sequence and easily detached at cooling. Figure 5.36 shows such a deposit, containing only graphite as characterized in Figure 5.37, on the samples subjected to synthetic biogas at 900°C with characteristic growth features.

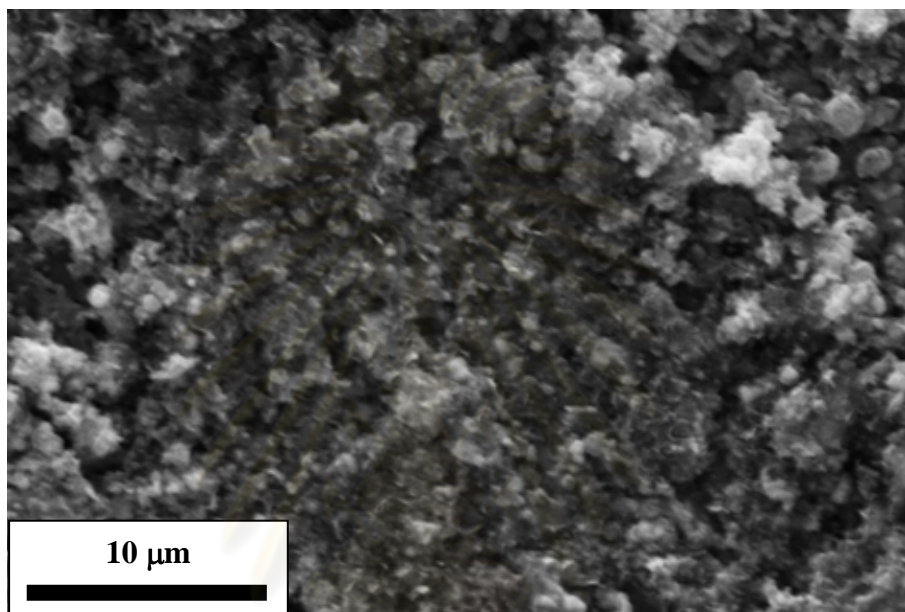


Figure 5.34: Surface morphology of 441 exposed to 70%CH₄+30%CO₂ at 900°C during 80h.

ศูนย์วิทยทรัพยากร
จุฬาลงกรณ์มหาวิทยาลัย

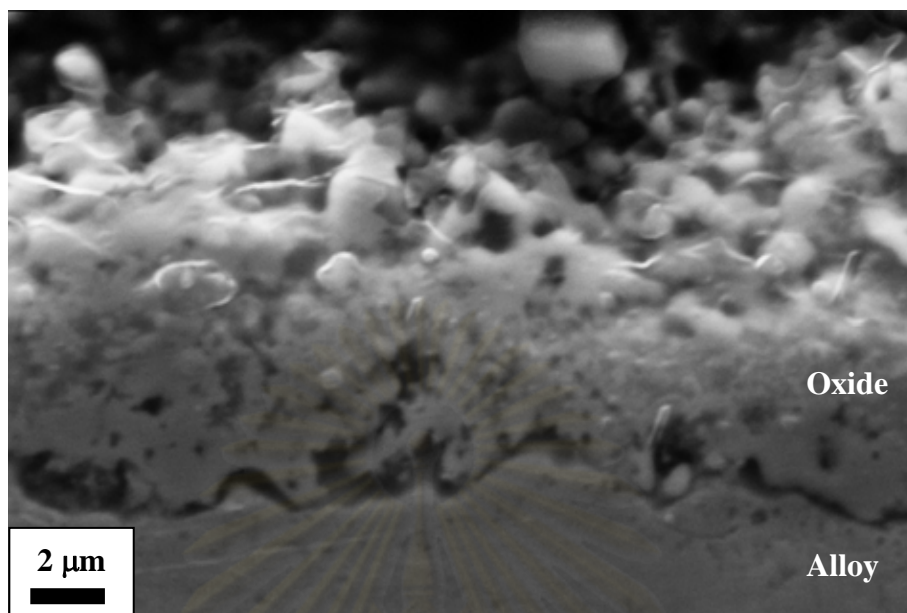


Figure 5.35: Cross section 441 exposed to 70%CH₄+30%CO₂ at 900°C during 80h.

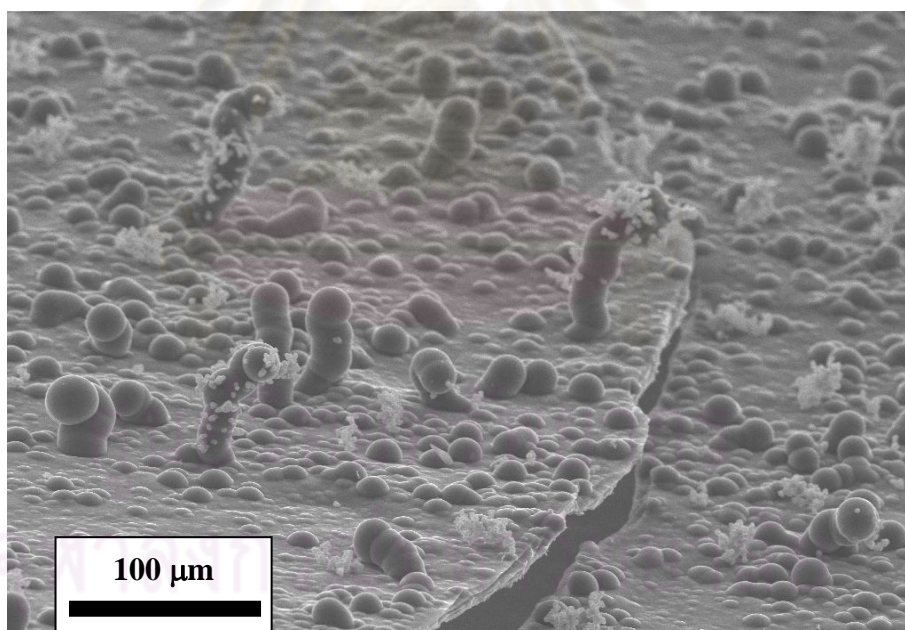


Figure 5.36: Carbon deposit on the sample exposed to 70%CH₄+30%CO₂ at 900°C during 25h.

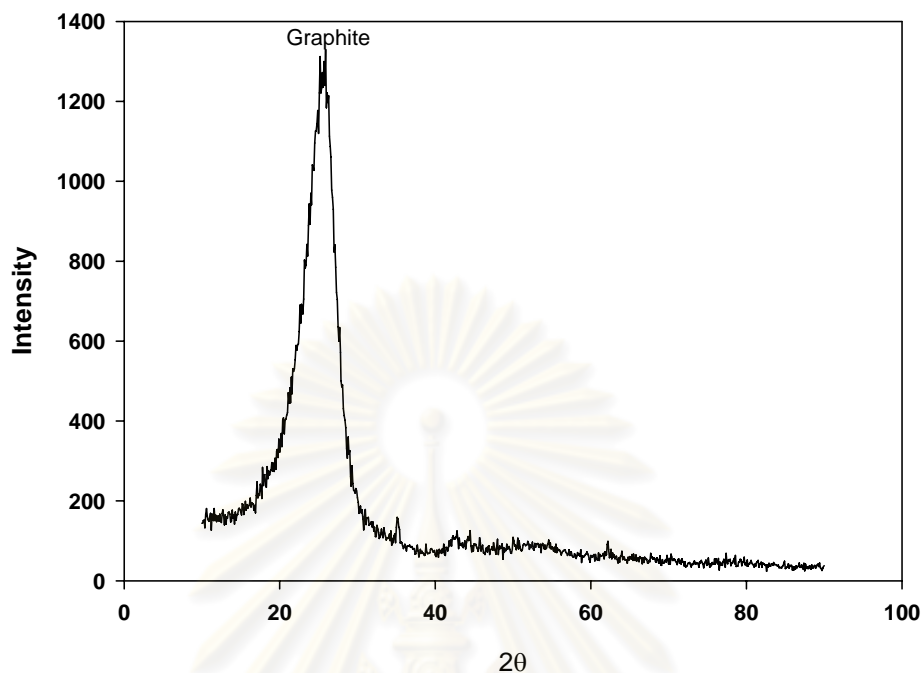


Figure 5.37: XRD pattern of carbon deposit of figure 5.36.

From Figure 5.36 and 5.37, graphite particles of 10 μm diameter deposited and transformed into the film. It seemed that the carbon has grown in the perpendicular direction of the surface sample. The growth rate of graphite film is approximate $0.11 \mu\text{m}\cdot\text{s}^{-1}$. In addition, XRD spectra recorded on the deposit confirmed that there was only graphite in the deposit.

Comparing to scale morphology of Crofer in the same condition, the surface morphology of Crofer exposed to biogas was also revealed in figure 5.38 for Crofer at 800°C and in figure 5.39 for that at 900°C . It seemed their morphology were almost identical to the morphology of 441 in the same condition at 800°C but the scale morphology of Crofer exposed to biogas at 900°C seemed more dense than that of 441. From Figure 5.36, whiskers, platelets and fleecy forms of chromia can be also observed on the dense chromia scale in addition to carbon particles.

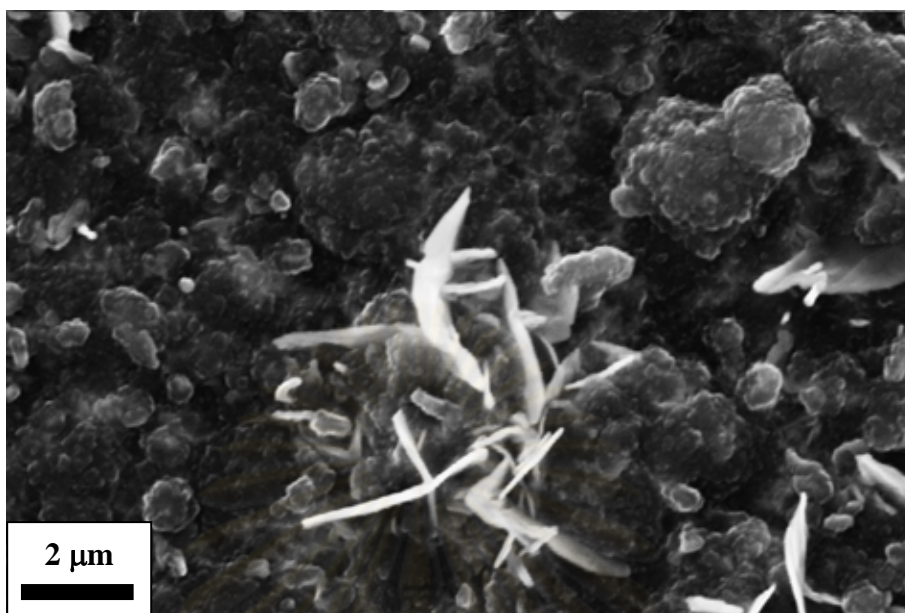


Figure 5.38: Surface morphology of Crofer exposed to 70%CH₄+30%CO₂ at 800°C during 80h.

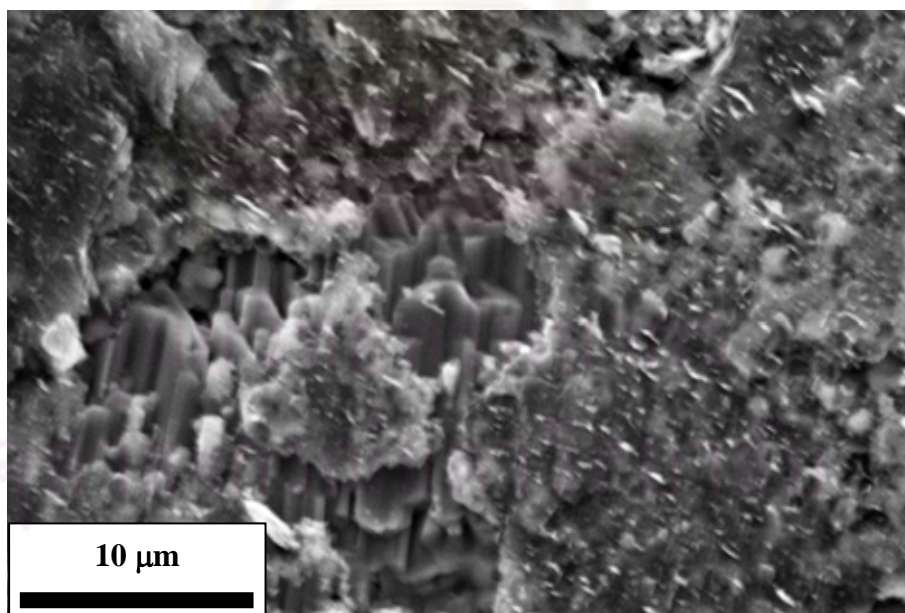


Figure 5.39: Surface morphology of Crofer exposed to 70%CH₄+30%CO₂ at 900°C during 80h.

The morphology of corrosion scale showing chromia and/or carbide-rich phase is in agreement with thermodynamic calculations and generally observed in stainless steels. From above results and discussion, it may be further proposed that, in the initial stage of corrosion, the major oxide was mainly rhombohedral $(\text{Fe, Cr})_2\text{O}_3$ topped with MnCr_2O_4 , SiO_2 , TiO_2 and carbon. When the corrosion proceeds, the corrosion scale becomes more dense and homogeneous in addition to spherical carbon particles at lower temperature. Mn-Cr Spinel tended to be dense and covered Cr_2O_3 . TiO_2 was also dispersed on the outermost layer. The schematic sketch of the evolution of the corrosion scale growth at the lower temperature is schematized in Figure 5.40.

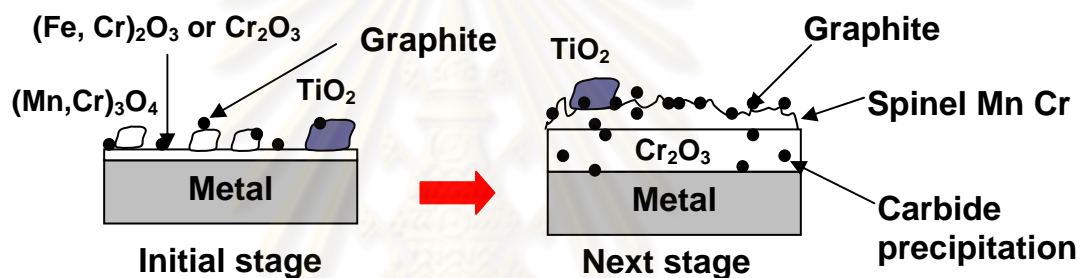


Figure 5.40: Schematic of the evolution of corrosion scale of 441 in biogas atmosphere at the lower temperatures.

However, due to more carbon pick up at higher temperatures, the oxide scale becomes porous with carbon and carbon then diffuses easier compared to lower temperatures to metal to form carbide. The schematic sketch of the evolution of the corrosion scale growth at 900°C is schematized in Figure 5.41.

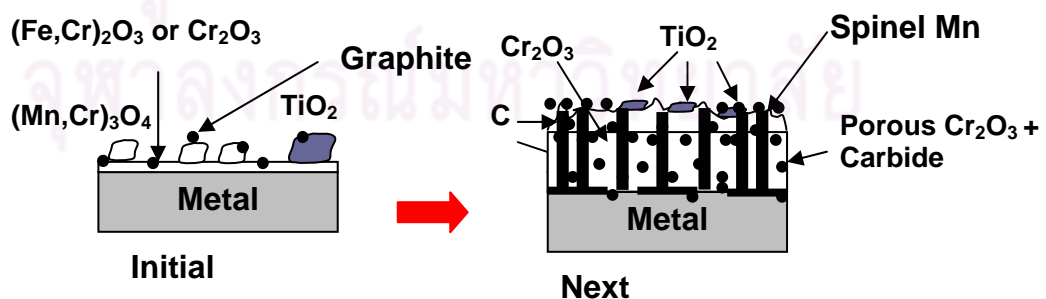


Figure 5.41: Schematic of the evolution of the corrosion scale on 441 in biogas atmosphere at 900°C .

5.4.3 Thickness

Due to the presence of carbon and possible carbide(s) in addition to oxides, the thickness of the corrosion scales is difficult to assess exactly due to non-uniform thickness and the appearance of internal precipitation. They were tentatively measured by SEM on cross-sections and also calculated from mass gain, assuming chromia formation only (as described in Appendix B). The results appear in Figure 5.42. It can be observed that scales grown in pure CO₂ have almost identical measured and calculated thickness. On the contrary, when grown in biogas, the calculated and measured thicknesses could be different by a factor of 2. Thicknesses of scales on 441 in synthetic biogas are significantly greater than those in synthetic air or humidified hydrogen. The scale thickness on 441 is higher than Crofer for all atmospheres except for air and H₂O/H₂.

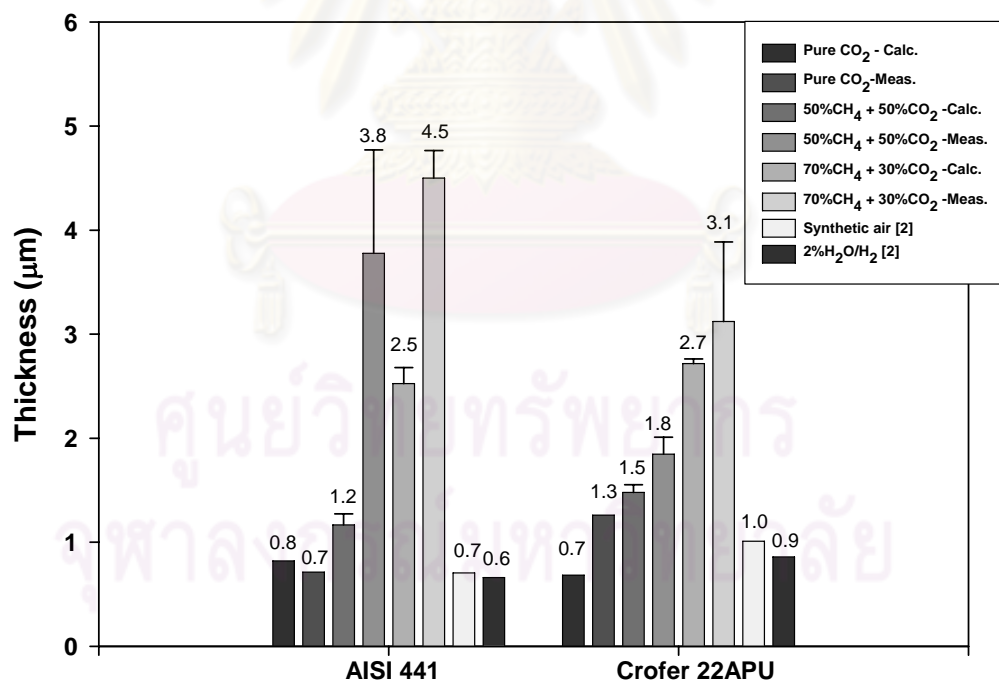


Figure 5.42: Thickness of corrosion scales formed in different atmospheres at 800°C obtained by calculation from mass gain (Calc.) and cross section measurements (Meas.). When error bars, the value indicated is the mean value.

5.4.4 Microhardness

To assess the presence of carbon within the metallic substrate, microhardness testing was performed in the subsurface zone. The results of Knoop indentation, with the long diagonal of the indent parallel to the metal-scale interface, at 10 μm below it appear in Fig. 5.43. The hardness of 441 subjected to synthetic biogas at 800°C is not significantly different from that of non-oxidised 411, showing that, at this temperature, carburisation is very weak, in good agreement with the XRD results. In the other hand, the hardness of 441 submitted to synthetic biogas at 900°C gained much higher value compared to the similar atmosphere at 800°C due to carbon dissolution and/or precipitation hardening by carbide.

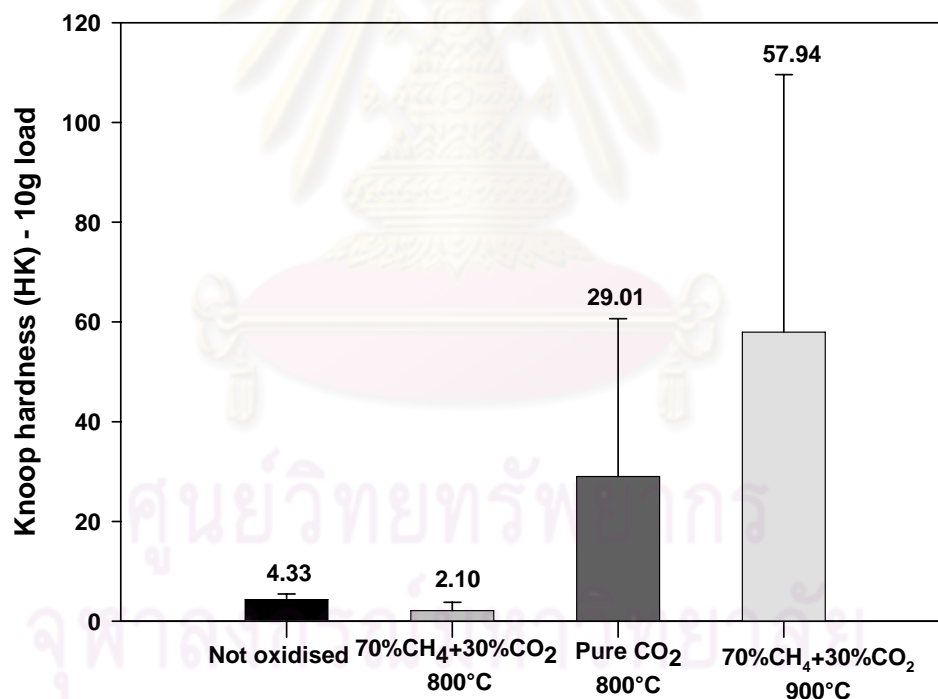
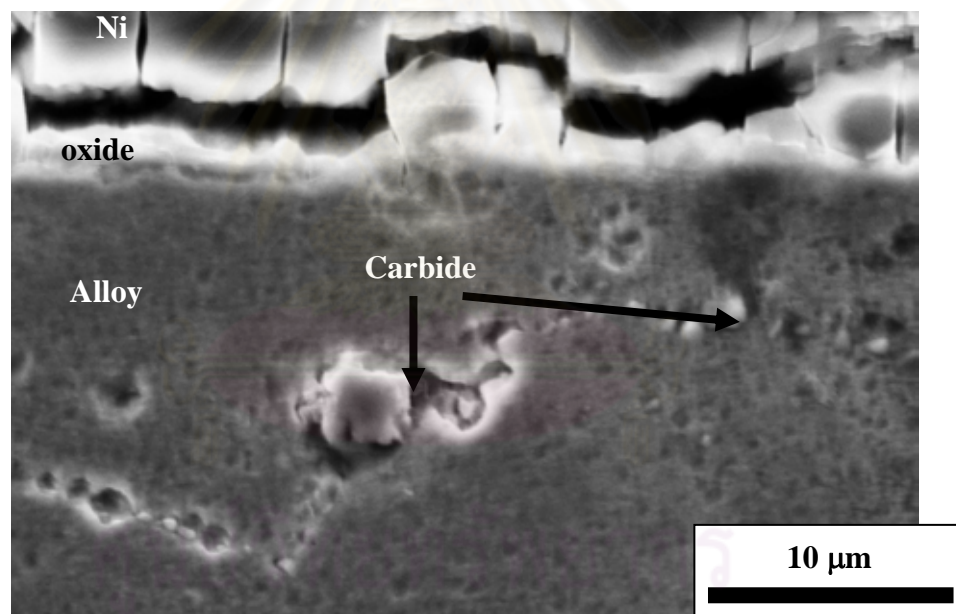


Figure 5.43: Microhardness values of the 441 steel substrate at 10 μm under the metal-scale interface. Corrosion duration: 80 h. Given values: mean values. Error bars: maximum values from 5 measurements.

In pure CO₂, the high hardness value obtained confirms the works by Abellan et al. (Abellan, 2009; 2010) who claim that carbon may diffuse through chromia

scales. According to thermodynamics, the equilibrium activity of carbon in pure CO₂ is not high enough to carburize chromium, but CO release at the oxide-gas interface, resulting from the oxidation reaction, may locally increase this activity making possible chromium carbide formation. It is also envisaged that CO may diffuse in molecular form through specific channels in the oxide, making carbon dissolution and carburisation possible at the metal-scale interface by this reaction: $2CO = CO_2 + \langle\langle C \rangle\rangle_{metal}$. In this study, carbide precipitation in alloy was confirmed by SEM imaging of the cross section of 441 in pure CO₂ as shown in Figure 5.44.

From this figure, it is noted that the precipitates are favorably TiC with 4 μm in diameter at about 10 μm from the metal - oxide interface.



a)

จุฬาลงกรณ์มหาวิทยาลัย

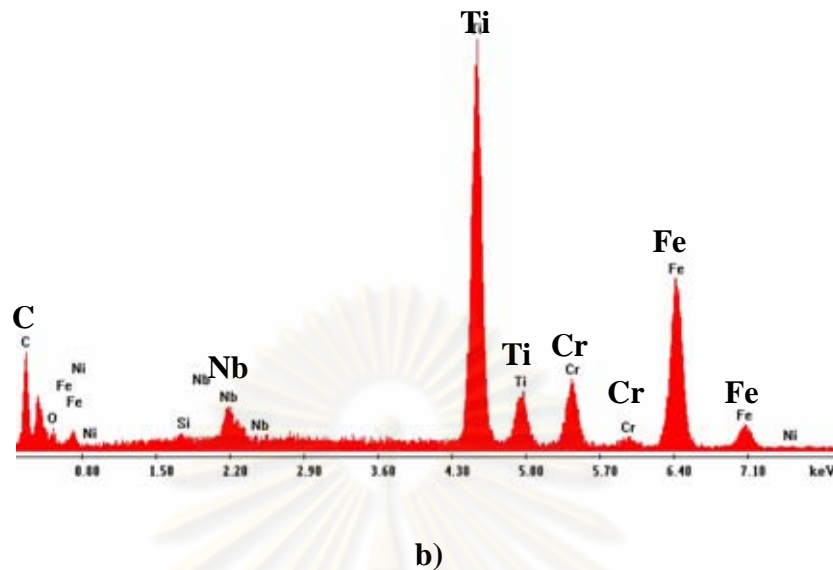


Figure 5.44: a) cross section of 441 subjected to pure CO₂ at 800°C during 100h and b) EDX analysis for carbides.

According to morphology and microhardness results, the oxide and/or carbide layer that forms on the surface at lower temperatures can act as a barrier to inward carbon diffusion into surface corresponding in lower hardness at the metal-scale interface, whereas the porous scale formed at 900°C may favour the carbon diffusion resulting in embrittlement of the bulk materials.

The corrosion behaviour of stainless steels in synthetic biogas atmospheres were studied and concluded as follows:

1. Oxidation kinetics of the steel in synthetic biogas are linear, with the rate constants higher than for steel oxidation in pure CO₂.
2. Increasing the fraction of CH₄ in biogas increases the corrosion rate.
3. The oxides Cr₂O₃ and Mn-Cr spinel form on 441 in biogas as in CO₂, but Cr and Ti carbides can also appear in the scale and/or in the metal.
4. At $T \leq 800^\circ\text{C}$, the scale is compact and acts as a barrier to carbon penetration, but at 900°C porosity in scales leads to direct reaction between biogas and metal.
5. Carbon strongly deposits on samples exposed to synthetic biogas at 900°C but not at lower temperatures. The temperature of 800°C must not be overpassed to ensure carbon free operation of SOFCs.

Chapter VI

General conclusion and perspectives

6.1 General Conclusion

The conventional stainless steels AISI441 was used as the candidate materials for SOFCs interconnectors at high temperature. The important properties for these with comments are corrosion behaviour, mechanical adhesion of scale, electrical conductivity, and Cr-evaporation. Anyway, this research was intensively focused on the terms of high temperature corrosion behaviour of ferritic stainless steels under fermentative biogas atmospheres instead of humid hydrogen.

The study divided into the following two categories: 1) the oxidation behaviour of steels under CO₂ atmosphere and 2) the corrosion behaviour of steels subjected to synthetic biogas atmospheres. They were summarized as follows:

6.1.1 Conclusions for steels under CO₂ atmosphere

AISI441 and Crofer22APU were oxidized in pure CO₂ at high temperatures in order to understand the oxidation kinetics. The study of oxidation kinetics associated with the thermodynamics, and physico-chemical characterization was carried out. The following conclusions could be drawn:

1. In the temperature range of 600 to 1000°C, the thermodynamic calculation showed that the partial pressures of oxygen are in order of 10^{-8.4} to 10^{-4.9} bar, corresponding to the stability binary oxides as FeO, Cr₂O₃, SiO₂, TiO₂, Nb₂O₅ and also the spinel phase MnCr₂O₄. The carbon activity varied from 10^{-13.9} to 10^{-11.5}, showing that no solid carbon or stable carbide can be deposited.

2. The oxidation kinetics of ferritic stainless steel under CO₂ atmosphere was in parabolic function at high temperatures (>925 °C) due to limitation by chromium diffusion through the growing oxide scale and in linear function at lower temperatures and initial oxidation stages due to interface limitation. It was also noted that the mass gain at all temperatures increased very rapidly at the initial stage (20 min) to about 0.03-0.05 mg.cm⁻² due to rapid nucleation of oxide.

3. Both kinetic constants (parabolic and linear) of 441 under CO₂ atmosphere were almost identical to these of Crofer as well as both apparent activation energies in the same conditions.

4. The parabolic constants of ferritic stainless steels in CO₂ were in order of 10⁻¹² g².cm⁻⁴.s⁻¹, in the same range as those in synthetic air or 20%O₂/Ar. However, their apparent activation energy was considerably higher than the values obtained in other atmospheres.

5. The linear constants of ferritic stainless steels oxidation were inferior to these of iron oxidation in the same atmosphere. Comparing to the linear constants of iron, the apparent activation energy of iron was also higher than that of 441 and Crofer oxidised in pure CO₂.

6. As observed in the PEC experiments, the oxide presented the energy gap values corresponding to rhombohedral (Fe,Cr)₂O₃ and Cr₂O₃. These possible oxides also showed the n-type of semiconductor, agreeing with the semiconductor type of chromia equilibrated with a low oxygen potential.

7. As observed in isobaric kinetics and markers experiments, the kinetic model was proposed with n-type chromia with Cr_i^{•••} interstitial chromium ions as the major defect.

8. The scale characterization by SEM-EDX and XRD showed the surface morphology of steels with the major rhombohedral of (Fe,Cr)₂O₃ and Cr₂O₃ topped with a layer of Mn-Cr spinel and dispersed TiO₂ nodules.

6.1.2 Conclusions for steels under synthetic biogas

AISI441 and Crofer22APU were exposed to synthetic biogas (50-70%CH₄ and 30-50%CO₂) at high temperatures in order to study this corrosion behaviour. The following conclusions could be drawn:

1. The thermodynamic calculations by FactSage showed that the partial pressure of oxygen produced by the mixtures of carbon dioxide and methane used in this work lies in the range 10^{-23} to 10^{-20} bar for temperatures between 700 and 900°C. These pressures led to the existence of stable binary oxide from stainless steel oxidation as Cr_2O_3 , SiO_2 , TiO_2 , Nb_2O_5 , but not iron oxides. The spinel phase $(\text{Mn,Cr})_3\text{O}_4$ was also stable in such conditions.

2. In the composition range of the synthetic biogas (50-70 % CH_4 and 30-50% CO_2), the carbon activity was always equal to 1, revealing that the formation of solid carbon from the atmosphere is possible. This will therefore lead to possible carbide formation, as Cr and/or Ti or Nb carbide.

3. Oxidation kinetics of the steels in synthetic biogas were linear functions, with the rate constants higher than these for steel oxidation in pure CO_2 . It was also noted that increasing the fraction of CH_4 in biogas increased the corrosion rate.

4. According to kinetic experiments, the linear constants for 441 and Crofer subjected to the same methane fraction in biogas atmosphere were also almost identical. It was observed that all constants were in the same range.

5. The linear constants of 441 in the range of biogas (50-70% CH_4) tend to be greater than these in pure CO_2 . The estimation of the apparent activation energy of 441 calculated by Arrhenius law to be 120, 206, 158, and 273 $\text{kJ}\cdot\text{mol}^{-1}$ for 30, 50, 70 and 100% of methane in synthetic biogas consequently. The linear constants of Crofer also showed the same tendency.

6. The corrosion kinetics of steels in biogas were also performed using the continuous thermogravimetric method. All kinetics were also linear but it was found that the constants determined by discontinuous method were superior to these by continuous method in the same atmospheres. However, the methane fraction in biogas did not play an importance role with regard to the kinetic constants by this method.

7. The linear velocity of the gas was more influent on the kinetic constants of corrosion by CH_4 than by CO_2 .

8. The oxides Cr_2O_3 and Mn-Cr spinel formed on 441 in biogas as in CO_2 , but Cr carbide could also appear in the scale and/or in the metal.

9. At $T \leq 800^\circ\text{C}$, the scale was compact and acted as a barrier to carbon penetration but at 900°C porosity in scales led to direct reaction between biogas and metal.

10. Carbon strongly deposited on samples exposed to synthetic biogas at 900°C but not at lower temperatures. The temperature of 800°C must not be over-passed to ensure carbon free operation of SOFCs.

6.2 Perspectives

1. As reviewed in the industrial context, the fermentative biogas is more complex than that in this experiment. Effect of water vapour and/or sulphur-containing gas in $\text{CH}_4 + \text{CO}_2$ simulated biogas on the kinetics of stainless steel AISI441 should be focussed. Flexibility of biogas composition and/or impurity tolerance on performance of stainless steel interconnect should be also discussed.

2. As reviewed in the industrial context, the effect of other gases such as H_2S should be also investigated in order to reduce carbon in the system.

3. As observed in the experiments of biogas, at higher temperature (900°C), carbon attack taking place on the oxidation led to the high porous oxide scale and carburization of materials. The development procedures for diminishing carbon before gas inlet should be also conducted.

3. According to the composition of biogas, the composition of real fermentative biogas is depended on the production resource which is different with location and biomass waste types. The reactivity of steels used as SOFCs interconnectors should be further more studied under real biogas atmospheres.

4. As reviewed in chapter 1 of Introduction, composition of gases in both cathode and anode side varies from gas inlet to gas outlet. The effect of composition of gases in both anode and cathode side may be further investigated at the same time.

5. According to the performance of SOFCs interconnectors, the other properties such mechanical adhesion, electrical conductivity and Cr evaporation, of 441 subjected to biogas atmosphere should be investigated.

6. Other coating materials, such as LSM or LSC or reactive-element coating, and also coating procedure may be further conducted.

7. The reactivity of other conventional steels under general SOFCs or biogas atmospheres should be also investigated. The modification of surface of steels will be then conducted.



ศูนย์วิจัยทรัพยากร
จุฬาลงกรณ์มหาวิทยาลัย

References

- Abellan J.P., Olszewski T., Penkalla H.J., Meier G.H., Singheiser L., Quadackers W.J. Scale Formation Mechanisms of Martensitic Steels in High CO₂/H₂O-Containing Gases Simulating Oxyfuel Environments. **Materials at High Temperature** 26, 1, (2009): 63-72.
- Abellan J.P., Olszewski T., Meier G.H., Singheiser L., Quadackers W.J. The oxidation behaviour of the 9% Cr steel P92 in CO₂- and H₂O-rich gases relevant to oxyfuel environments. **International Journal of Material Research** 101, 2, (2010): 287-299.
- Allam I.M. and Gasem Z.M. High temperature corrosion of alloy Haynes 556 in carburizing/oxidizing environments, **Materials and Corrosion** 58, No.4, (2007): 245-253.
- Antoni L. Materials for solid oxide fuel cells: the challenge of their stability. **Material Science Forum** 461-464, (2004): 1073-1090.
- Assabumrungrat S., Laosiripojana N., Piroonlerkgul P. Determination of the boundary of carbon formation for dry reforming of methane in a solid oxide fuel cell. **J. Power sources** 159, (2006): 1274-1282.
- Azad A.M., Sreedharam O.M. and Gnanamoorthy J.B. Activities of metal in an AISI316LN stainless steel by emf measurements. **J. Nuclear Materials** 167, (1989): 82-88.
- Barin I., **Thermochemical data of pure substances**. VCH, Weinheim, Germany, 1989.
- Belton G.R., Fruehan R.J. The determination of activities by mass spectrometry. I. The liquid metallic systems Iron-Nickel and Iron-Cobalt. **J. Phys.Chem** 71, (1967): 1403-1409.
- Billings G.J., Smeltzer W.W., and Kirkaldy J.S. Oxidation and decarburization kinetics of iron-carbon alloys. **J. Electrochem. Soc.: Solid State Science** 117, 1, (1970):111-117.

- Brylewski T., Nanko M., Maruyama T., Przybylski K. Application of Fe-16Cr ferritic alloy to interconnector for a solid oxide fuel cell. **Solid State Ionics** 143, (2001): 131-150.
- Birks N., Meier G.H. **Introduction to high temperature oxidation of metals**. Edward Arnold (Publishers) Ltd, 1983.
- Butler M.A. Photoelectrolysis and physical properties of the semiconducting electrode WO_3 . **J. Applied physics** 48, (1977): 1914.
- Calphad, Available from <http://www.calphad.com>
- Chandra-ambhorn S. **Reactivity and surface modification of stainless steels used as electric interconnectors in high temperature solid oxide fuel cells**. Thèse de doctorat, Matériaux et Génie des Procédés, INP Grenoble, France, 2006.
- Chase M.W., Davies Jr., C.A., Rowney J.R., Jr., Frurip D.J., McDonald R.A., and Syverud A.N.. **JANAF Thermochemical tables**, 3rd ed, Vol.14, 1985.
- Dehoff R. **Thermodynamics in materials science**, 2nd ed, CRC Press Taylor & Francis Group, 2006.
- Fujii C.T. and Meussner R.A. Carburization of Fe-Cr alloys during oxidation in dry carbon dioxide. **J. Electrochem.Soc.: Electrochemical Science** 114(5), (1967): 435-442.
- FACTSAGE 5.5, may 2007, Thermfact and GTT-technologies, CNRS-LTPCM Grenoble.
- Finnerty C.M. , Ormerod R.M. Internal reforming over nickel/zirconia anode in SOFCS operating on methane: influence of anode formulation, pre-treatment and operating conditions. **J. Power sources** 86, (2000): 390-394.
- Fergus J. W. Metallic interconnects for solid oxide fuel cells. **Materials Science and Engineering** A397, (2005): 271-283.
- Fuller E.N., Schettler P.D., Gidding J.C. A new method for prediction of binary gas - phase diffusion coefficients. **Industrial and Engineering chemistry** 58, 19, (1966)
- Gartner W.W. Depletion layer photoeffects in semiconductors. **Physical Review** 116, (1959): 84.

- Geng S., Zhu J. Promising alloys for intermediate-temperature solid oxide fuel cell interconnect application. **J. of Power Sources** 160, (2006): 1009-1016.
- Girona K., Laurencin J., Morel B., Petitjean M., Bultel Y., and Lefebvre-Joud F. Solid oxide fuel cell operated under biogas simulation and experimentation. **Proceeding of 7th European SOFC Forum**, Lucerne, Switzerland, July 3-7, (2006).
- Goutier F., Valette S., Vardelle A., and Lefort P. Oxidation of stainless steel 304L in carbon dioxide. **Corrosion science** (2010), accepted manuscript. DOI: 10.1016/j.corsci.2010.03.022
- Herle J.V., Membrez Y. Biogas exploitation in SOFC, in: U.Bossel(Ed.), **Proceedings of the 5th European Forum Secretariat**, CH5442-Oberrohrdorf, Switzerland, 2003: 1003-1010.
- Herle J.V., Membrez Y., Bucheli O. Biogas as a Fuel source for SOFC co – generators, **J. Power Source** 124, 2004: 300-312.
- Herle J.V., Maréchal F., Leuenberger S., Membrez Y., Bucheli O., Favrat. D. Process flow model of solid oxide fuel cell system supplied with sewage biogas, **Journal of Power Source** 131, (2004): 127-141.
- Holt A., Kofstad P. Electrical conductivity and defect structure of Cr_2O_3 . I. High temperatures ($> \sim 1000^\circ\text{C}$), **Solid State Ionics** 69, (1994): 127-136.
- Holt A., Kofstad P. Electrical conductivity and defect structure of Cr_2O_3 . II. Reduced temperatures ($< \sim 1000^\circ\text{C}$), **Solid state ionics** 69, (1994): 137-143.
- HSC chemistry, Outotec company, Germany, available at CNRS-LTPCM Grenoble.
- Jian L., Huezo J., Ivey D G. Carburisation of interconnect materials in solid oxide fuel cells. **J. of Power Sources** 123, (2003):151-162.
- Jung I.-H. Critical evaluation and thermodynamic modelling of the Mn-Cr-O system for the oxidation of SOFC interconnect. **Solid State Ionics** 177, (2006): 765-777.
- Kofstad P. and Lillerud K.P. On high temperature oxidation of Chromium: II Properties of Cr_2O_3 and the oxidation mechanism of chromium, **J.Electrochem.Soc.: Solid-State Science and Technology** 127, 11, (1980): 2410-2419.

- Kofstad P. **High temperature corrosion**, Elsevier Science publishing, 1988.
- Kofstad P., Bredesen R. High temperature corrosion in SOFC environments. **Solid State Ionics** 52, (1992): 69-75.
- Kurokawa H., Kawamura K., Maruyama T. Oxidation behaviour of Fe-16Cr alloy interconnect for SOFC under hydrogen potential gradient. **Solid State Ionic** 168, (2004): 13-21.
- Lee D.B. and Choi J.W. High temperature oxidation of steels in air and CO₂-O₂ atmosphere, **Oxidation of Metals** 64, Nos.516, (2005):319-329.
- Lupis C.H.P. **Chemical thermodynamics of materials**, International edition, Prentice hall Simon &Schuster(Asia) Pte Ltd, 1993.
- S. Mrowec, **Defect and diffusion in solids: an introduction**. Elsevier Scientific Publishing Company, 1980.
- Moosa A., Ahmed J.K. and Hoobi A. Oxidation properties in CO₂ of Inconel alloy 600 coated by simultaneous aluminizing-chromizing process. **Chinese J. Aeronautics** 20, (2007): 134-139.
- Norheim A., Hustad J. E., Bryknes J., Vik A. Comparison of performance data of a solid oxide fuel cell using biomass gasification gas and natural gas. **Science in thermal and chemical biomass conversion**, Vancouver Island, BC, Canada, Aus./Sept. 2004.
- Oquab D., Xu N., Monceau D., Young D.J. Subsurface microstructural changes in a cast heat resisting alloy caused by high temperature corrosion, **Corrosion science** 52, (2010): 255-262.
- Piccardo P., Chevalier. S., Molins R., Viviani M., Caboche G., Barbucci A., Sennour M., Amendola R. Metallic interconnects for SOFC: Characterization of their corrosion resistance in hydrogen/water atmosphere and at the operating temperatures of differently coated metallic alloys. **Surface & Coating technology** 201, (2006): 4471-4475.
- Piroonlerkgul P., Assabumrungrat S., Laosiripojana N., Adesina A.A., Selection of appropriate fuel processor for biogas-fuelled SOFC system, **Chemical Engineering journal** 140, (2008): 341-351.

- Rasi S., Veijanen A., and Rintala J. Trace compounds of biogas from different biogas production plants, **Energy** 32, (2007): 1375-1380.
- Reeves A.S. and Smeltzer W.W. Decarburization of an iron 0.8 w/o carbon alloy in the presence of a Wustite scale. **J.Electrochem.Soc.: Solid state science**, (Jan 1970): 117-121.
- Rouillard F., Cabet C., Wolski K., Pijolat M. Oxide-layer formation and stability on a nickel-base alloy in impure helium at high temperature formation. **Oxid.Met.**, 68, (2007): 133-148.
- Rouillard F., Cabet C., Wolski K., Pijolat M. Oxidation of a chromia-forming nickel-base alloy at high temperature in mixed diluted CO/H₂O atmospheres, **Corrosion Science** 51, (2009): 752-760
- Sarrazin P., Galerie A., Fouletier J. **Les mécanismes de la corrosion sèche : une approche cinétique**, EDP Science, 2000
- Schneider A., Viefhaus H., Inden G. Surface analytical studies of metal dusting of iron in CH₄-H₂-H₂S mixtures, **Material and Corrosion** 51, (2000): 338-343.
- Srisruar A., Coindeau S., A.Galerie, Petit J.-P., Wouters Y. Identification by photoelectrochemistry of oxide phases grown during the initial stages of thermal oxidation of AISI441 ferritic stainless steel in air or in water vapour, **Corrosion Science** 51, (2009): 562-68.
- Toscan F. **“Optimisation conjointe de l’adhérence des couches d’oxydes et des cinétiques d’oxydation thermique sur acier inoxydables”** Thèse de Doctorat, Matériaux et Génie des Procédés, INP Grenoble, France, 2004.
- Venugopal V., Kulkani S.G., Subbanna C.S., and Sood D.D. Determination of chemical activities of Fe, Cr, Ni, and Mn in stainless steel 316 by Knudsen effusion cell mass spectrometry. **J.Alloy and Compounds** 218, (1995): 95-100.
- Valette S., Denoirjean A., Tétard D., Lefort P. C40E steel oxidation under CO₂: Kinetics and reactional mechanism. **Journal of alloys and compounds** 413, (2006): 222-231.
- Verhoeven D. J., **Fundamental of physical metallurgy**, John Wiley&Sons, 1975.

- Wouters Y. **Oxydation thermique des métaux dans la vapeur d'eau, cas du nickel et du titane.** Thèse de Doctorat, Matériaux et Génie des Procédés, INP Grenoble, France, 1996.
- Wyckoff R.W.G. **Crystal structures volume I & II**, 2nd ed., John Wiley & Sons, New York, 1964.
- Xu N., Monceau D., Young D.J., Furtado J. High temperature corrosion of cast heat resisting steels in CO + CO₂ gas mixtures. **Corrosion Science** 50, (2008): 2398-2406.
- Yin R.C. Carburization performance of incoloy 800HT in CH₄/H₂ gas mixture, **Material Science and Engineering A** 380, (2004): 281-289.
- Yin R. Carburization of 310 stainless steel exposed at 800 – 1100°C in 2%CH₄/H₂ gas mixture. **Corrosion science** 47, (2005): 1896-1910.
- Young E.W.A, Stiphout P.C.M. and De Wit J.H.W. N type behavior of chromium (III) oxide. **J Electrochem.Soc: Solid State Science and Technology** 132(4), (1985): 884-886.
- Zhang J., Boddington K., Young D.J. Carburisation and metal dusting of 304 stainless steel in CO/CO₂ and CO/H₂/H₂O gas mixtures. **Corrosion Science** 50, (2008): 3107-3115.

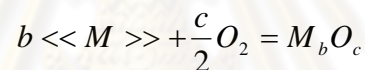
Appendices

Appendix A

Thermodynamic calculations

A.1 Calculation of modified Ellingham diagram in terms of partial pressure of di-oxygen participating in oxidation and temperature

The oxidation reaction of a metal M is written as follows:



The Gibbs free energy of formation of one mol of $M_a O_b$ is then $\Delta_f G_{M_a O_b}$, defined by the thermodynamic relation,

$$\Delta_f G_{M_b O_c} = \Delta_f G_{M_b O_c}^\circ + RT \ln \Pi$$

At equilibrium, $\Delta_f G_{M_b O_c} = 0$

Therefore,

$$\Delta_f G_{M_b O_c}^\circ = -RT \ln K$$

with

$$K = \frac{a_{M_b O_c}}{a_{\ll M \gg}^b a_{O_2}^{c/2}}$$

By assuming the unit activity of metal oxide and ideal behaviour of the di-oxygen molecule,

Hence,

$$\Delta_f G^\circ_{M_a O_b} = RT \ln \left(a_{\langle\langle M \rangle\rangle}^b P_{O_2}^{c/2} \right)$$

$$P_{O_2} = \exp \left[\frac{2}{c} \left(\frac{\Delta_f G^\circ_{M_b O_c}}{RT} - b \ln a_{\langle\langle M \rangle\rangle} \right) \right]$$

$$\log P_{O_2} = 0.4343 \left[\frac{2}{c} \left(\frac{\Delta_f G^\circ_{M_b O_c}}{RT} - b \ln a_{\langle\langle M \rangle\rangle} \right) \right] \quad (A-1)$$

with $\langle\langle M \rangle\rangle$ is the activity of constituent M in alloy (activity $\neq 1$) which can be calculated using various thermodynamic software. In this work, we chose to use Thermocalc. Reliability of calculation of activities by this software is confirmed by different methods and references as show in TableA-1.

TableA-1: Comparison of activities in stainless steel 316 calculated by different methods and references.

T (K)	Activity	KCMS*, [Venugopal, 1995]	Calculated by Azad et al. [Azad, 1989]	MEMF**, [Azad, 1989]	This calculation (Thermocalc)
1293	a_{Fe}	0.68 - 1.58	0.75	0.95	0.69
1293	a_{Cr}	0.23 - 0.93	0.27	0.28	0.46
1468	a_{Ni}	0.08 - 0.19	0.52	-	0.08
1302	a_{Mn}	$3.3 \times 10^{-7} - 9.5 \times 10^{-7}$	0.05	0.0039	0.02

* KCMS = K-cell mass spectrometry

** MEMS = Meta-stable EMF

According to table A1, the activities of Fe, Cr, Ni, and Mn calculated for stainless steel 316 in this study by Thermocalc were in excellent agreement with the

other experiments or calculations, showing the possible use of the models of this software.

The activities of metal alloy are depended on the composition and temperature. In this study, the activities of AISI441 were determined using the thermodynamic software Thermocalc as shown in Figure A.1.

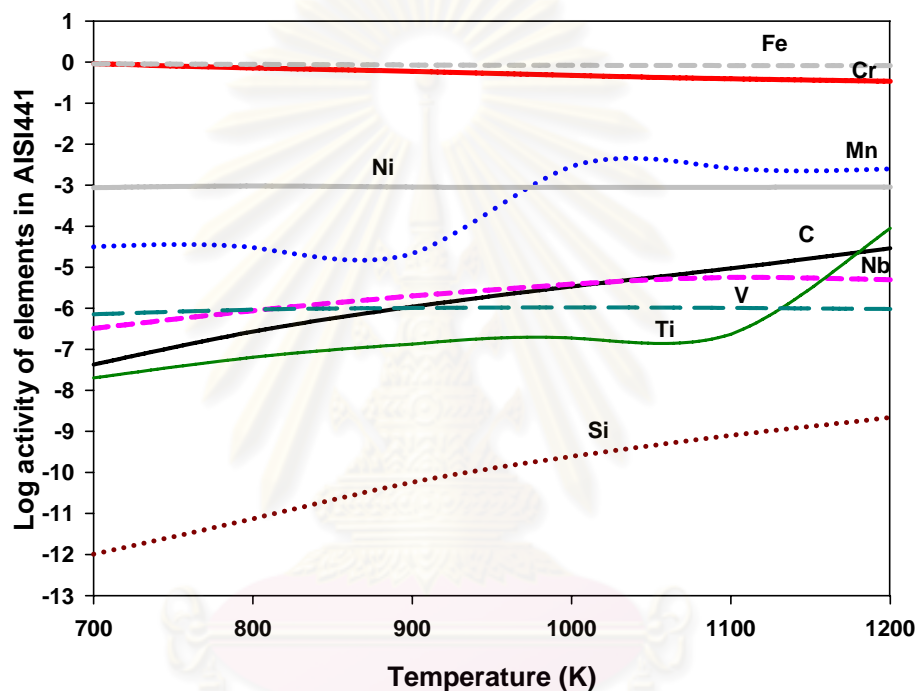


Figure A.1: the activities of the constituent of metal in the AISI441 in function of several temperatures.

The calculations show mostly activities of element in stainless steel 441 will increase when the temperature also increase because the potential energy between atom decrease when temperature increase. It was observed that the activity of elements such as Fe and Cr in solid solution attains to ideal behaviour according to Raoult's Law and others obey Henry's law.

For the metal oxides, the Gibbs free energy of formation of the useful compound in this study was compared between several references as show in Table A-2.

TableA-2: Gibb free energy of formation of several metal oxides in J/mol at 900 K

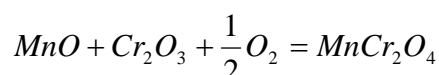
	$\Delta_f G_r^\circ$, (Barin 1989)		$\Delta_f G_r^\circ$, (Chase 1985)		$\Delta_f G_r^\circ$, FactSage databank	
	900 K	1200 K	900 K	1200 K	900 K	1200 K
Cr/Cr₂O₃	-901522	-826048	-894736	-818475	-890515.6	-816726.2
Mn/MnO	-319086	-296975	-	-	-318982.9	-296924.1
Ti/TiO₂	-780233	-727229	-774046	-727113	-780501.5	-727668.6
Fe/FeO	-205790	-186454	-213118	-194316	-206161.5	-186939.2
Si/SiO₂	-	-	-747468	-695653	-747785.5	-695640.2
Fe/Cr/FeCr₂O₄	-1154397	-1055516	-	-	-1155118.4	-1056770.1

According to Table A-2, the FactSage databank (Fact53) is no discrepancies comparing to the free energy form the other data, showing the confident use of these data.

A1.1 Gibbs free energy of formation of MnCr₂O₄

The Gibbs free energy of formation of MnCr₂O₄ is not available from thermodynamic data books (Barin 1989; Chase 1985) nor FactSage databank. Jung (Jung, 2006) supposed that the optimised Gibbs energy of formation of MnCr₂O₄ from MnO and Cr₂O₃ is -51 kJ.mol^{-1} in the temperature range of 500 to 1365°C.

Thus



$$\Delta_r G^\circ = -51 \text{ kJ.mol}^{-1}$$

From thermodynamic relation, the equation is written as following

$$\Delta_f G_{MnO/ Cr_2O_3 / MnCr_2O_4}^\circ = \Delta_f G_{Mn/ Cr / MnCr_2O_4}^\circ - \Delta_f G_{MnO}^\circ - \Delta_f G_{Cr_2O_3}^\circ$$

$$\therefore \Delta_f G_{Mn/ Cr / MnCr_2O_4}^\circ = -51000 + \Delta_f G_{MnO}^\circ + \Delta_f G_{Cr_2O_3}^\circ$$

Substituting $\Delta_f G_{M_b O_c}^\circ$, and the activities to equation (A-1). These P_{O_2} will be plotted as $\log P_{O_2}$ in function of inverse temperature in range of 700 to 900°C, near similarly as the Ellingham diagram, but the critical pressure of O_2 for classic Ellingham diagram is derived by equation (A-1) supposing the activities of constituents equal to 1. Therefore, the Ellingham diagrams and the modified Ellingham are shown in Figure A.2 and A.3 respectively.

ศูนย์วิทยทรัพยากร
จุฬาลงกรณ์มหาวิทยาลัย

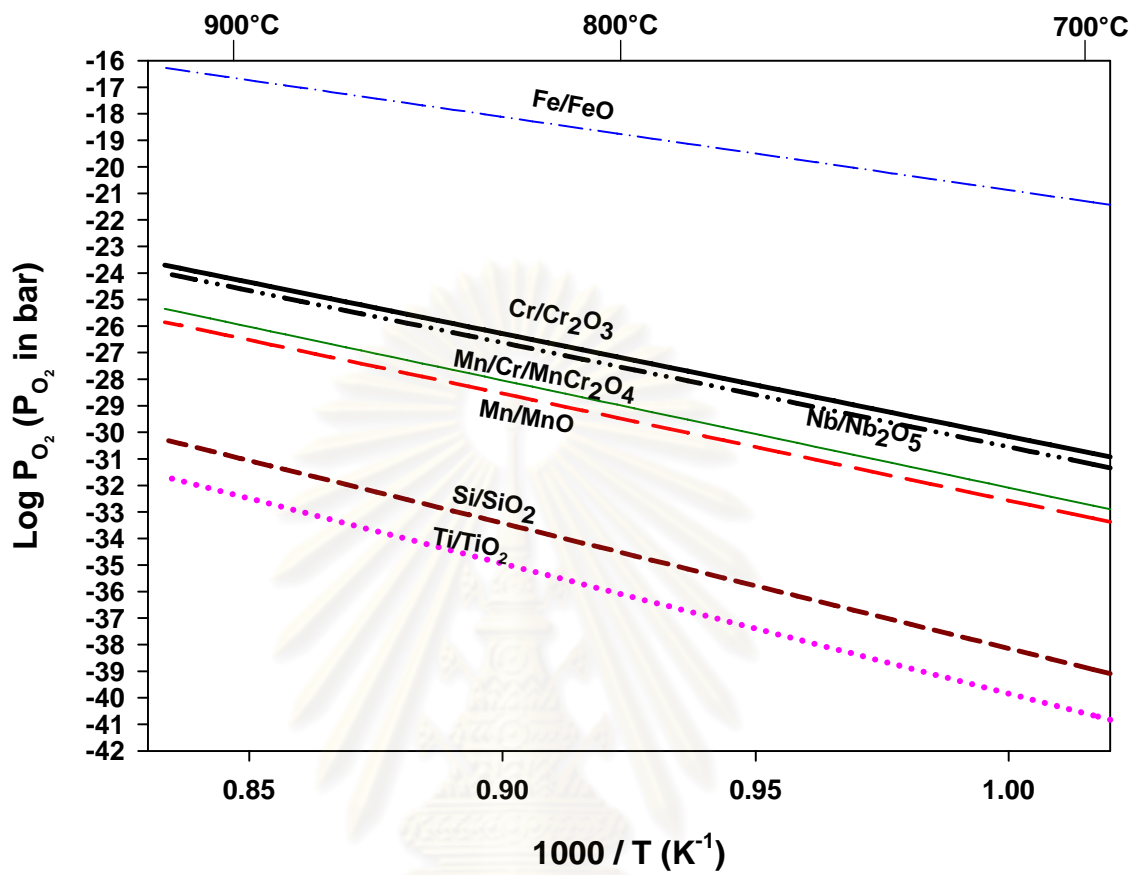
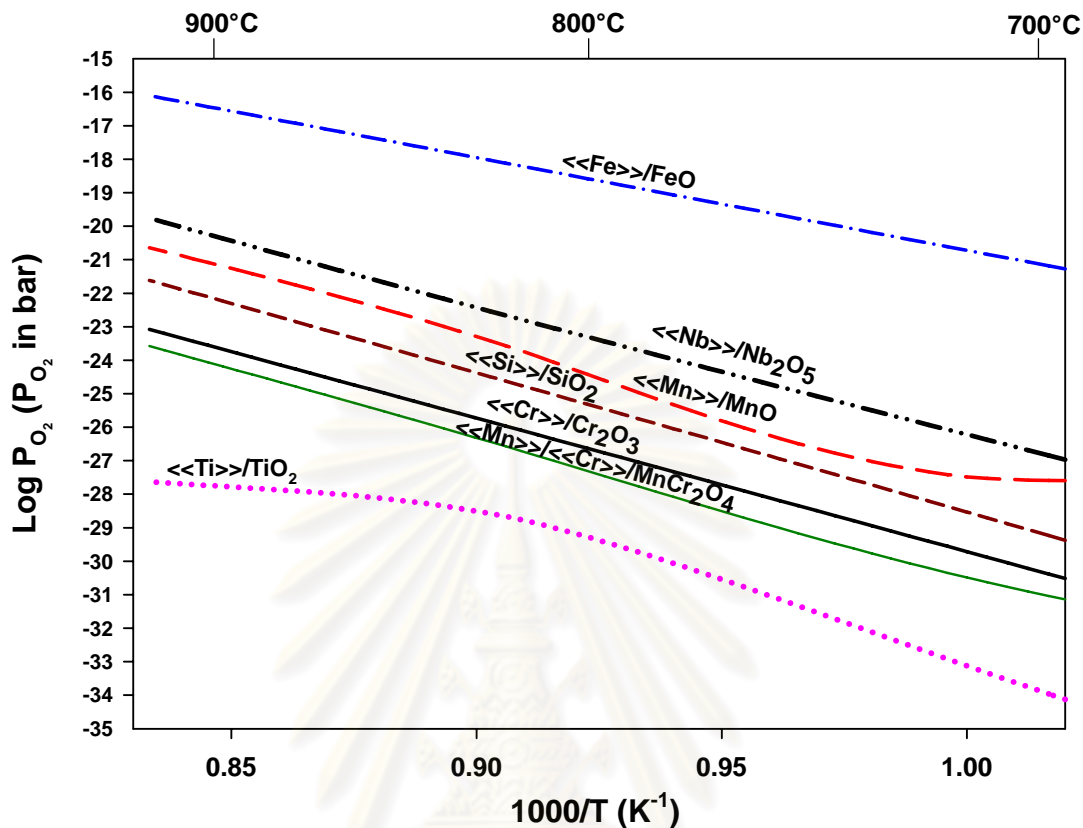


Figure A.2: Classic Ellingham diagram plotted as $\text{Log } P_{\text{O}_2}$ in function of inverse temperature.

ศูนย์วิทยทรัพยากร
จุฬาลงกรณ์มหาวิทยาลัย



FigureA.3: Modified Ellingham diagram plotted as $\text{Log } P_{O_2}$ in function of inverse temperature

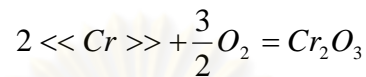
From Figure A.2 and A.3, the diagrams show that all critical pressure of oxygen for pure metal increases with increasing temperature. Comparing with both Ellingham diagrams, although the same metal oxides will be feasibly formed in 441 but the critical pressures of oxygen in classical diagram are lower than that in modified diagram due to their activity. In addition, the order of stability of metal oxide is changed in modified diagram.

A.2 Thermodynamic stability of MnCr_2O_4 at 1073 K

For construction of phase stability diagram of metal oxide such as Cr_2O_3 , MnO and MnCr_2O_4 in alloy such as 441 or Crofer22 with the pressure of oxygen in

function of activity of Mn, all possible phases are calculated thermodynamically by the equations following

For line (a), Critical pressure of oxygen forming Chromia (Cr_2O_3) are calculated by this chemical reaction following



Gibbs free energy of formation Cr_2O_3 at 1073 K, $\Delta_r G_{\text{Cr}_2\text{O}_3}^\circ = -847860.30 \text{ J}$

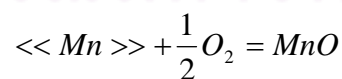
$$\Delta_r G_{\text{Cr}_2\text{O}_3}^\circ = -RT \ln \left(\frac{1}{a_{\text{Cr}}^2 P_{\text{O}_2}^{3/2}} \right)$$

$$\frac{\Delta_r G_{\text{Cr}_2\text{O}_3}^\circ}{RT} = 2 \ln a_{\text{Cr}} + \frac{3}{2} \ln P_{\text{O}_2}$$

$$\log P_{\text{O}_2} = 0.43 \left\{ \frac{2}{3} \left[\frac{\Delta_r G_{\text{Cr}_2\text{O}_3}^\circ}{RT} - 2 \ln a_{\text{Cr}} \right] \right\}$$

Therefore, every a_{Mn} , $\log P_{\text{O}_2} = \text{const.} = -27.01$

For line (b), MnO formed thermodynamically is carried out by this chemical reaction.



Gibb free energy of formation MnO at 1073 K, $\Delta_r G_{\text{MnO}}^\circ = -306346.80 \text{ J}$

$$\Delta_r G_{\text{MnO}}^\circ = -RT \ln \left(\frac{1}{a_{\text{Mn}} P_{\text{O}_2}^{1/2}} \right)$$

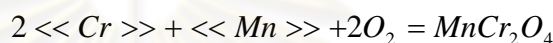
$$\log a_{Mn} + \frac{1}{2} \log P_{O_2} = 0.43 \left(\frac{\Delta_r G_{MnO}^\circ}{RT} \right)$$

$$\log P_{O_2} = 0.43 \left(\frac{2\Delta_r G_{MnO}^\circ}{RT} \right) - 2 \log a_{Mn}$$

Therefore,

$$\log P_{O_2} = -29.83 - 2 \log a_{Mn}$$

For line (c), $MnCr_2O_4$ formed at equilibrium is also carried out by this chemical reaction



Gibb free energy of formation $MnCr_2O_4$ at 1073 K, $\Delta_r G_{MnCr_2O_4}^\circ = -1205207.10$ J

$$\Delta_r G_{MnCr_2O_4}^\circ = -RT \ln \left(\frac{1}{a_{Mn} a_{Cr}^2 P_{O_2}^2} \right)$$

$$\log a_{Mn} + 2 \log a_{Cr} + 2 \log P_{O_2} = 0.43 \left(\frac{\Delta_r G_{MnCr_2O_4}^\circ}{RT} \right)$$

$$\log P_{O_2} = 0.43 \left(\frac{\Delta_r G_{MnCr_2O_4}^\circ}{2RT} \right) - \log a_{Cr} - 0.5 \log a_{Mn}$$

Therefore,

$$\log P_{O_2} = -29.34 - 0.5 \log a_{Mn}$$

The phase boundaries between Cr_2O_3 , MnO and $MnCr_2O_4$ are drawn by line (e) and (f) which are calculated by interception of line (a), (b) and (c). Considering the lines which compose of the most stable phase, i.e. the lowest line, the phase stability of $MnCr_2O_4$ with the activity of Mn is shown in Figure A.4.

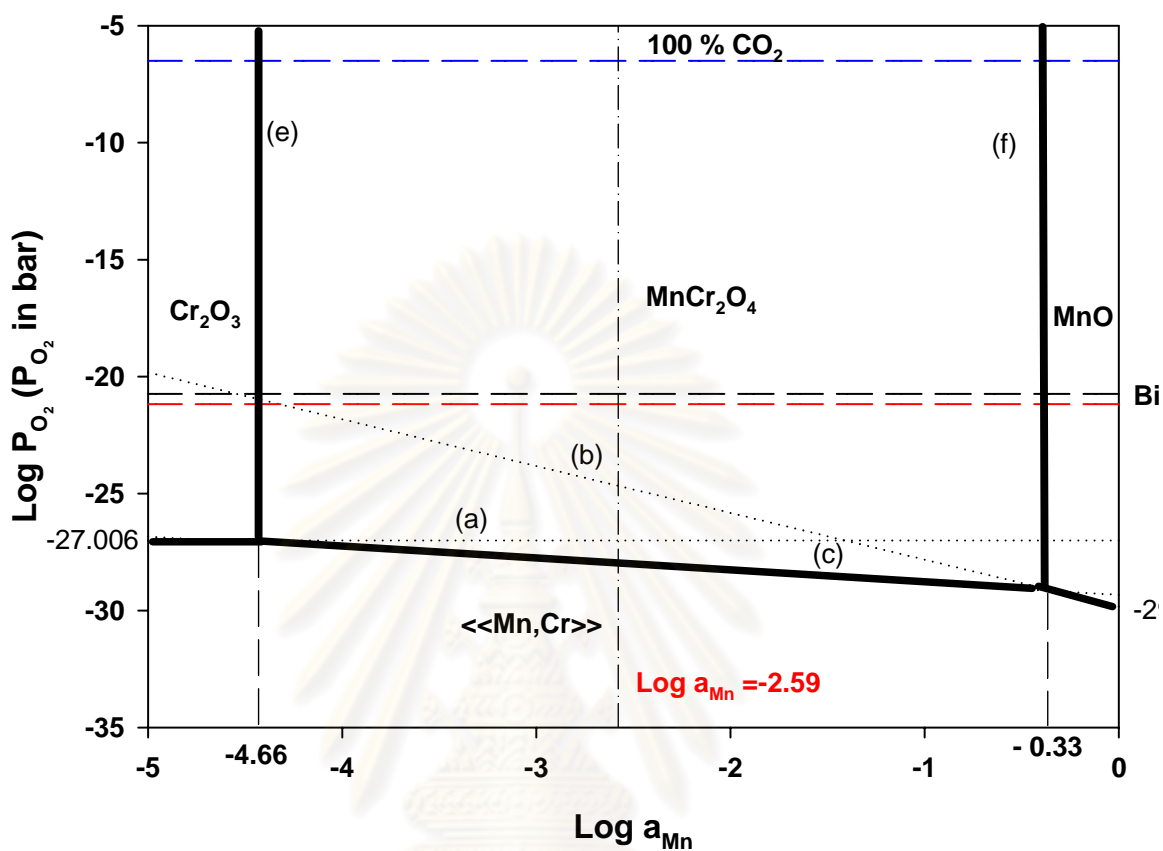


Figure A.4: Thermodynamic stability of MnCr_2O_4 versus the activity of Mn at 1073K

From Figure A.4, when the activity of Mn in 441 is equal to $10^{-2.59}$, it can be concluded that the spinel MnCr_2O_4 can thermodynamically form on the oxidizing sample of 441 in contact with synthetic biogas with large driving force at $\text{PO}_2 = 10^{-22}$ and small driving force at $\text{PO}_2 = 10^{-27}$ bar.

Appendix B

Oxide thickness calculation

B.1 The estimation of oxide thickness from mass gain

Assuming only Cr oxide appearing in the scale, the reaction of oxidation will be considered as follows



The mass variation of oxide in unit surface area is given as

$$\frac{\Delta m(Cr_2O_3)}{A} = t(Cr_2O_3) \cdot \rho(Cr_2O_3) \quad (2)$$

Where $\frac{\Delta m(Cr_2O_3)}{A}$ is mass gain in $g \cdot cm^{-2}$

$t(Cr_2O_3)$ is thickness of Cr oxide in cm

$\rho(Cr_2O_3)$ is density of Cr oxide: 5.21 g cm^{-3}

The measurement of mass gain by thermogravimetric analysis corresponds to the mass of oxygen $\frac{\Delta m}{A}$ ($g \cdot cm^{-2}$). A corrective factor between the mass of oxide and oxygen will be calculated as follows

$$\frac{\Delta m(Cr_2O_3)}{A} = \frac{\Delta n(Cr_2O_3) \cdot M(Cr_2O_3)}{A} = \frac{\frac{2}{3} \Delta n(O_2) \cdot M(Cr_2O_3)}{A} = \frac{2}{3} \frac{M(Cr_2O_3)}{M(O_2)} \cdot \frac{\Delta m}{A} \quad (3)$$

where $\Delta n(Cr_2O_3)$ is the variation of molar number of Cr oxide

$M(Cr_2O_3)$ is molar mass of Cr oxide: ($152 \text{ g} \cdot \text{mol}^{-1}$)

$\Delta n(O_2)$ is the variation of molar number of oxygen

$M(O_2)$ is the molar mass of oxygen: ($32 \text{ g} \cdot \text{mol}^{-1}$)

Taking (3) into (2), the equation (2) become

$$t(\text{Cr}_2\text{O}_3) = \frac{2}{3} \frac{M(\text{Cr}_2\text{O}_3)}{M(\text{O}_2)} \cdot \frac{1}{\rho(\text{Cr}_2\text{O}_3)} \cdot \frac{\Delta m}{A} = 0.608 \cdot \frac{\Delta m}{A} \quad (4)$$

Hence, a mass gain of $1 \text{ mg}\cdot\text{cm}^{-2}$ corresponds to a chromia thickness of $\sim 6 \mu\text{m}$. In case of MnCr_2O_4 as oxide scale by $2\text{Cr} + \text{Mn} + 2\text{O}_2 = \text{MnCr}_2\text{O}_4$, the same calculation was used with the equation as follows:

$$\begin{aligned} \frac{\Delta m(\text{Cr}_2\text{O}_3)}{A} &= \frac{\Delta n(\text{MnCr}_2\text{O}_4) \cdot M(\text{MnCr}_2\text{O}_4)}{A} \\ &= \frac{\frac{1}{2} \Delta n(\text{O}_2) \cdot M(\text{MnCr}_2\text{O}_4)}{A} \\ &= \frac{1}{2} \frac{M(\text{MnCr}_2\text{O}_4)}{M(\text{O}_2)} \cdot \frac{\Delta m}{A} \end{aligned} \quad (5)$$

$$t(\text{Cr}_2\text{O}_3) = \frac{1}{2} \frac{M(\text{MnCr}_2\text{O}_4)}{M(\text{O}_2)} \cdot \frac{1}{\rho(\text{MnCr}_2\text{O}_4)} \cdot \frac{\Delta m}{A} = 0.667 \cdot \frac{\Delta m}{A} \quad (6)$$

Where $\Delta n(\text{MnCr}_2\text{O}_4)$ is the variation of molar number of Cr oxide

$M(\text{MnCr}_2\text{O}_4)$ is molar mass of Cr oxide: ($207 \text{ g}\cdot\text{mol}^{-1}$)

$\Delta n(\text{O}_2)$ is the variation of molar number of oxygen

$M(\text{O}_2)$ is the molar mass of oxygen: ($32 \text{ g}\cdot\text{mol}^{-1}$)

$\rho(\text{Cr}_2\text{O}_3)$ is density of Mn-Cr spinel: 4.85 g cm^{-3}

Therefore, a mass gain of $1 \text{ mg}\cdot\text{cm}^{-2}$ corresponds to a MnCr_2O_4 thickness of $\sim 6 \mu\text{m}$.

Appendix C

Naphthalene formation

C.1 Introduction

While the ferritic stainless steels were subjected to synthetic biogas atmospheres at temperatures higher than 900°C, brown flake solid material was surprisingly observed at the gas outlet and the end of the reactor tube as shown in Figure C.1. Dark brown liquid was also perceived near the heating zone but this surprising substance did not exist on the surface of stainless steels. However, the hypothesis is proposed that this substance is possibly hydrocarbon synthesized from biogas reactions.

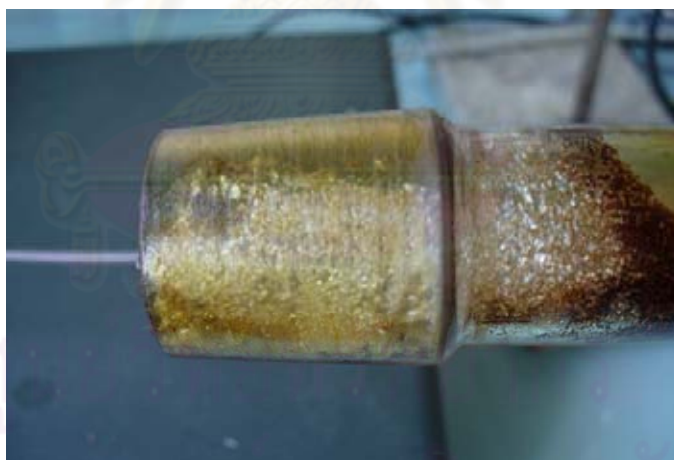


Figure C.1: brown solid particles appearing at the end of the reactor tube when ferritic stainless steels are exposed to synthetic biogas at 900°C during 5 hours

According to literature review [1,2], methane can lead to the formation of aromatic benzene and naphthalene by the catalytic dehydrocondensation process. The catalytic conversion of methane can be described as indirect processes relying upon the production of synthesis gas, either by reforming reaction or by partial oxidation,

followed by Fischer–Tropsch chemistry. However, this conversion process is dependent on several factors such as pressure, or the presence of a catalyst.

This aim of this observation is to recognize and avoid this substance which may appear in some processes using biogas.

C.2 Characterisation Procedure

All solid substance in the tube was collected. The X-ray diffraction spectroscopy (XRD) was then applied to investigate the types of crystallized compounds. Cu-K α was used as the radiation source. The diffraction angle was available in the range of 6.5-101 $^\circ$.

C.3 Results and Discussion

The XRD pattern of the substance is presented in Figure C.2. All peaks corresponding to monoclinic naphthalene (C₁₀H₈) were identified.

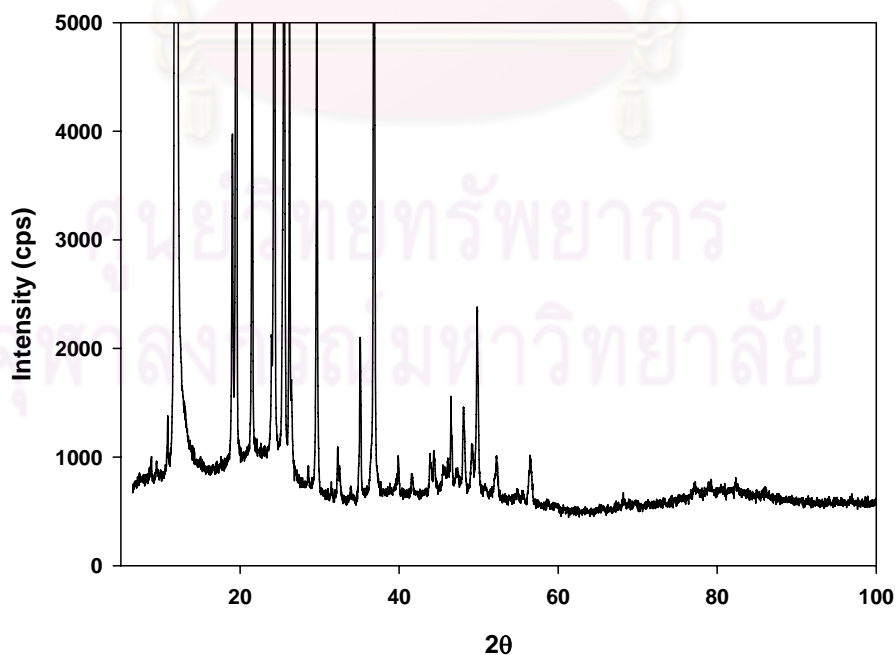
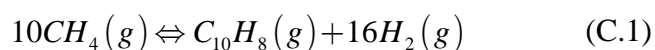


Figure C.2 XRD pattern of the substance appearing during the biogas reaction at 900 $^\circ$ C, indexed as the naphthalene.

According to thermodynamic calculations by Factsage, the naphthalene can be spontaneously ($\Delta G^\circ = -17086.4 \text{ J.mol}^{-1}$) transformed from the methane at high temperature (ca.900°C) with the following reaction:



From reaction C.1, naphthalene in the gas phase can form in the reaction tube at high contents of methane in the biogas. Observing the temperature along the 1 m long reaction tube, this gas species can be condensed in the lower temperature zone, due to low boiling (218°C) and melting point (80.26°C) of naphthalene. In the other hand, the naphthalene did not appear in the tube when the reaction occurred without stainless steels. It is probable that some elements such as Fe or Mo in stainless steels acted as a catalyst for this formation.

C.4 Conclusion

The formation of naphthalene can be occurred in the reaction consisting of methane and steels at 900°C due to dehydrocondensation process. Using biogas or methane as fuel in SOFC, the operating temperature should lower than 900°C in order to avoid the existence of naphthalene which lead to the material degradation of component in the device.

[1] Y. Shu, M. Ichikawa, *Catalystoday*, 2001, 71: 55

[2] Y. Shu, R. Ohnishi, M. Ichikawa, *J. catalysis*, 2002, 206:134

Biography

PIYOROSE PROMDIREK

Date of birth: 9 July 1980 at Sakon Nakhon

Current address: 13 Kosum 48 Yak 11 Donmeung, Bangkok, Thailand

Mobile: +66 8 00811244

Experience and Education

- 2002-2003 D.E.A. de Métallurgie et Matériaux à l'Institut National des Sciences et Technique Nucléaires, Saclay
Grade: 11.62/20
- 1998-2002 Bachelor of Engineering (B.Eng) at King Mongkut's Institute of Technology North Bangkok, Thailand
Subject: Mechanical engineering
Grade: 3.25/4.00
- 1995-1998 Certificat in technical education at King Mongkut's Institute of Technology North Bangkok, Thailand
Subject: Mechanical technology
Grade: 3.33/4.00

Conférences

1. P. Promdirek, G. Lothongkhum, Y. Wouters, A. Galerie *Cinetique de corrosion des aciers inoxydables ferritiques soumis au biogaz à haute temperature*, JECH40, Saint Etienne, 1-2 Avril 2009 (French lecture)
2. P. Promdirek, G. Lothongkum, J. Mougine, Y. Wouters, A. Galerie *High temperature corrosion of ferritic stainless steels exposed to synthetic biogas*, Gordon conference, New London, USA, 26-31 July 2009 (Poster)
3. P. Promdirek, G. Lothongkum, J. Mougine, Y. Wouters, A. Galerie *High temperature corrosion of ferritic stainless steels subjected to dry biogas*, EFC conference, Frankfurt, Germany, 31/09-2/10 2009 (Oral)
4. P. Promdirek, G. Lothongkum, Y. Wouters, S. Chandra-ambhorn, A. Galerie, *Effect of humidity on the kinetics of corrosion of ferritic stainless steels subjected to biogas*, ISHOC10, Zushi, Japan, 8-11 November 2010 (Oral)

Publications

1. P. Promdirek, G. Lothongkum, S. Chandra-ambhorn, Y. Wouters, A. Galerie, *Behaviour of ferritic stainless steels subjected to dry biogas atmospheres at high temperatures*, Material & Corrosion, (submitted)